UNITED STATES OF AMERICA
DEPARTMENT OF ENERGY
HYDROCARBONS AND GEOTHERMAL ENERGY OFFICE

In The Matter Of:	§	
	§	
Corpus Christi Liquefaction, LLC	§	**Docket No. 26-32-LNG**
Corpus Christi Liquefaction Stage IV, LLC	§	
	§	
Cheniere Marketing, LLC	§	
	§	

MOTION TO INTERVENE AND PROTEST OF INGLESIDE ON THE BAY COASTAL WATCH ASSOCIATION, INC., INDIGENOUS PEOPLES OF THE COASTAL BEND, KARANKAWA TRIBE OF TEXAS, AND CARRIZO/COMECRUDO TRIBE OF TEXAS, LLC

EXHIBIT 7

Impacts to Ingleside On The Bay Seagrass Meadows from Siltation and Erosion

Kirk Cammarata

Students: Austin Hamilton (MS), Carissa Pinon (MS), Collin Kerr (MS), Fabian Castro (UG), Jorge Jimenez (UG), Brooklyn McCormick (UG) and UAV & Satellite Imagery: Hua Zhang, PhD

TAMU-CC

Sponsor: Ingleside On The Bay Coastal Watch Association

TEXAS A&M UNIVERSITY CORPUS CHRISTI

IOBCWA

Photo Credit: Patrick Nye

Background

- The planned Moda (Enbridge) expansion received approval from USACE to construct additional ship berths to accommodate 2 Suezmax class tankers
- 8.86 acres of seagrass and 0.8 acres of wetlands will be directly lost from the construction footprint; Proposed mitigation will construct 20 acres of seagrass along Indian Point shoreline and construct a breakwater to facilitate its establishment and preservation (Mitigation ratio = 2.26:1).
- Additional acres of upland habitat are also proposed as part of the seagrass mitigation
- To my knowledge, only potential impacts from the construction activities have been considered for mitigation, not any *operational impacts*
- Multiple agencies have reviewed and commented on the permit

Overview of Ingleside On The Bay Community and Enbridge Facility

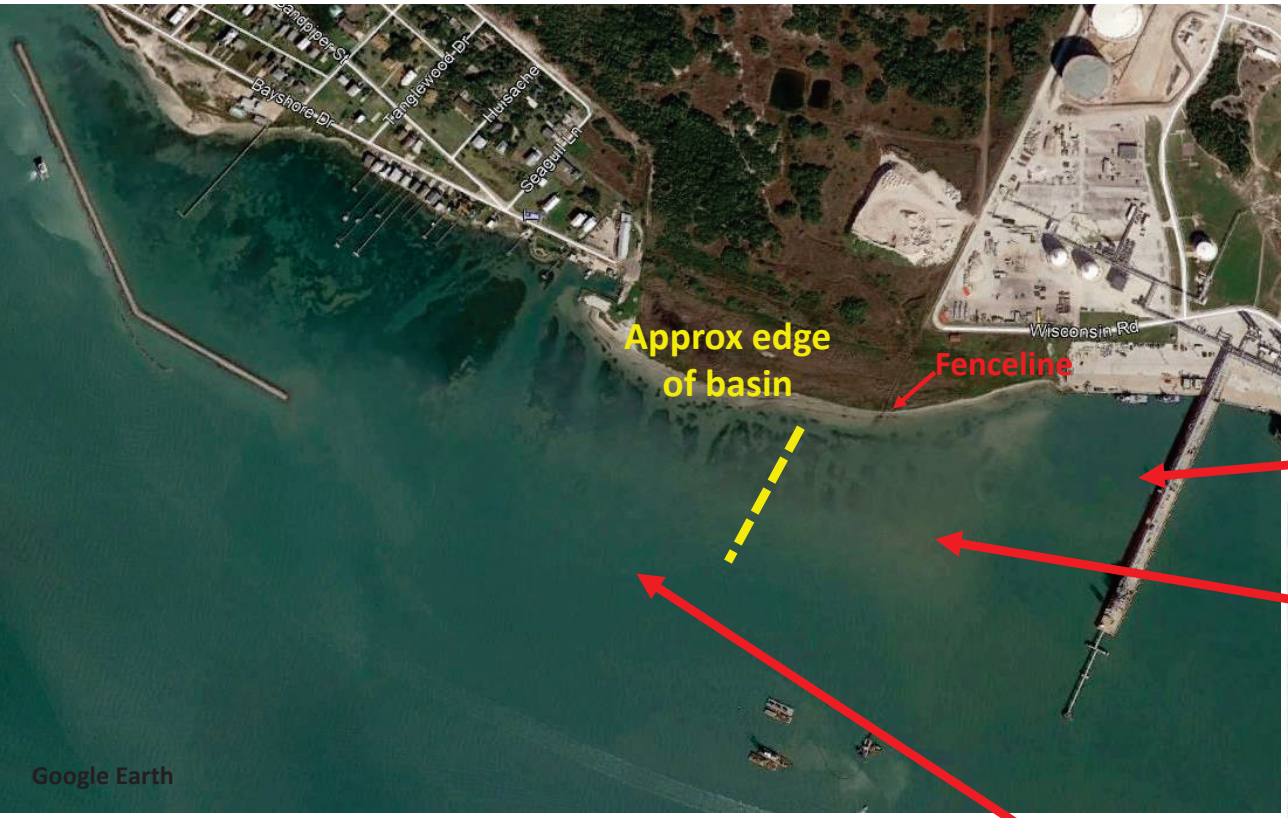

Existing Pier & West Slip

Proposed Pier

Proposed Slope Stabilization

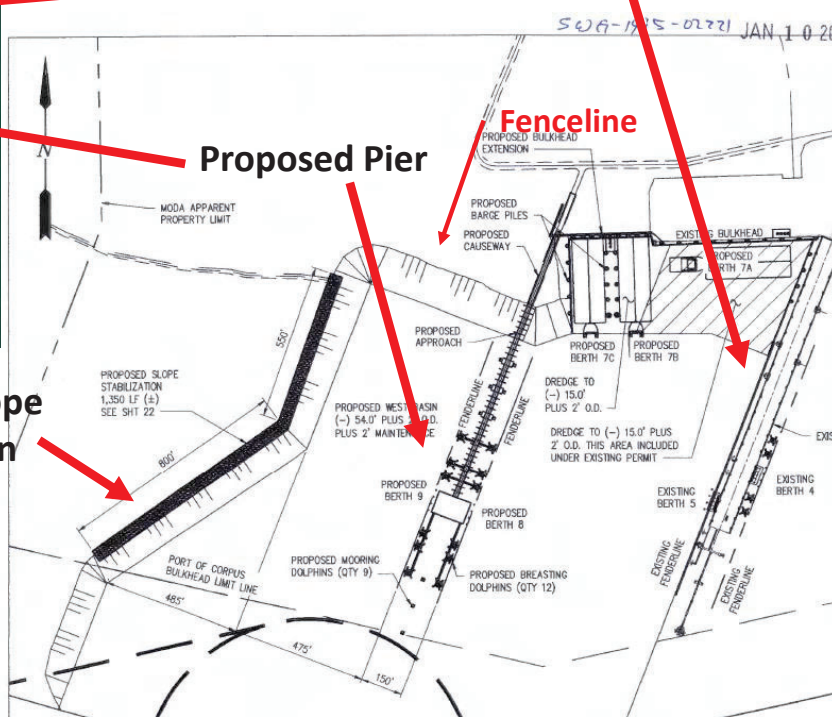

Construction Plans Impacting Seagrass Habitat

Concerns: Operational Impacts

1. Erosional impacts to seagrass from tug propwash
2. Sedimentation impacts to seagrass from tug propwash
3. Additional similar impacts from dredging, shipping wake and prop scarring

Goal:

1. Document any spatial and temporal patterns of sediment/erosion and impacts to seagrasses

Hypothesis:

1. Point source suspended sediments will result in a gradient of sediments, attenuated light conditions, and seagrass bioindicators

2016 – 2020 NAIP and 2021 UAV Imagery of Seagrass Meadow Adjacent to West Slip of Moda

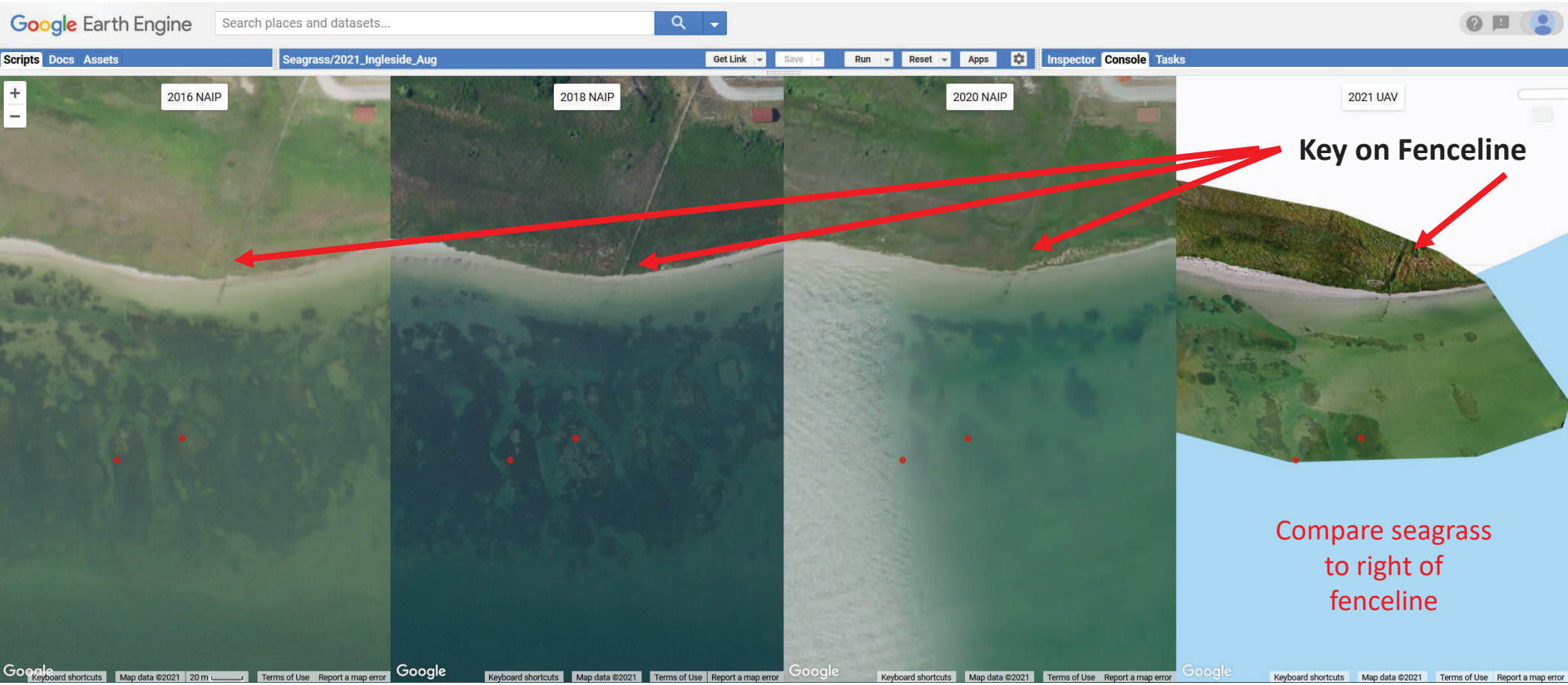

2016 NAIP **2018 NAIP** **2020 NAIP** **2021 UAV**

NAIP and UAV Imagery Credit: Hua Zhang, PhD

1:41 PM Clear Water (3 of 4 tugs visible)

Example of sediment plume generated during docking operation

Photo Credit: Patrick Nye

1:58 Silt plume and tugboats (3) propwash. Piling (Yellow) is reference point.

sediment plume front 1

Red arrow indicates plume front

Photo Credit: Patrick Nye

2:23PM Silt plume approaching piling 1853’ from edge of docking channel.

sediment plume front 3

Photo Credit: Patrick Nye

3:14 PM silt plume has expanded to 2334’ in one hour forty-three minutes.

Sediment plume (4) has reached homeowner’s shoreline

Photo Credit: Patrick Nye

Map of 12-2020 Sampling Sites: Seagrass Bioindicators

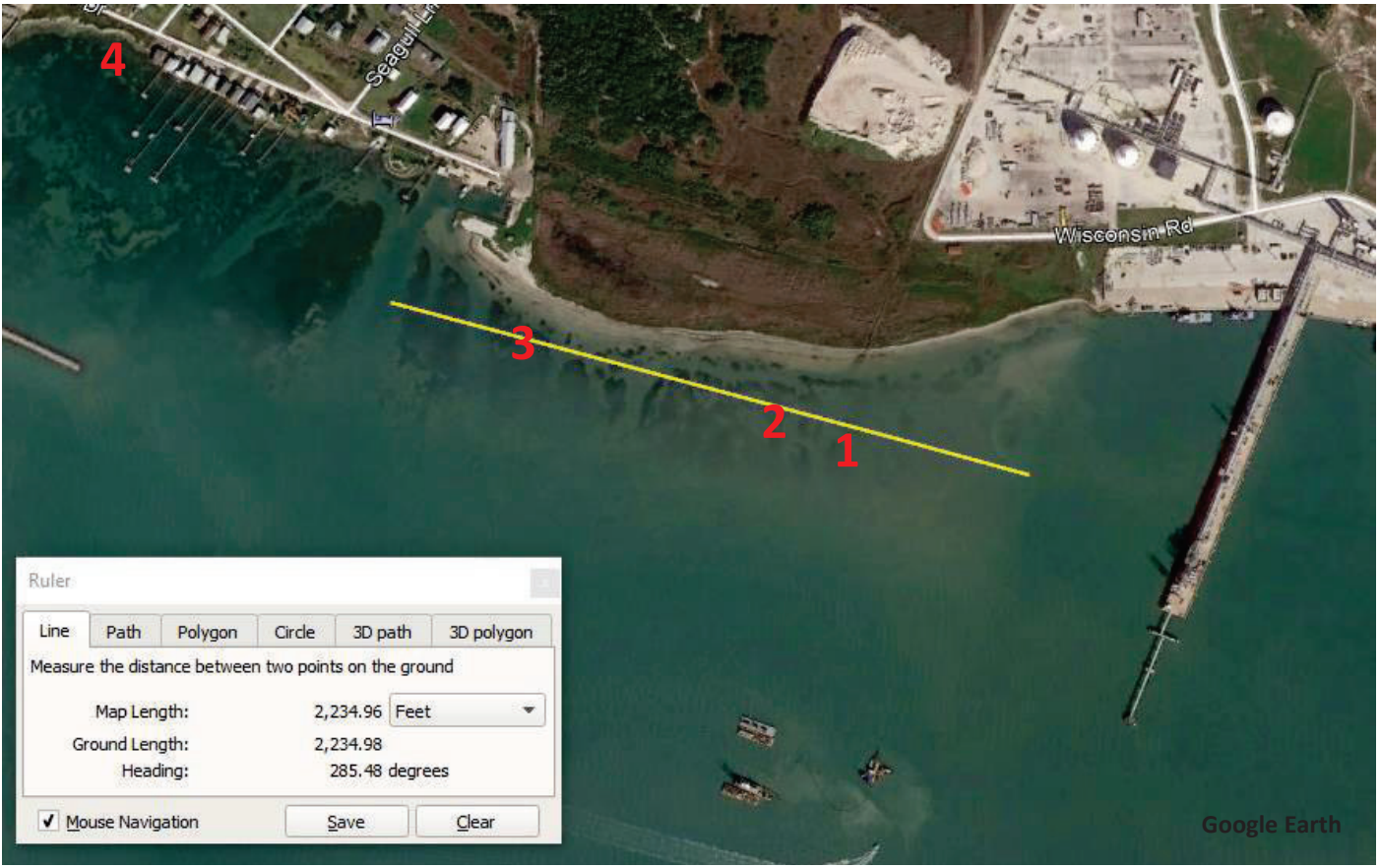

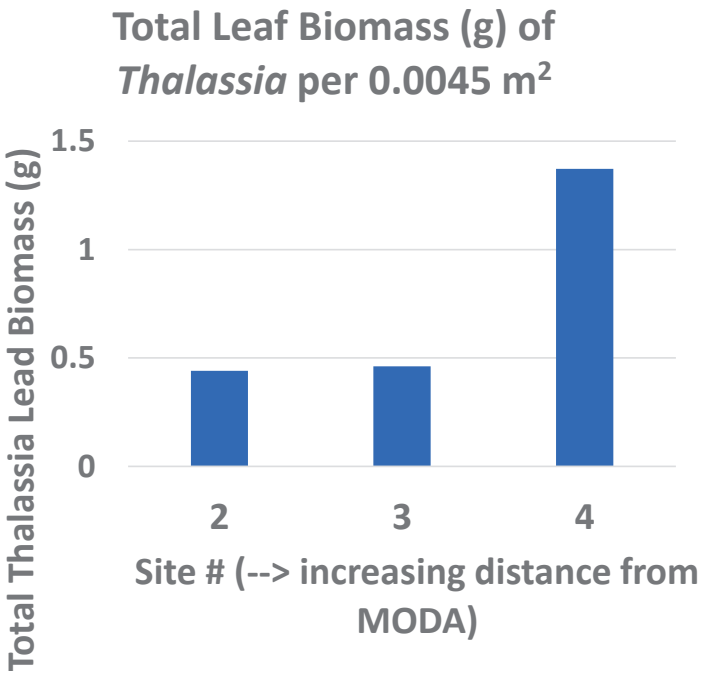

June 2021: Light Loggers and Sediment Traps

- **Measure light attenuation integrated over whole day and changing environmental conditions**
- **Measure light received at seagrass canopy level**

Depths across all seasons

(note: 1_2 measured from diff depths)

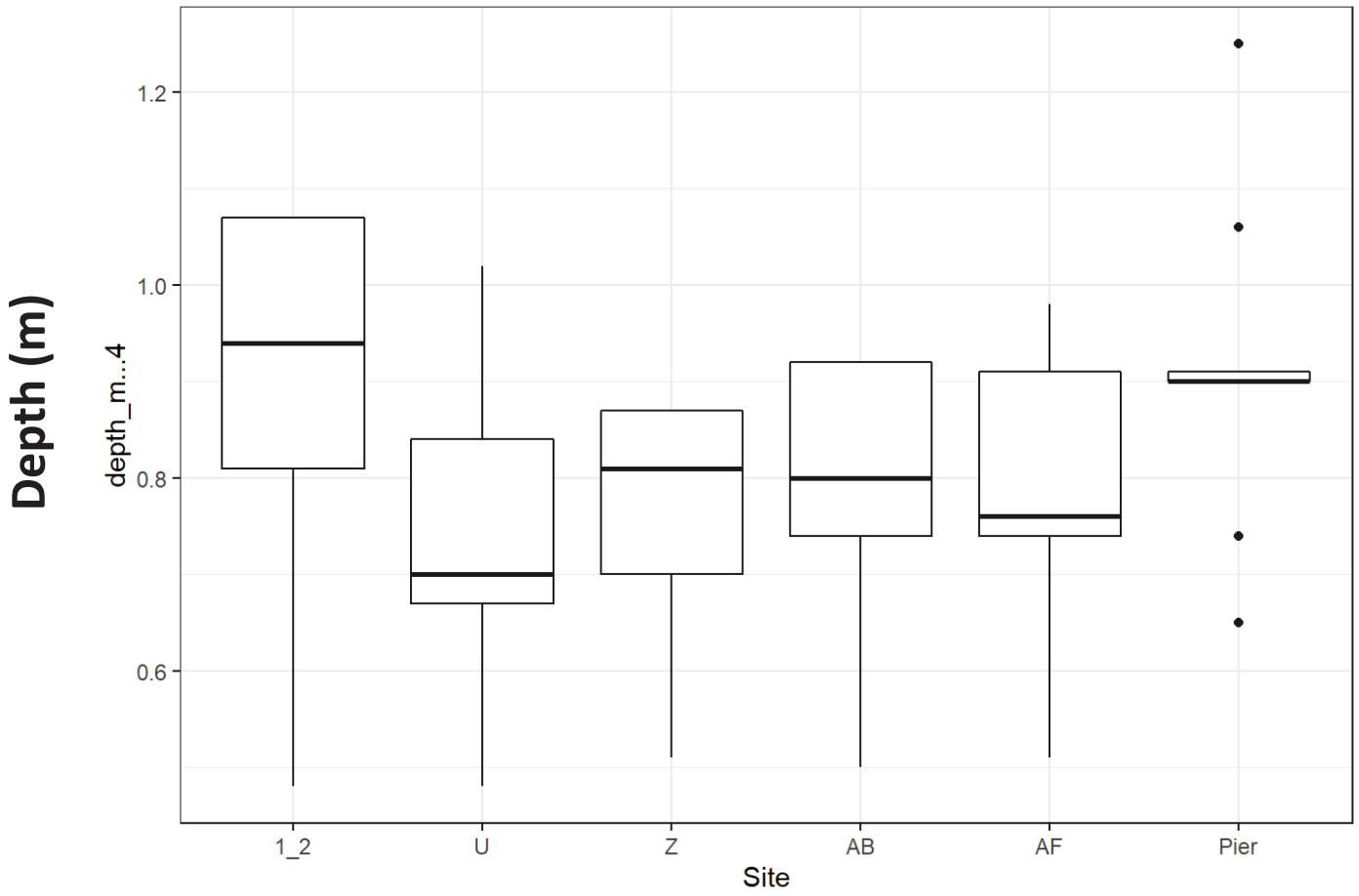

Light Levels from Loggers During a Docking Event

(Top Loggers deployed 49 cm above bottom)

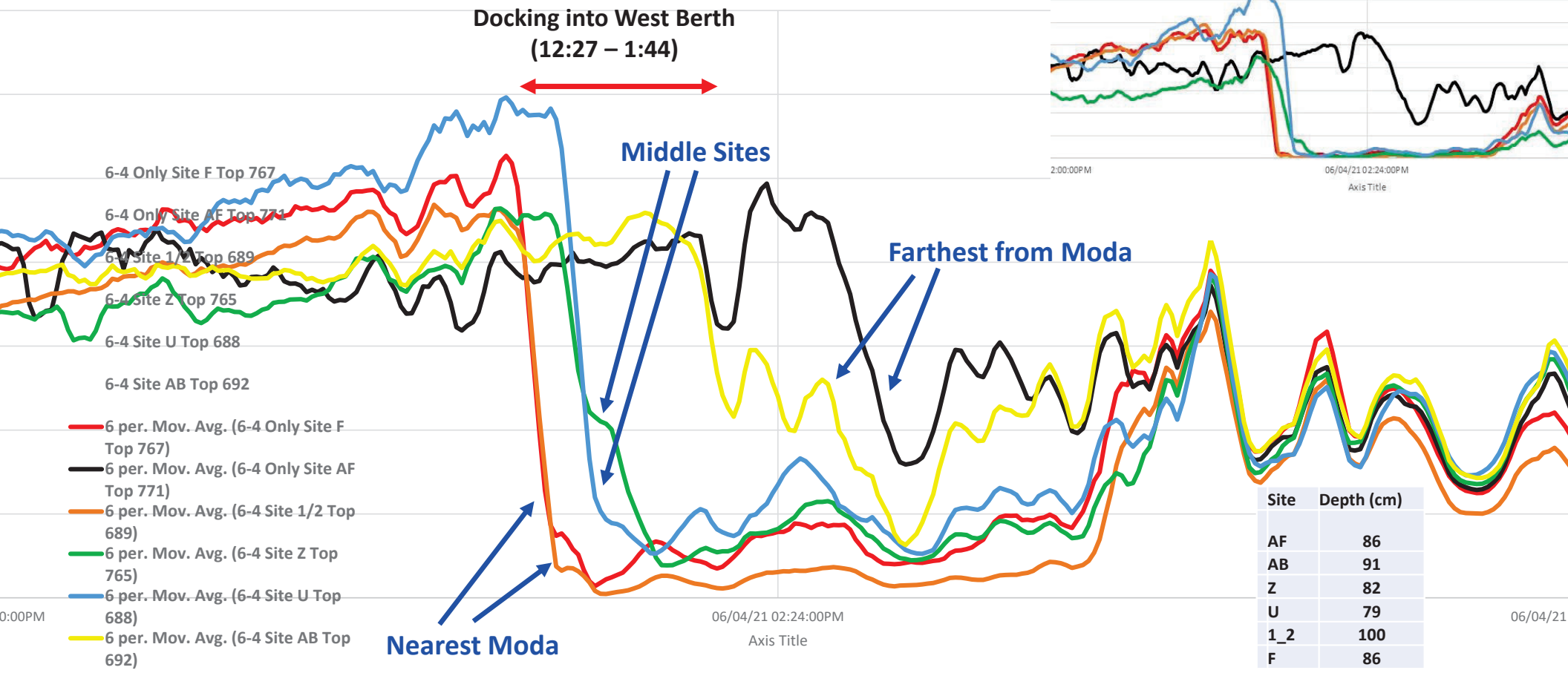

Bottom Loggers
(17 cm above Bottom)

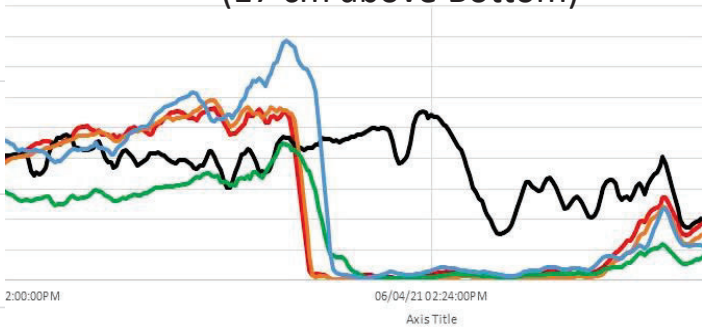

Site	Depth (cm)
AF	86
AB	91
Z	82
U	79
1_2	100
F	86

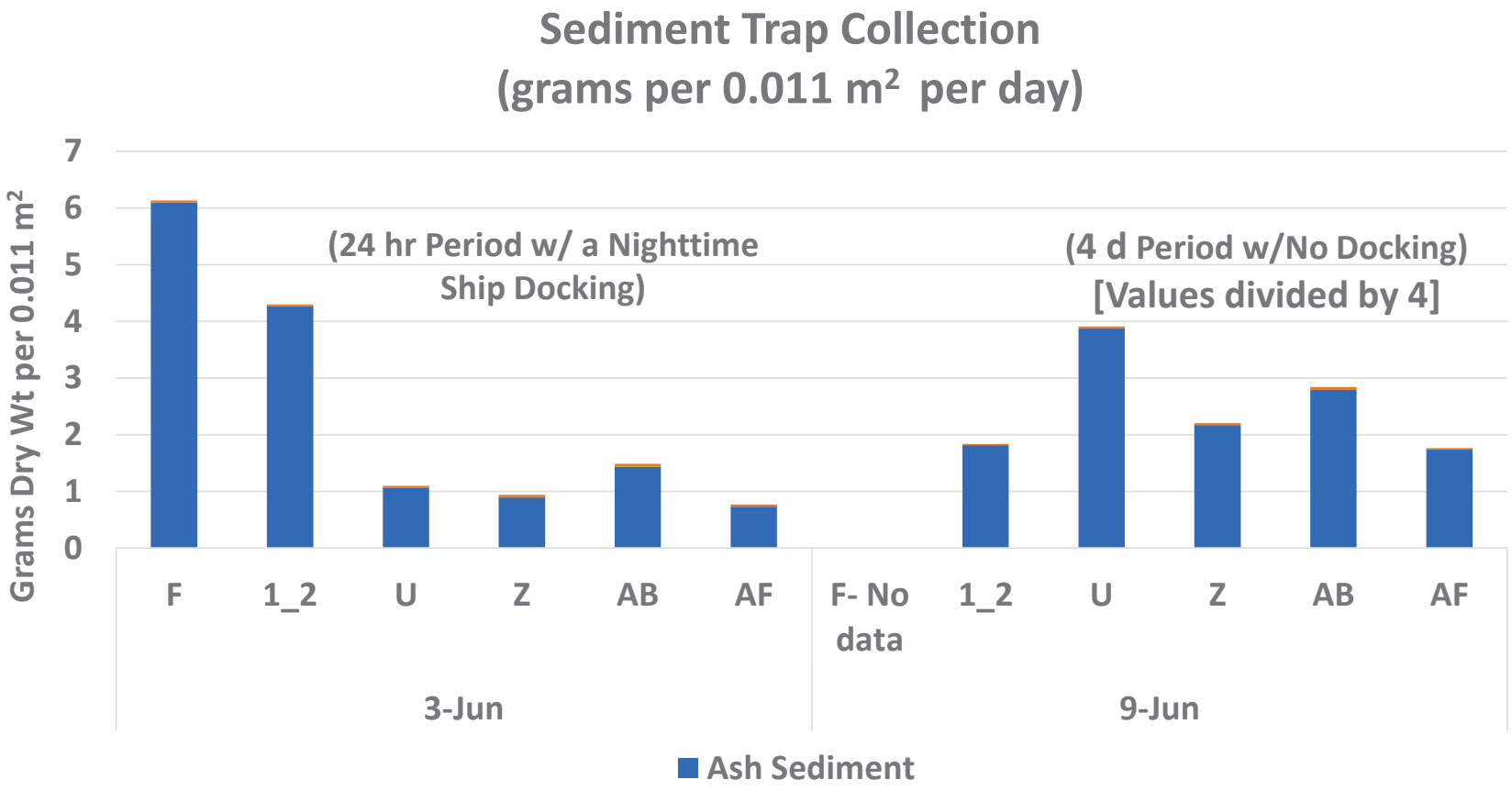
Sediment Trap Collection
(grams per 0.011 m² per day)
Grams Dry Wt per 0.011 m²
7
6
5
4
3
2
1
0
(24 hr Period w/ a Nighttime Ship Docking)
(4 d Period w/No Docking)
[Values divided by 4]
F
1_2
U
Z
AB
AF
F- No data
1_2
U
Z
AB
AF
3-Jun
9-Jun
Ash Sediment

Total Suspended Solids (TSS) and % TSS as Organic

(Yellow is F-Site water Sample Taken During Undocking on 8-3-21)

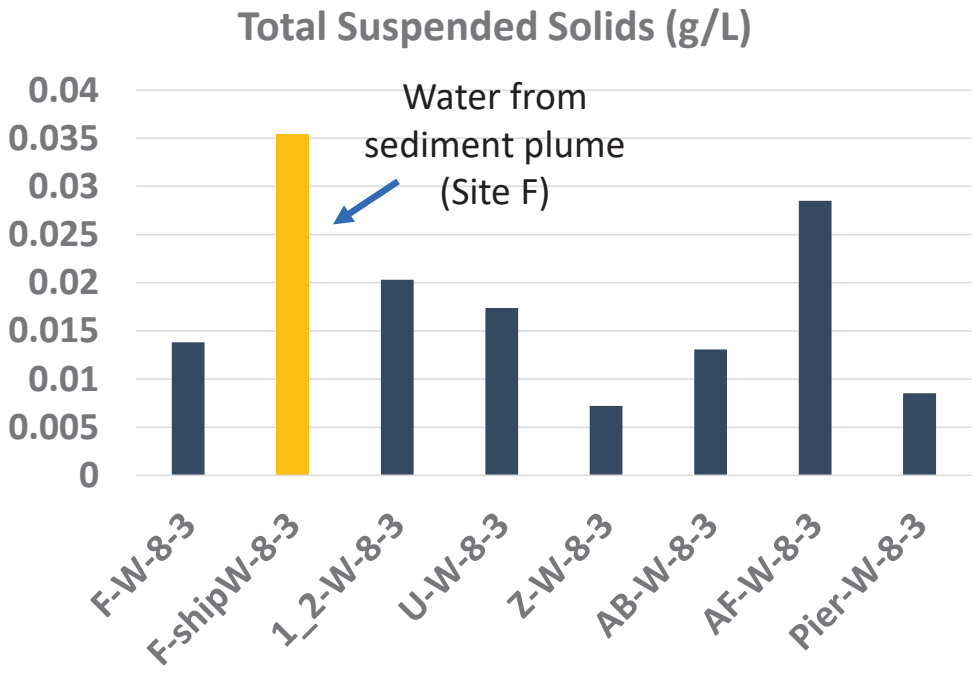

2.6-Fold more TSS during undocking, and salinity increased from 27.5 → 31.5

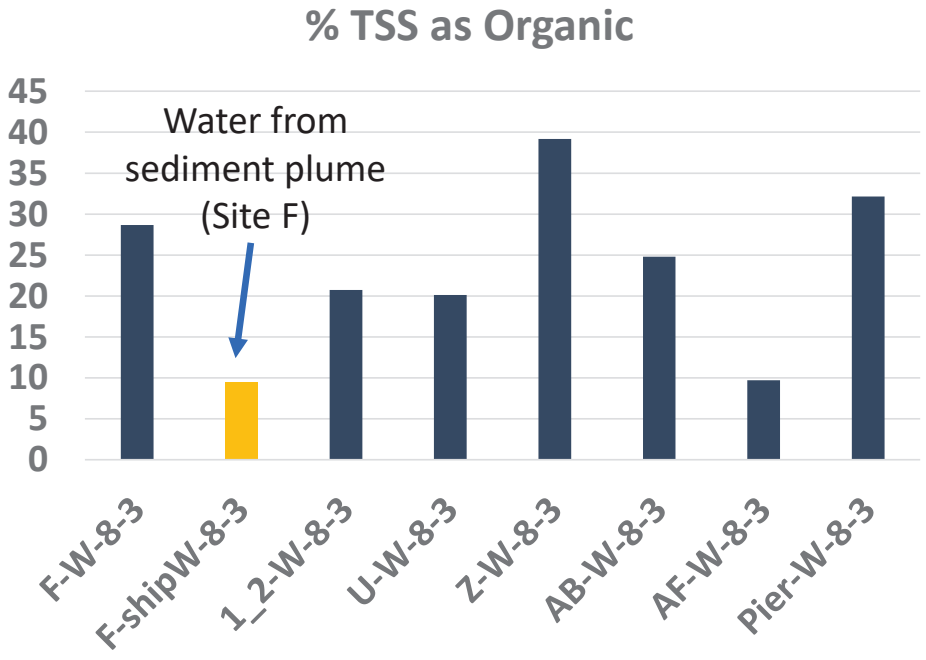

Less organic content in sediment plume (= more sand)

Seagrass Bioindicators – Jun - Nov 2021 Sampled all SG by “Ring”

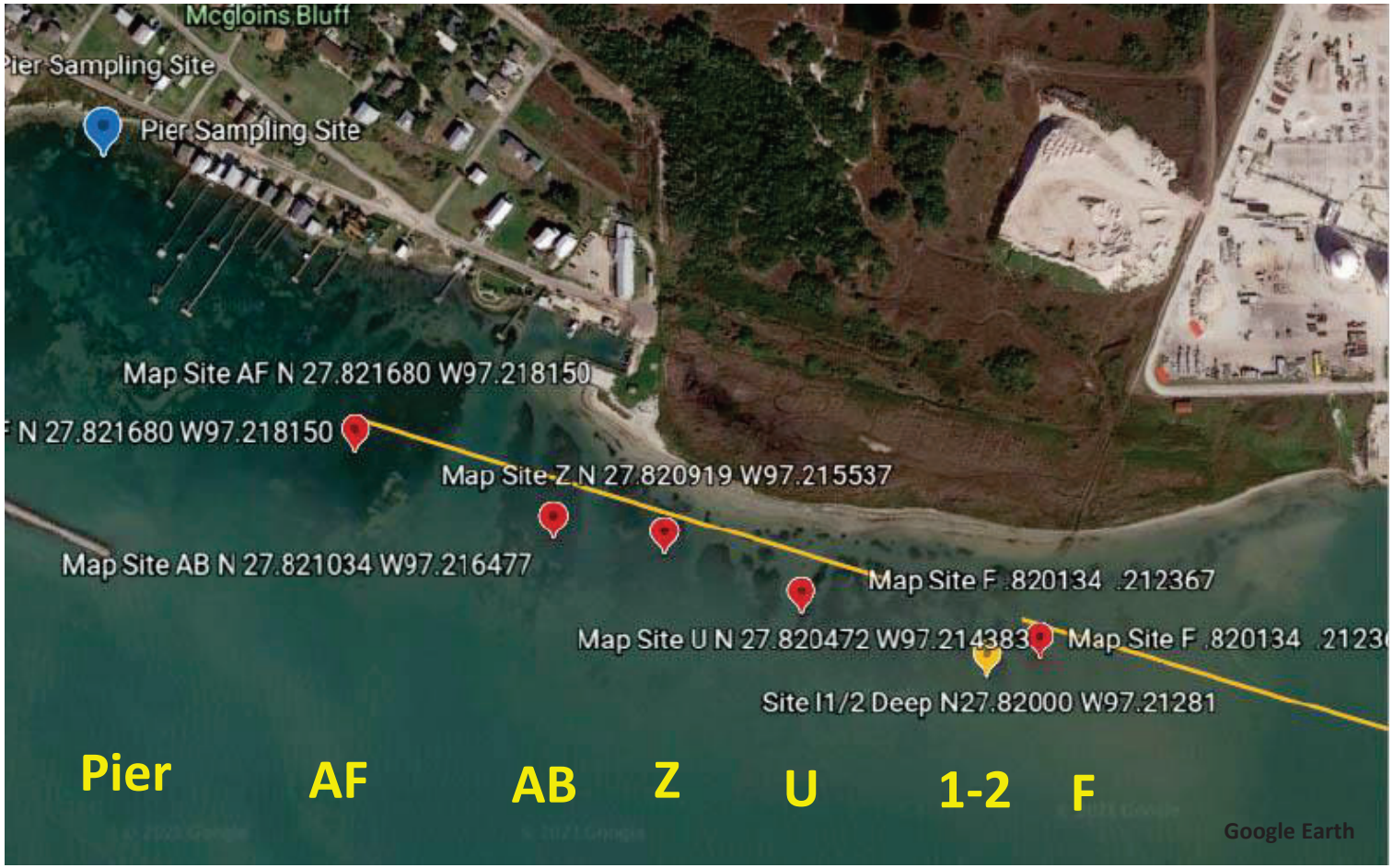

Bioindicators of the seagrass beds: August SG Canopy Height

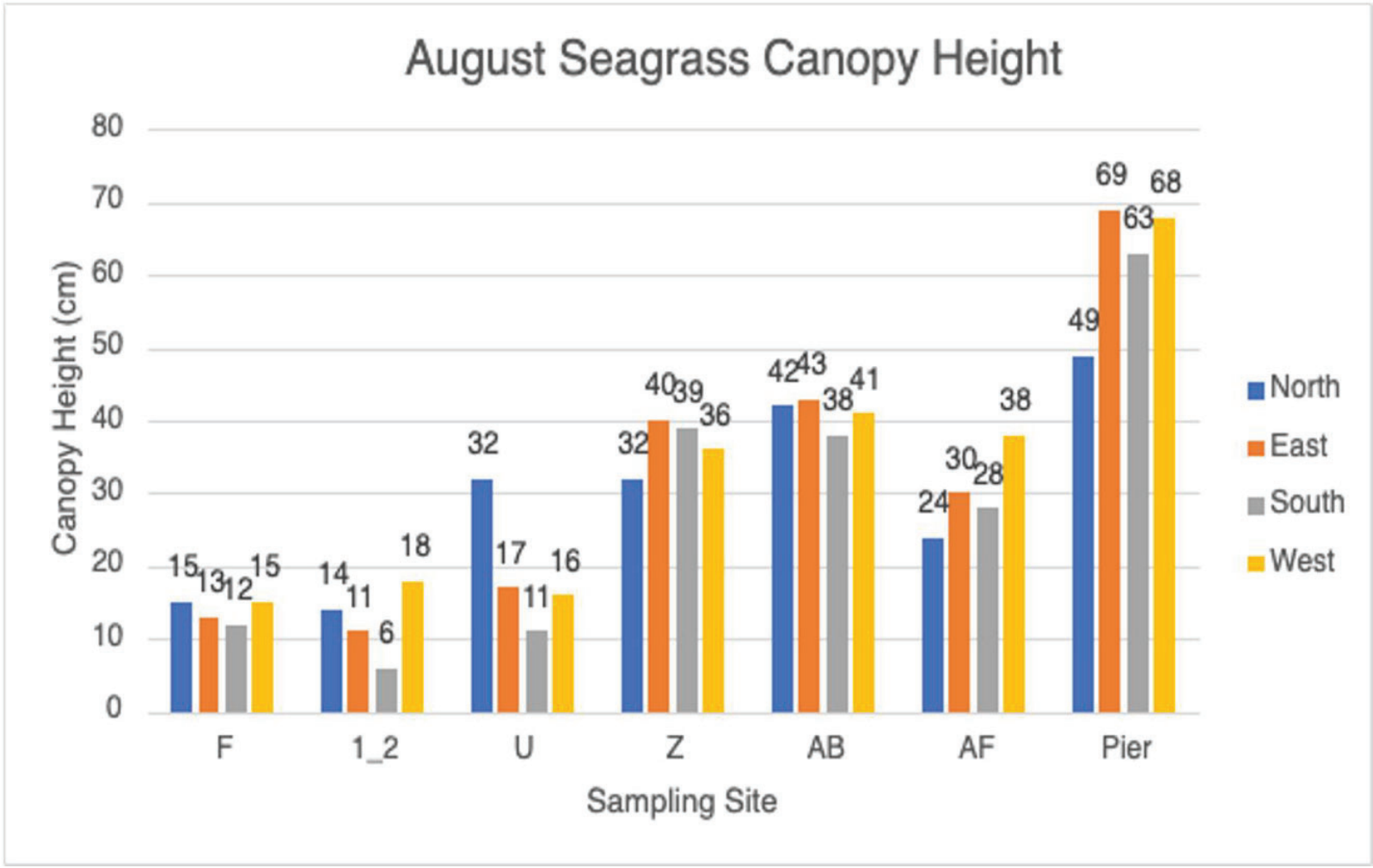

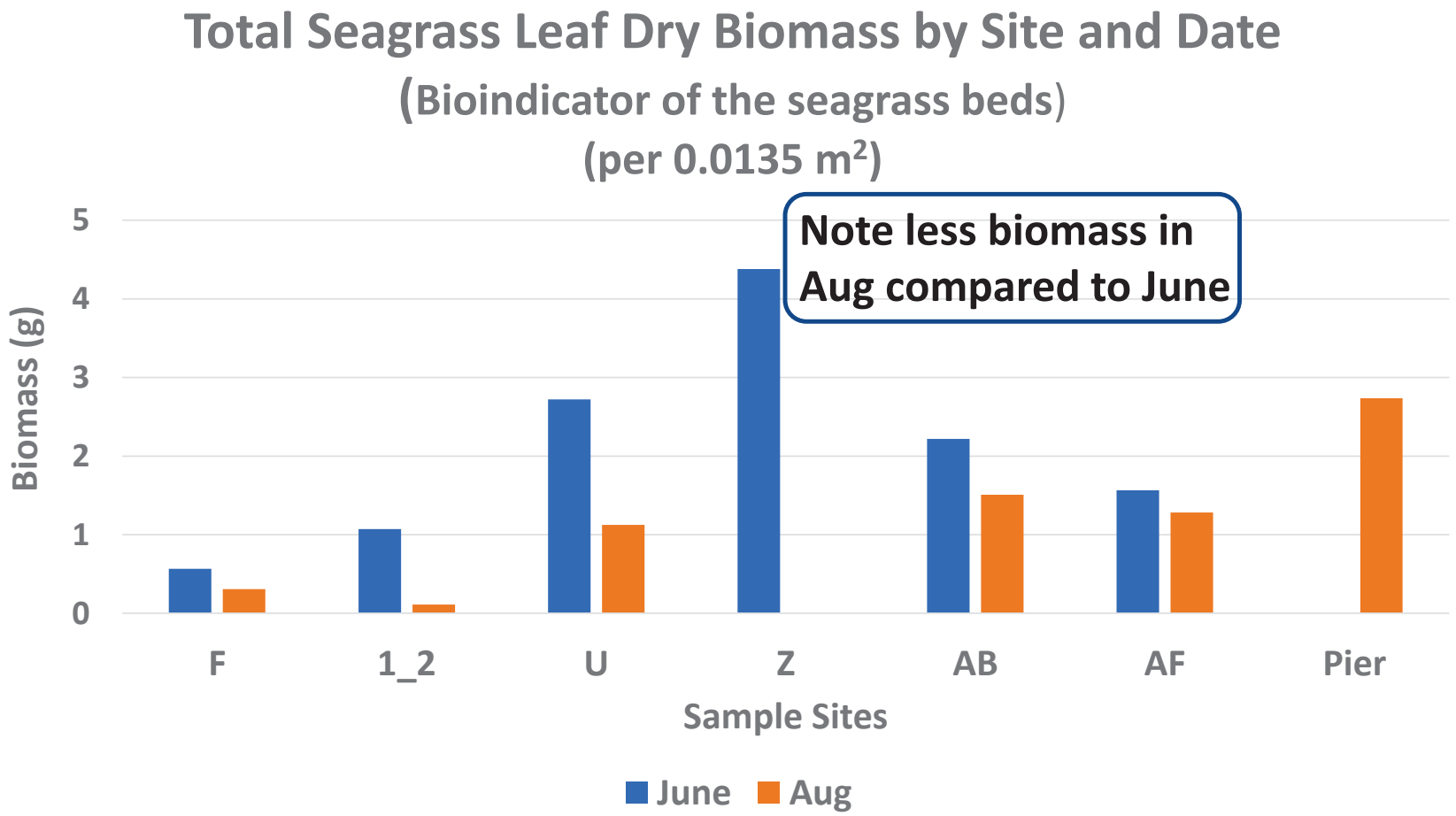

Other June bioindicators very consistent w/biomass

Other August bioindicators less consistent → suggests changing system?

Bioindicators of the seagrass beds

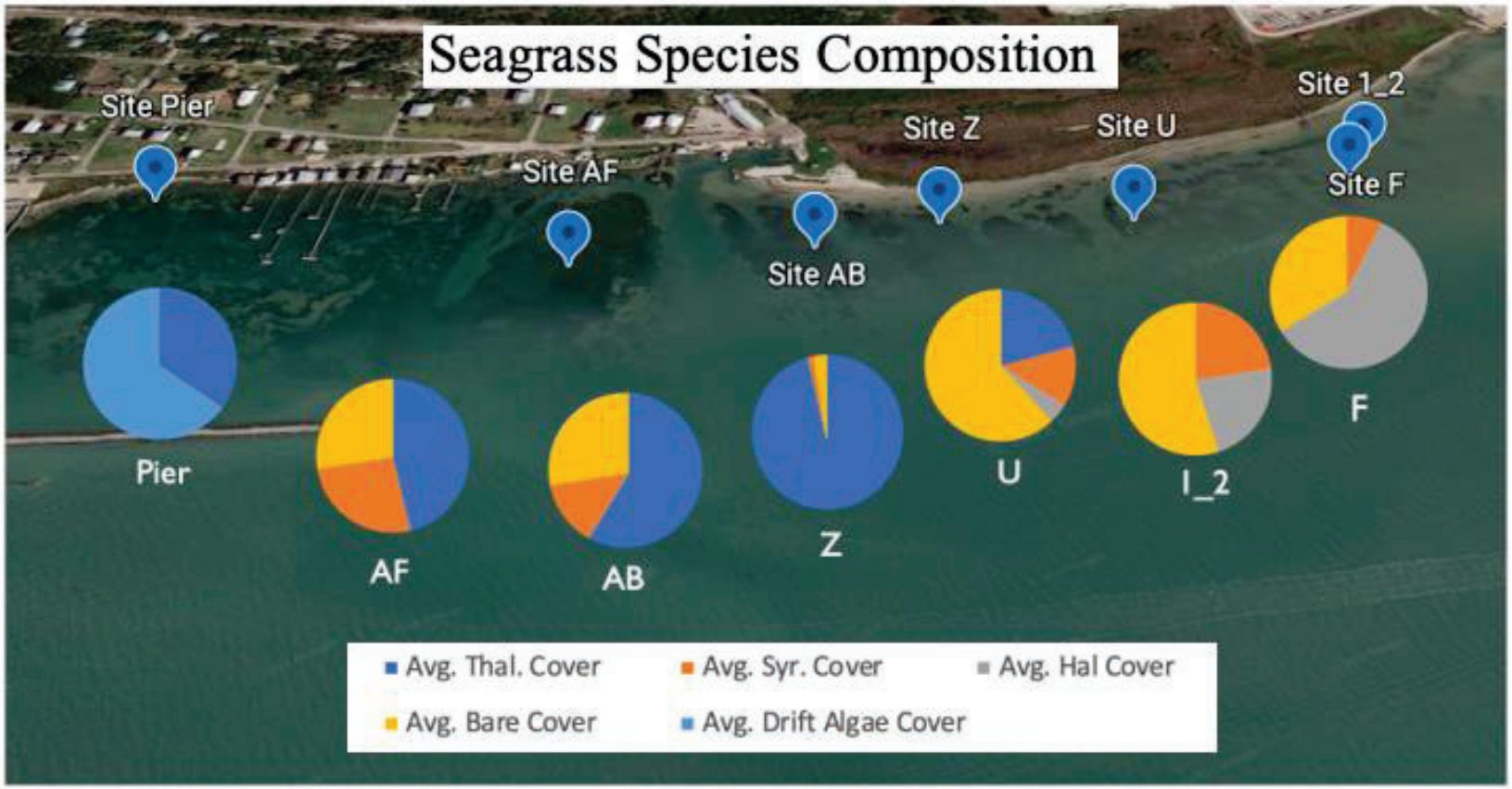

Seagrass Species Sampled and Shoot Density By Site (Bioindicator of the seagrass bed) (June 2021) (per 0.0135 m^2)

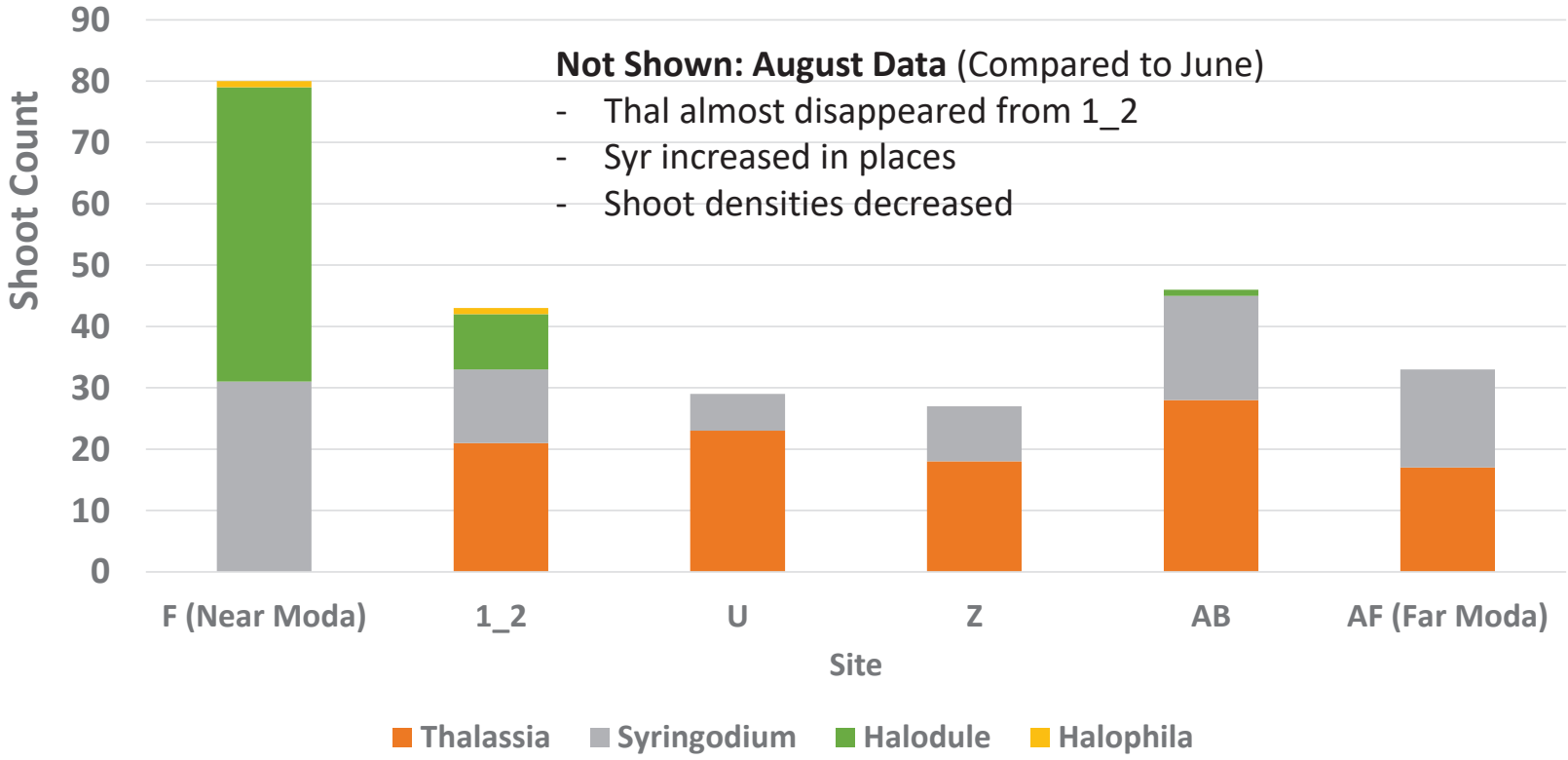

Not Shown: August Data (Compared to June)

- Thal almost disappeared from 1_2
- Syr increased in places
- Shoot densities decreased

[Turtle; Manatee; Shoal; Clover]

Comparison of Just *Thalassia* Across Sites: Leaf Wt and Epiphyte Wt

(Bioindicators of the plants)

Complicated by different numbers of shoots per ring

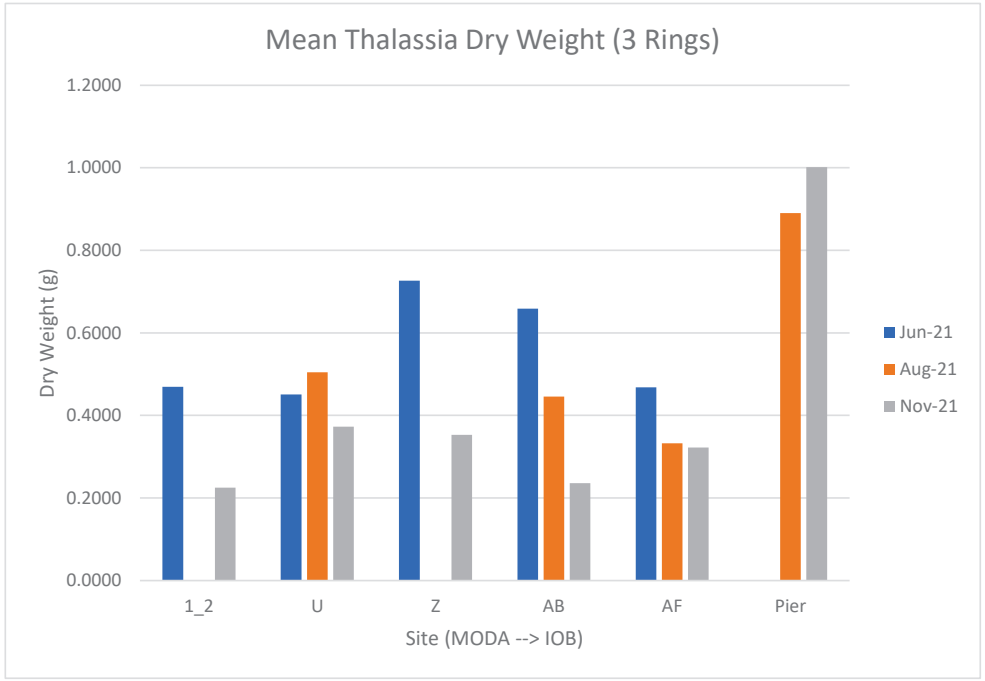

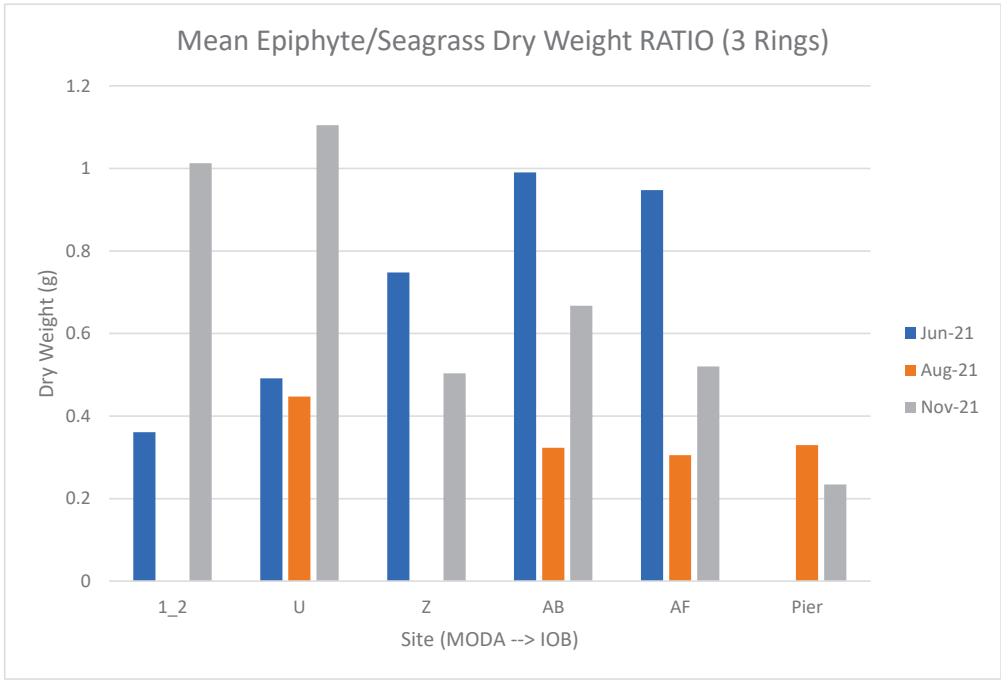

Seagrass *Plant* Bioindicators – Jan - June 2022 Sampled just *Thalassia* (Compared 5 whole shoots)

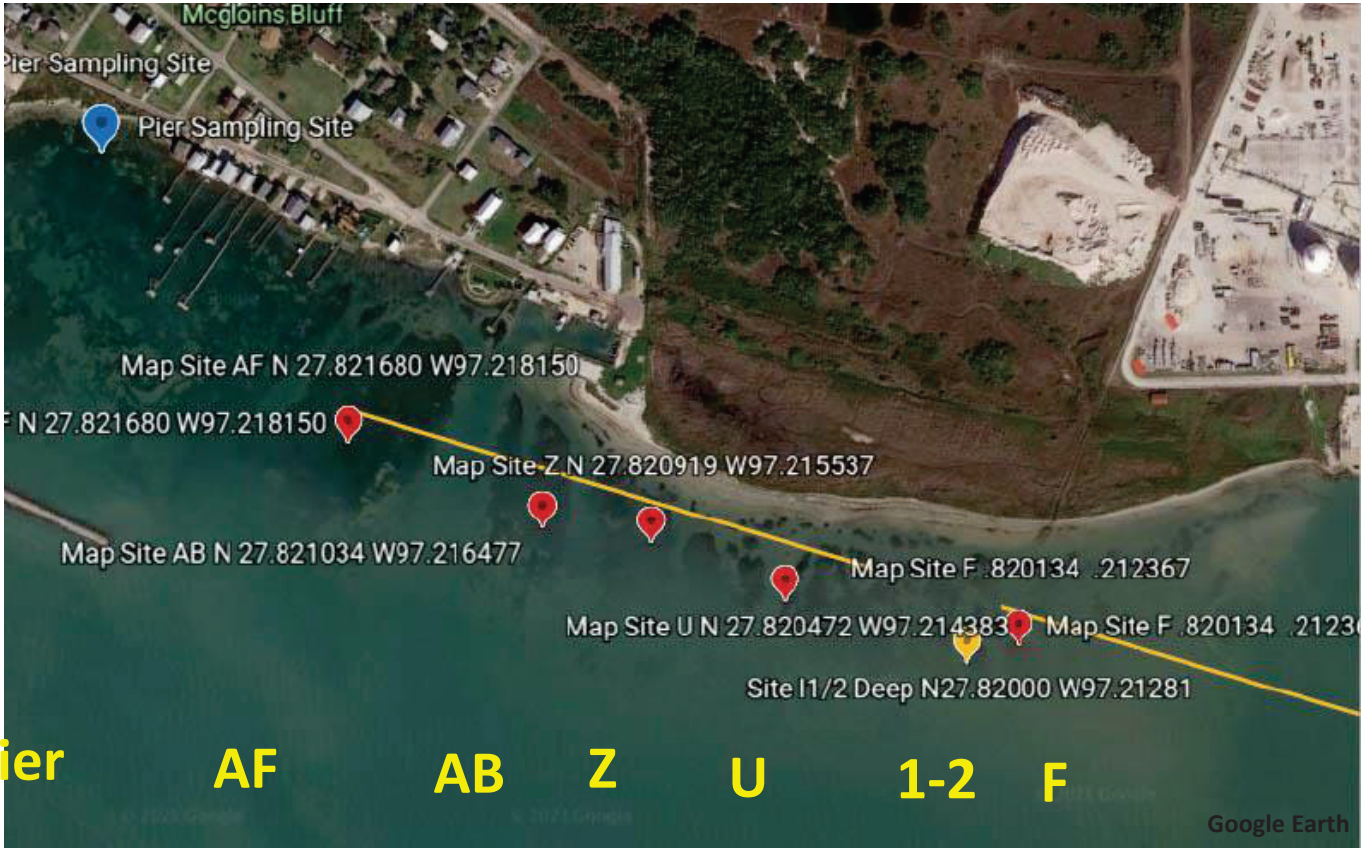

Comparison of Just *Thalassia* Across Sites: Leaf Wt and Epiphyte Wt for 5 Whole Shoots (Bioindicators of the plants)

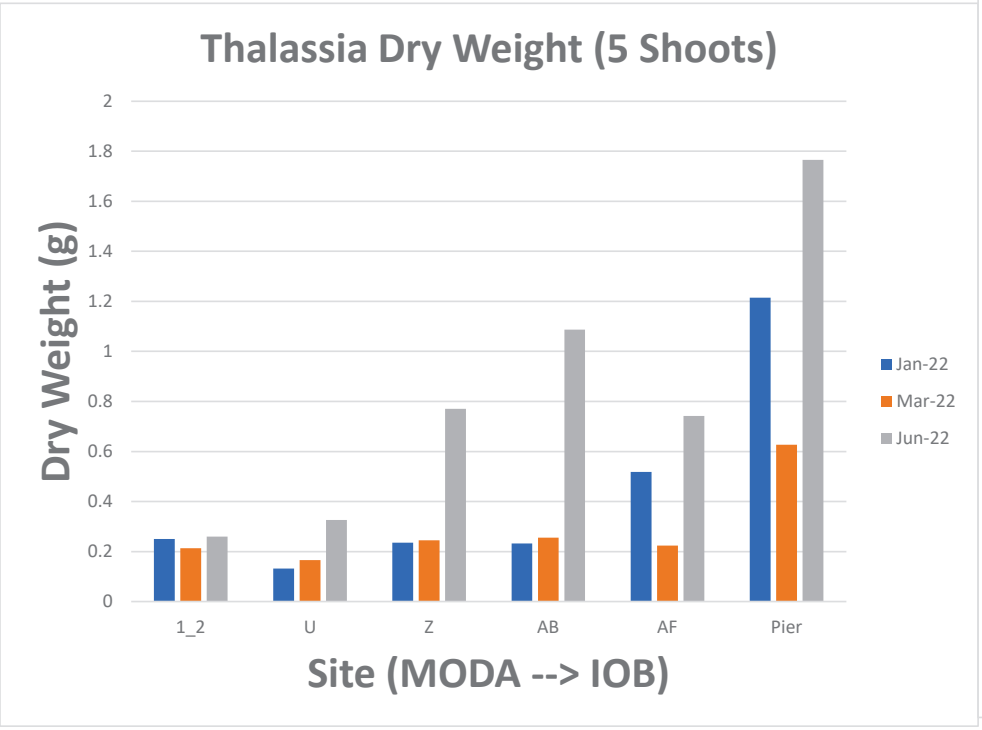

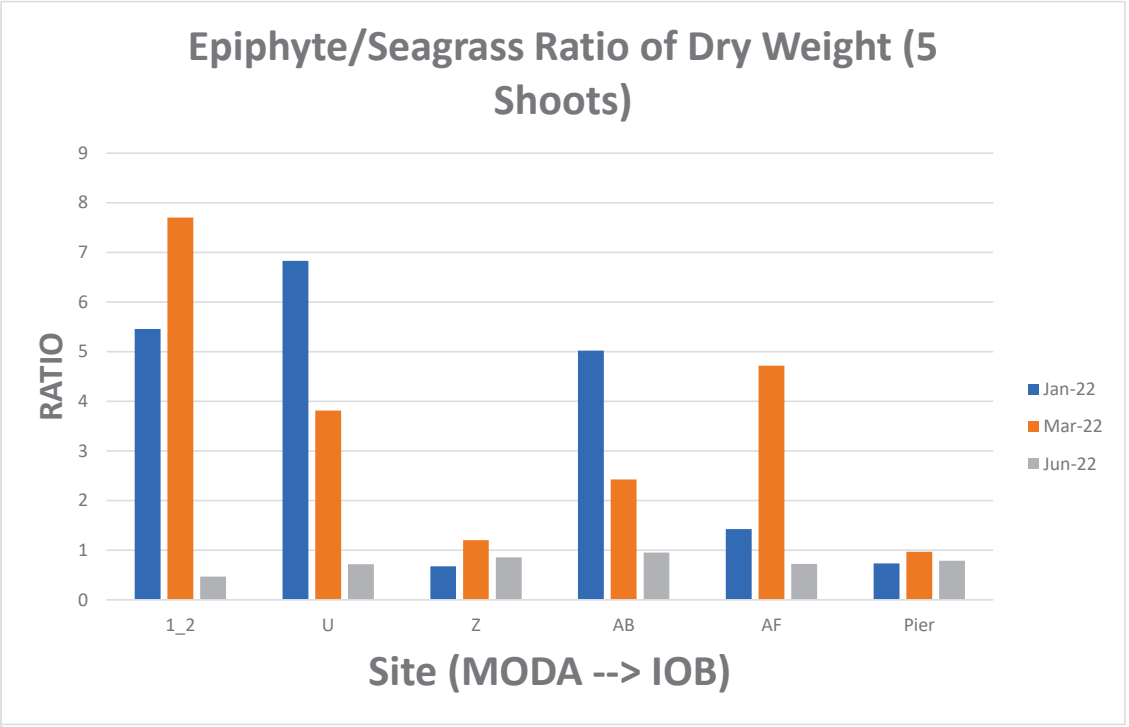

Comparisons across all seasons: Compare *by shoot* due to different sampling strategies (Ring vs 5 Shoots)
Mean Leaf Area

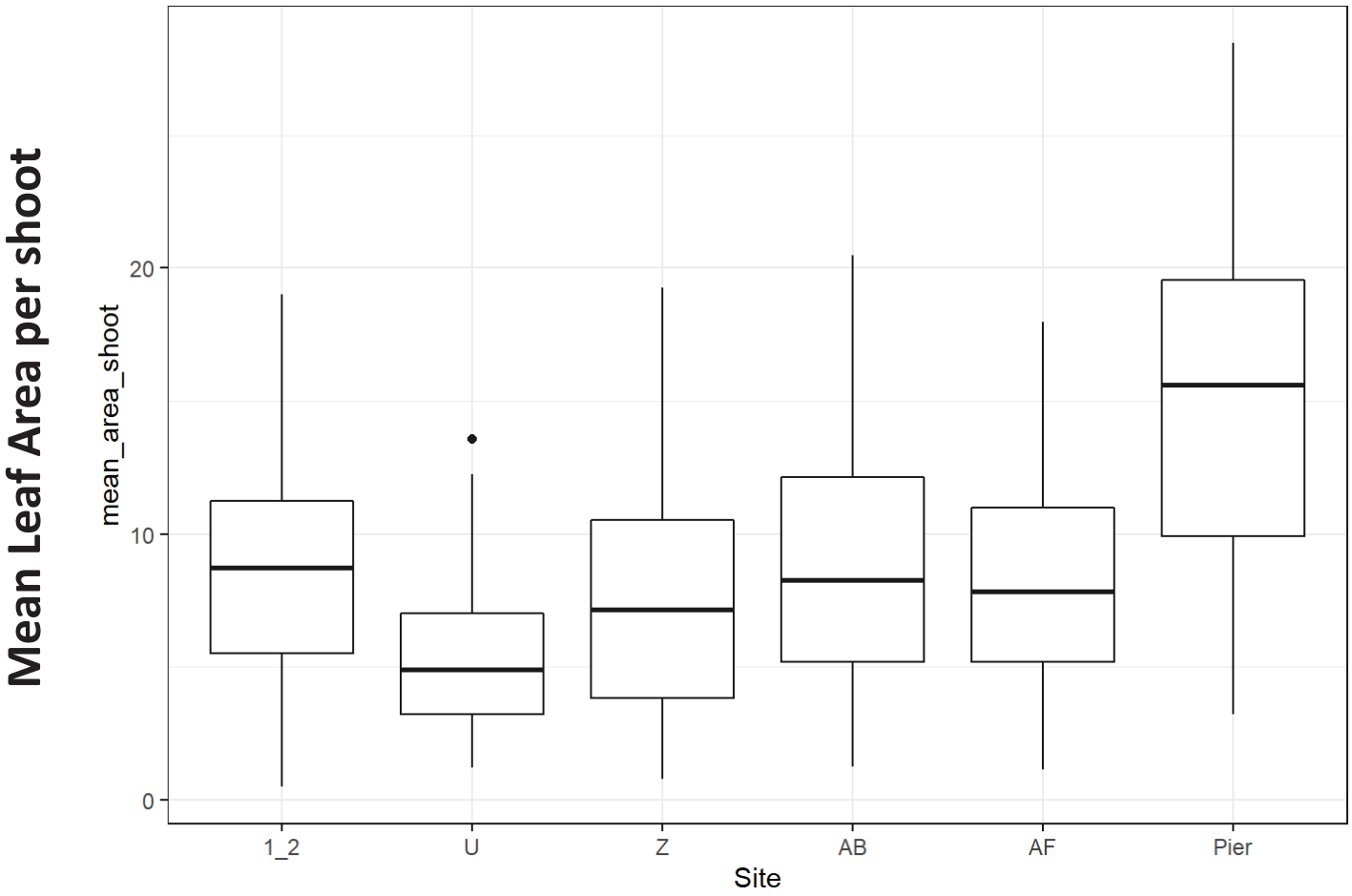

Comparisons across all seasons: Compare *by shoot* due to different sampling strategies (Ring vs 5 Shoots)
Mean Leaf AreaTotal Leaf Area

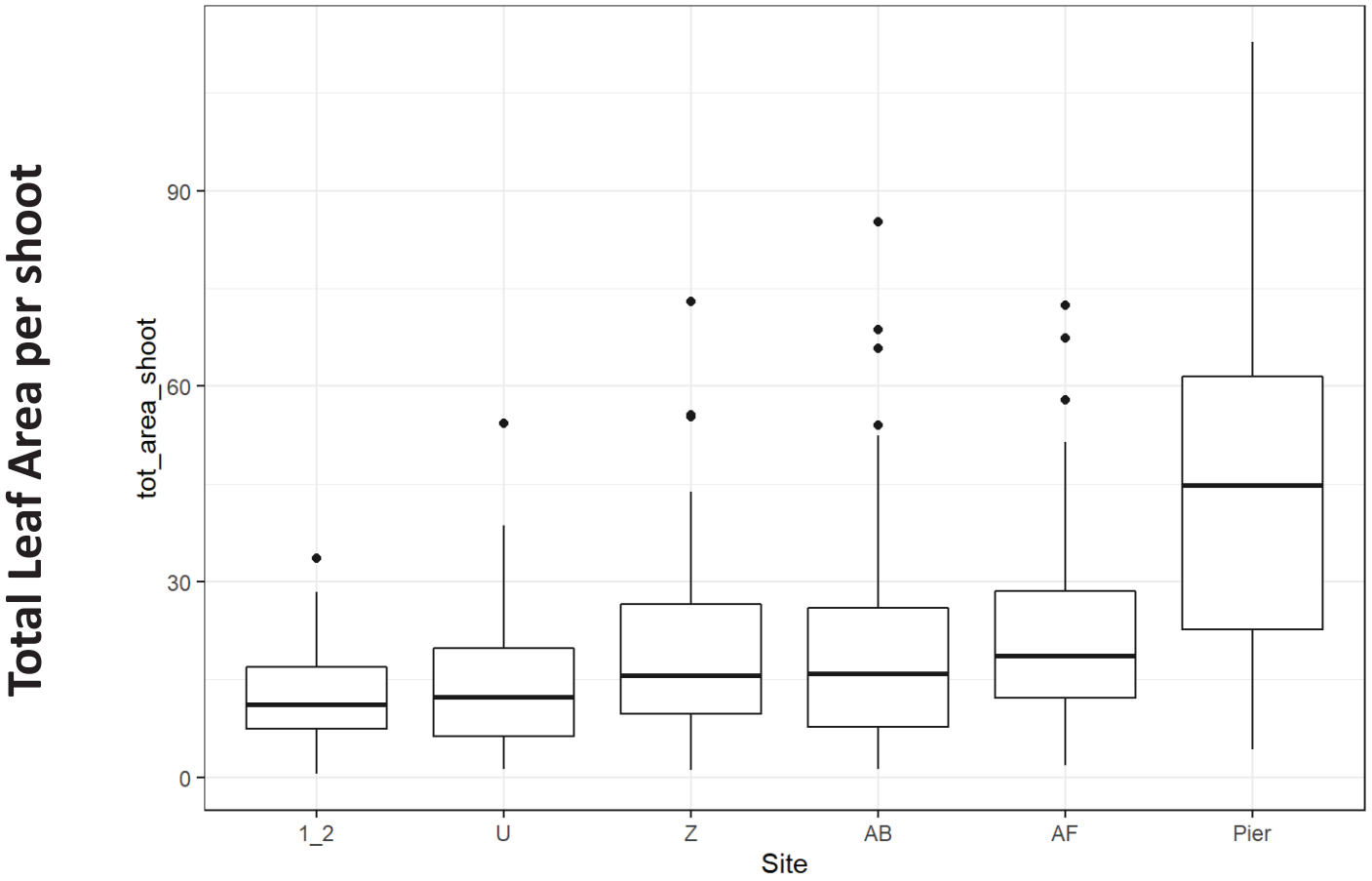

Comparisons across all seasons: Compare *by shoot* due to different sampling strategies (Ring vs 5 Shoots)
Leaf Wt and Epiphyte Wt for 5 Whole Shoots

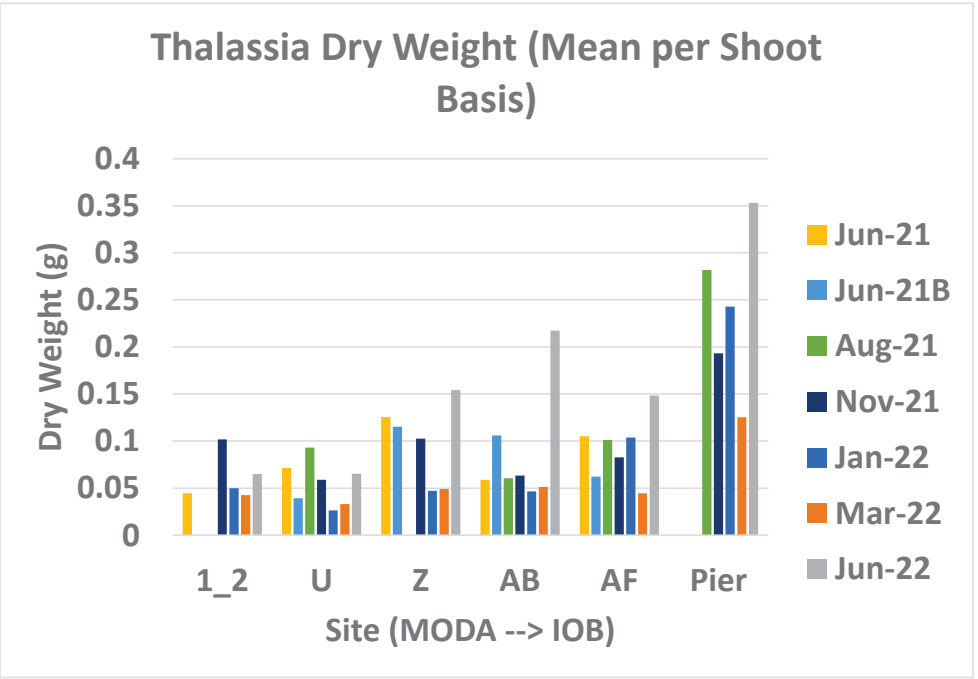

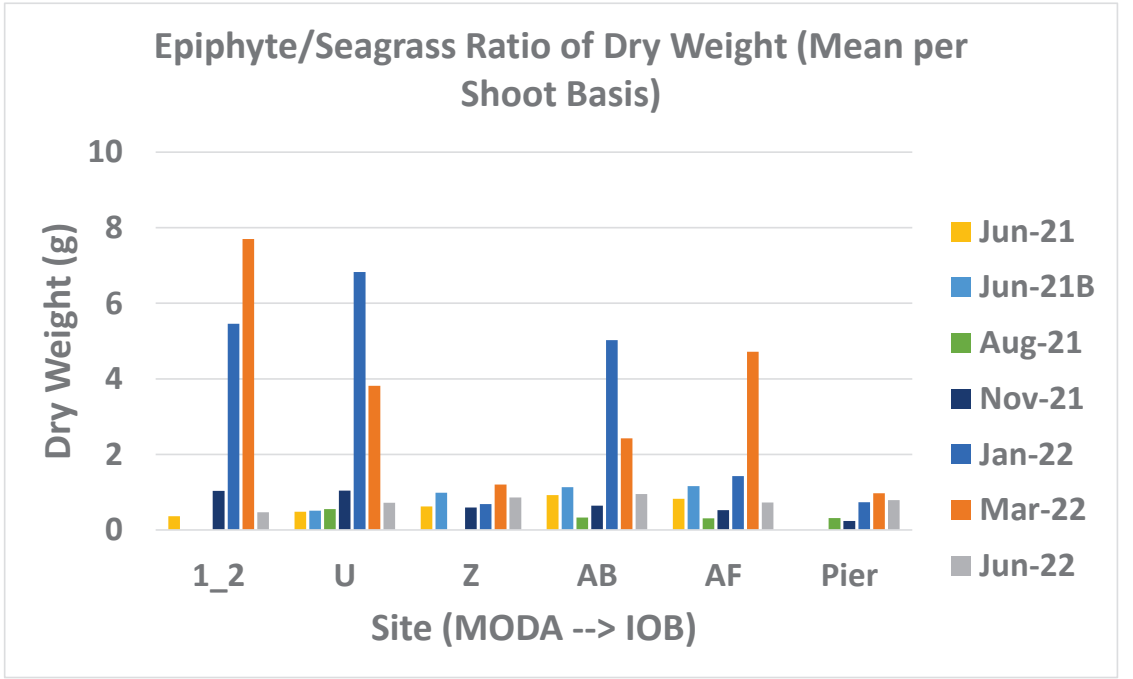

mean SG leaf area for June 2021 to June 2022 comparisions (For all ANOVA p-values are significant at < 0.05, and marginally significant at p < 0.01)

Mean leaf area per shoot in June 2021

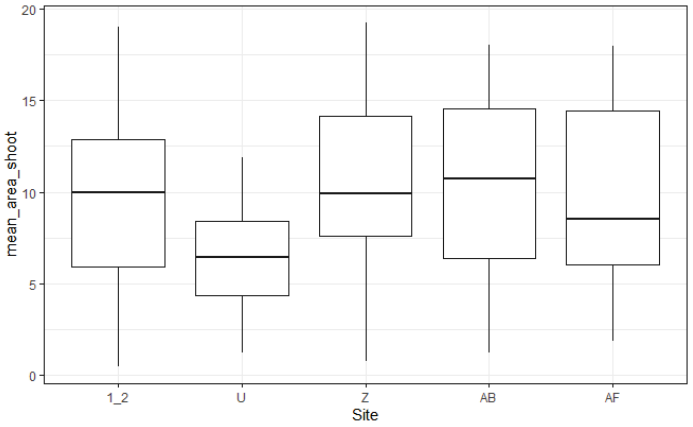

-U Site significantly smaller leaf area than AB and Z sites.
-Z site only significantly greater than U

Mean leaf area per shoot in June 2022

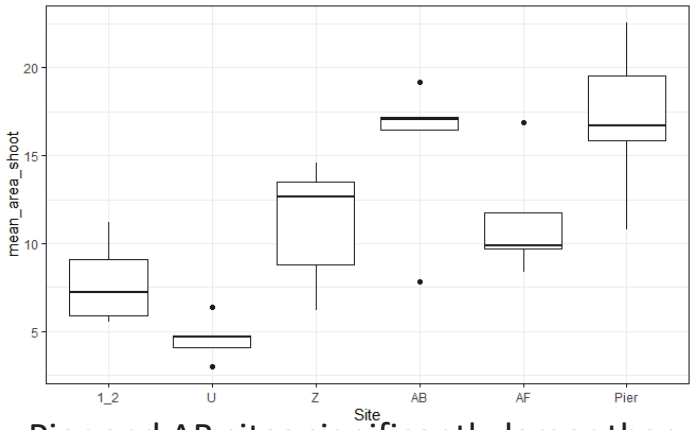

Pier and AB sites significantly larger than U and 1_2 sites.

U site significantly smaller than Z and AF sites as well.

Numbers on the left vertical Axis are the mean of (mean leaf area per shoot) per site for the Jun 2021 samplings

The Horizontal Axis is the location of study sites.

Starting from the left side being the closest to MODA slip, and the right side being furthest.

SG Biomass June 2021 June 2022 comparisions

Numbers on the left vertical Axis are the mean SG biomasses per Site
The Horizontal Axis is the location of study sites.

Starting from the left side being the closest to MODA slip, and the right side being furthest.

June 2022 Seagrass Biomass

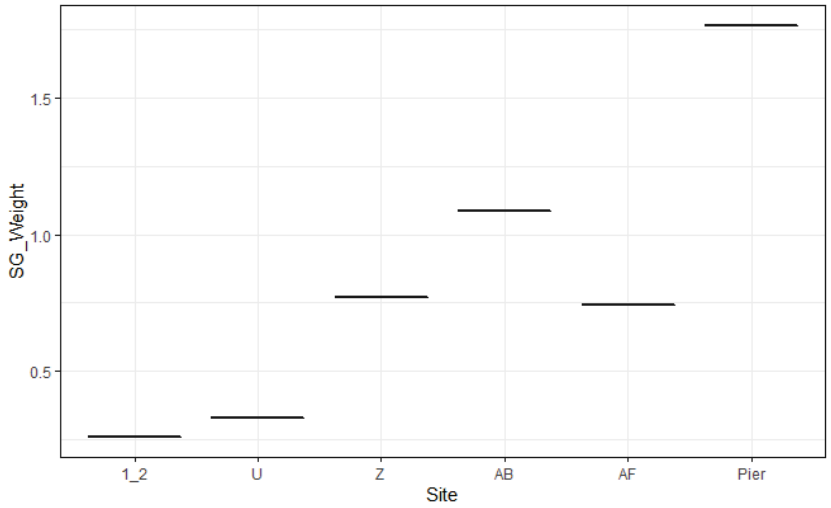

Pier Site significantly larger Biomass than other sites.

1_2 and U sites significantly smaller biomass than AB and Pier Sites

June 2021 Seagrass Biomass

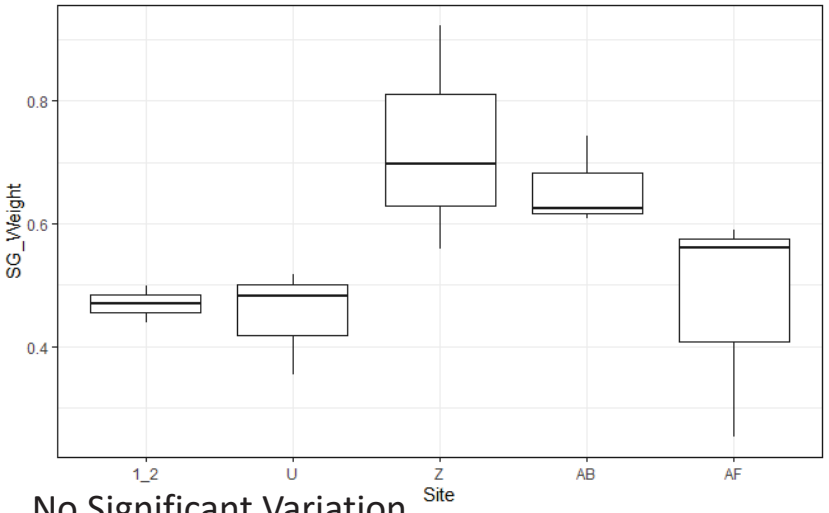

No Significant Variation

Epiphyte/Seagrass ratio for June 2021 to June 2022

Numbers on the left vertical Axis are the mean Epiphyte/Seagrass ratios.
The smaller the number, the less epiphyte and more seagrass

The Horizontal Axis is the location of study sites.

Starting from the left side being the closest to MODA slip, and the right side being furthest.

Epiphyte/Seagrass Biomass Ratio June 2022

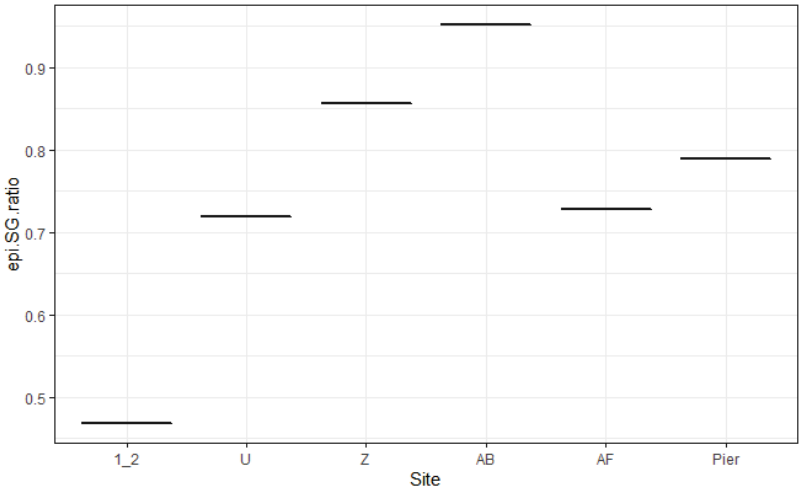

1_2 site has a significantly smaller ratio of Epiphyte to Seagrass than the other sites.

Epiphyte/Seagrass Biomass Ratio June 2021

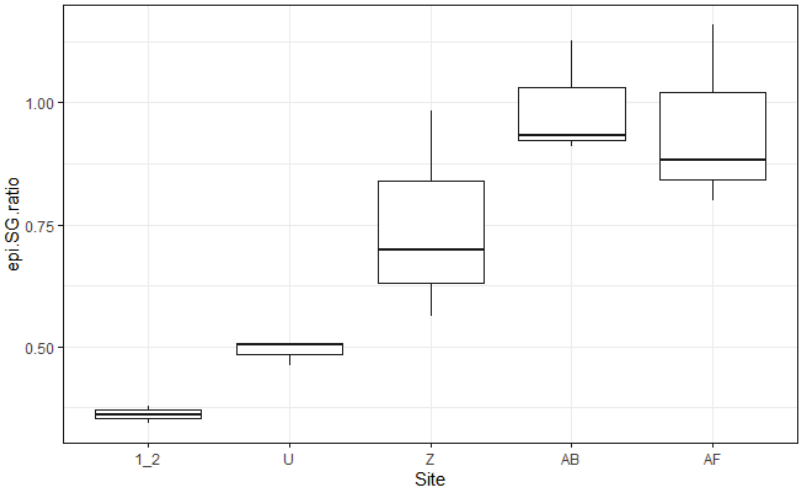

1_2 and U sites have significantly smaller ratios of epiphyte to Seagrass than AF and AB.

Observations Suggesting Direct Erosional Impacts

- Apparent loss of SG coverage near Moda from NAIP & UAV imagery
- Thal almost disappeared from Site 1_2 immediate area
- Some bare areas towards Moda have firm sediment – lack organic mat?
- Deep “guts” between SG mounds, oriented parallel to shore
- Shell hash accumulated in bottom of some guts → strong currents
- Site U: Possibly ship wake damage
  - Large patch of exposed Syr rhizomes
  - Exposed edge of SG with Thal rhizomes
- Scouring around Site Markers
  - Near Moda: from direction of Moda
  - Farther from Moda: More from SSE (Ship Channel)
- Severe Prop scarring at AF (& AB)
- August SG biomass less than in June

Exposed *Thalassia* Rhizomes on Edge of Seagrass Patch

Prop Scarring at Site AF

UAV Imagery Credit: Hua Zhang, PhD

Other Measures of Seagrass Function: “Consumer” Surveys

Squid Pops: Bait consumption indicates higher trophic consumers

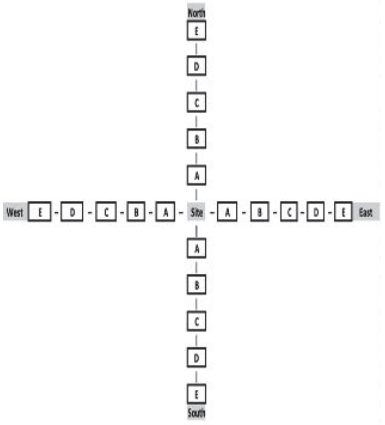

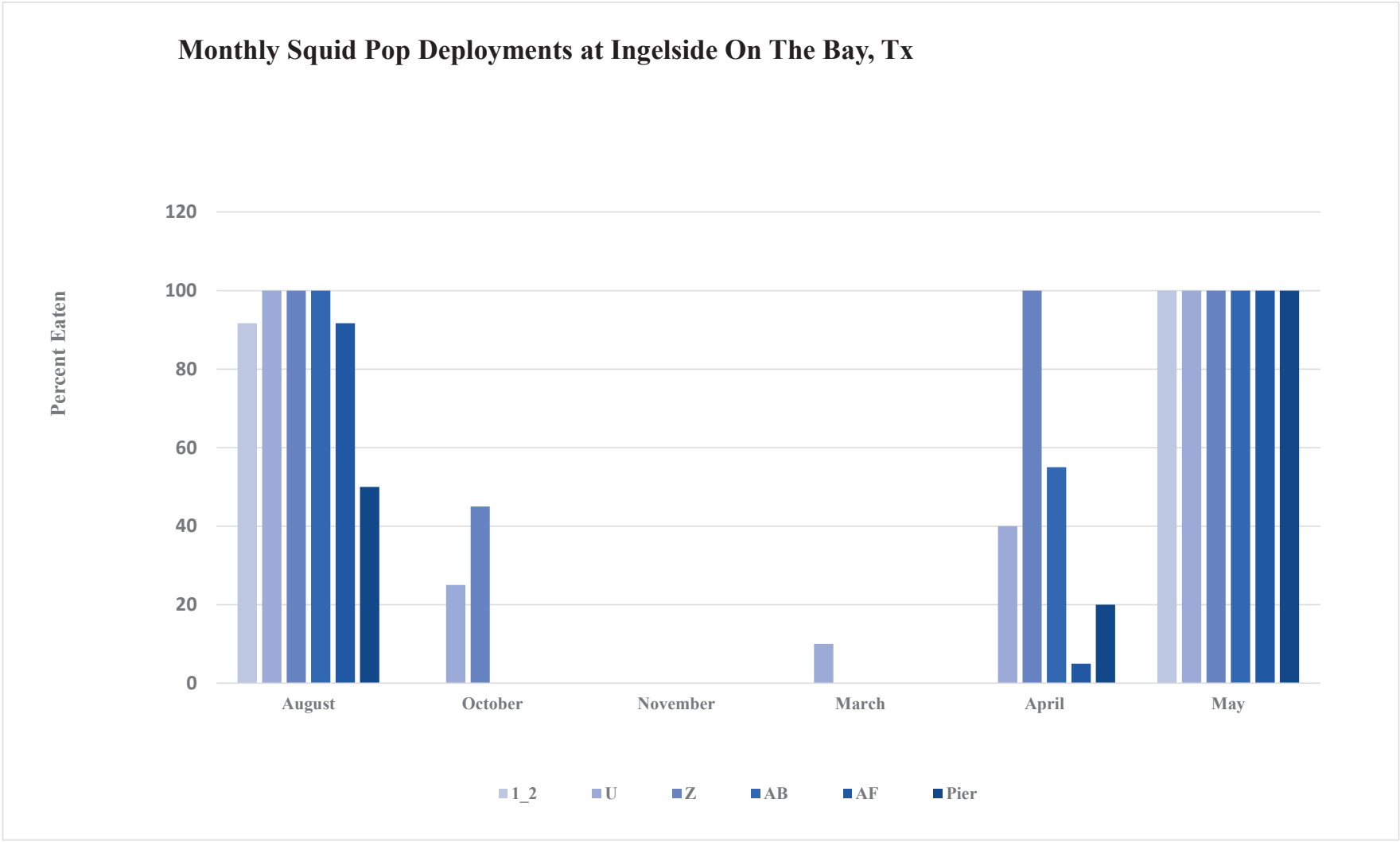
Monthly Squid Pop Deployments at Ingelside On The Bay, Tx
Percent Eaten
120
100
80
60
40
20
0
August
October
November
March
April
May
1_2
U
Z
AB
AF
Pier

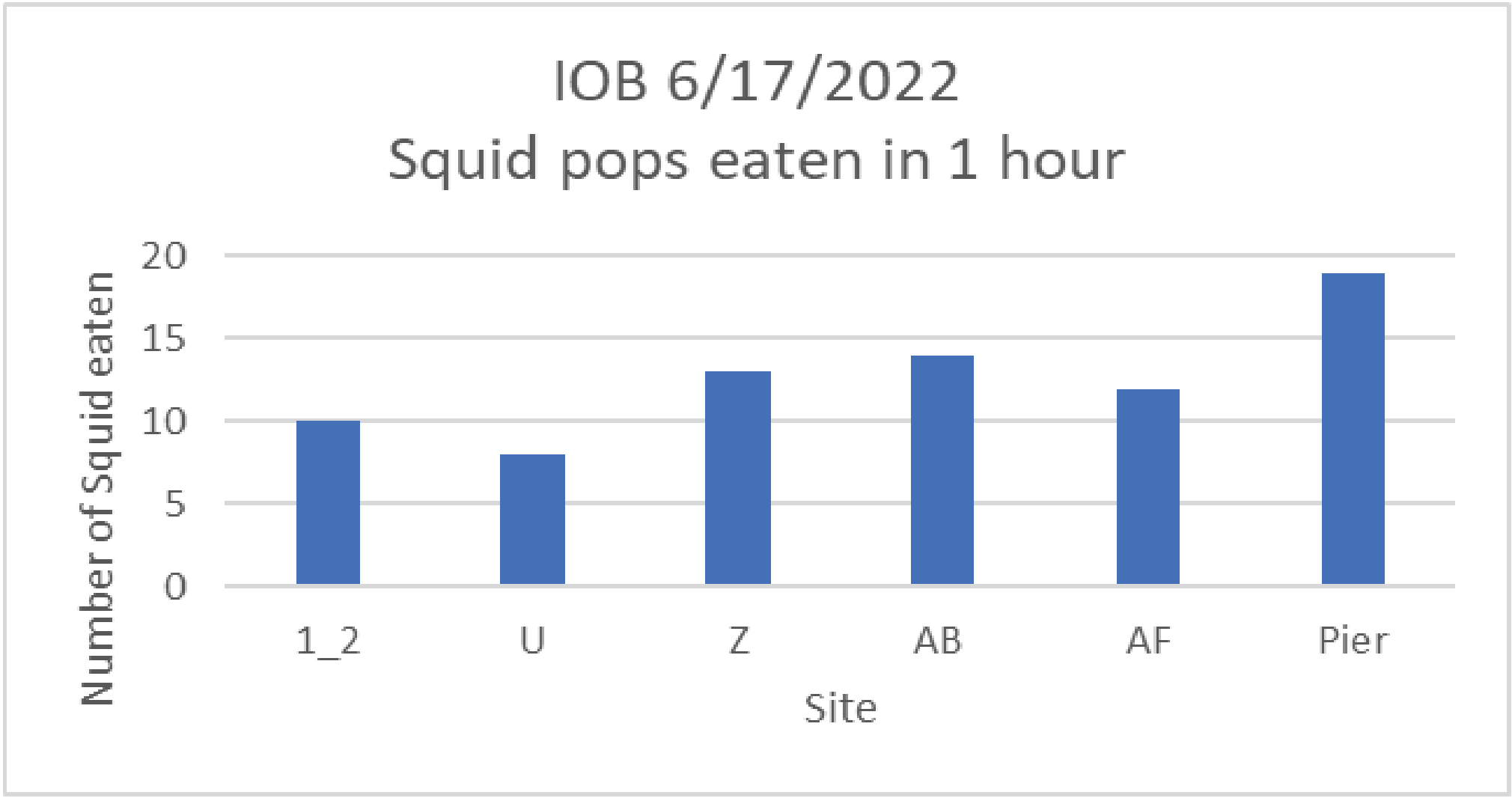
IOB 6/17/2022
Squid pops eaten in 1 hour
Number of Squid eaten
20
15
10
5
0
1_2
U
Z
AB
AF
Pier
Site

Other Factors Important For Seagrass: Salinity

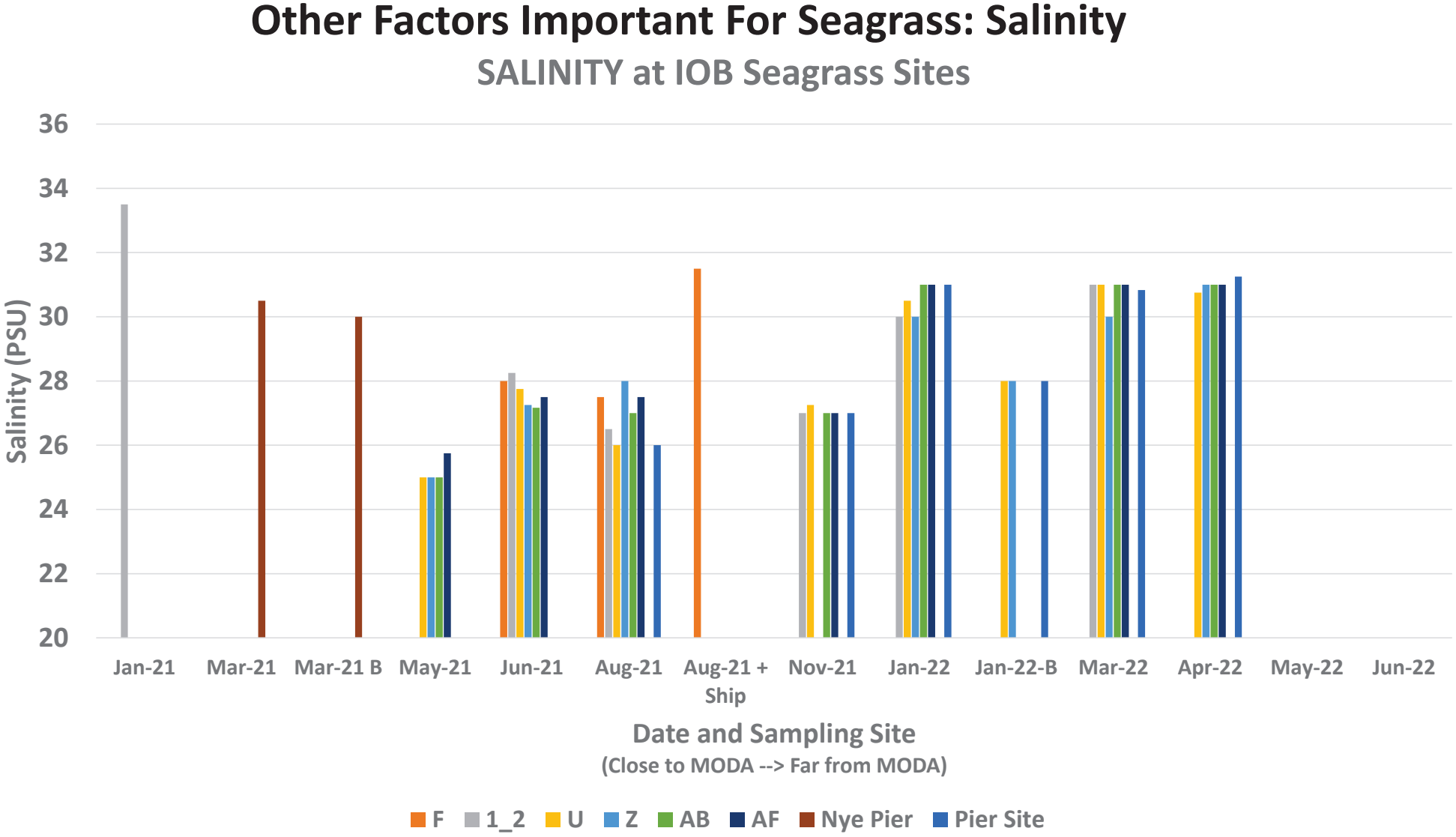

Conclusions:

- Observe gradients of SG and physical conditions away from MODA
  - Sediments, TSS and light during docking events
  - Biomass, SG species composition, morphology
- Aerial imagery suggests multi-year decline in SG coverage
- Documented sediment plumes and their spread from ship docking events; impacts on light penetration and TSS
- ***Consistent with*** **both siltation and direct erosional processes**
- ***Operational impacts*** **extend well-beyond the dock area**
- But also observe non-Moda impacts challenging SG
  - Prop scarring, ship wakes, boat landings
- More work needs to be done to characterize impacts and map SG condition

Questions ?

Acknowledgements:

THANK YOU !

- IOBCWA
- Nye family
- Hua Zhang
- Hard-working students!
- Chris and Ann Carlton
- Clark Antone and Suzi Wilder
- Jim Waits

Ship wake breaking over SG Meadows

Photo Credit: Patrick Nye

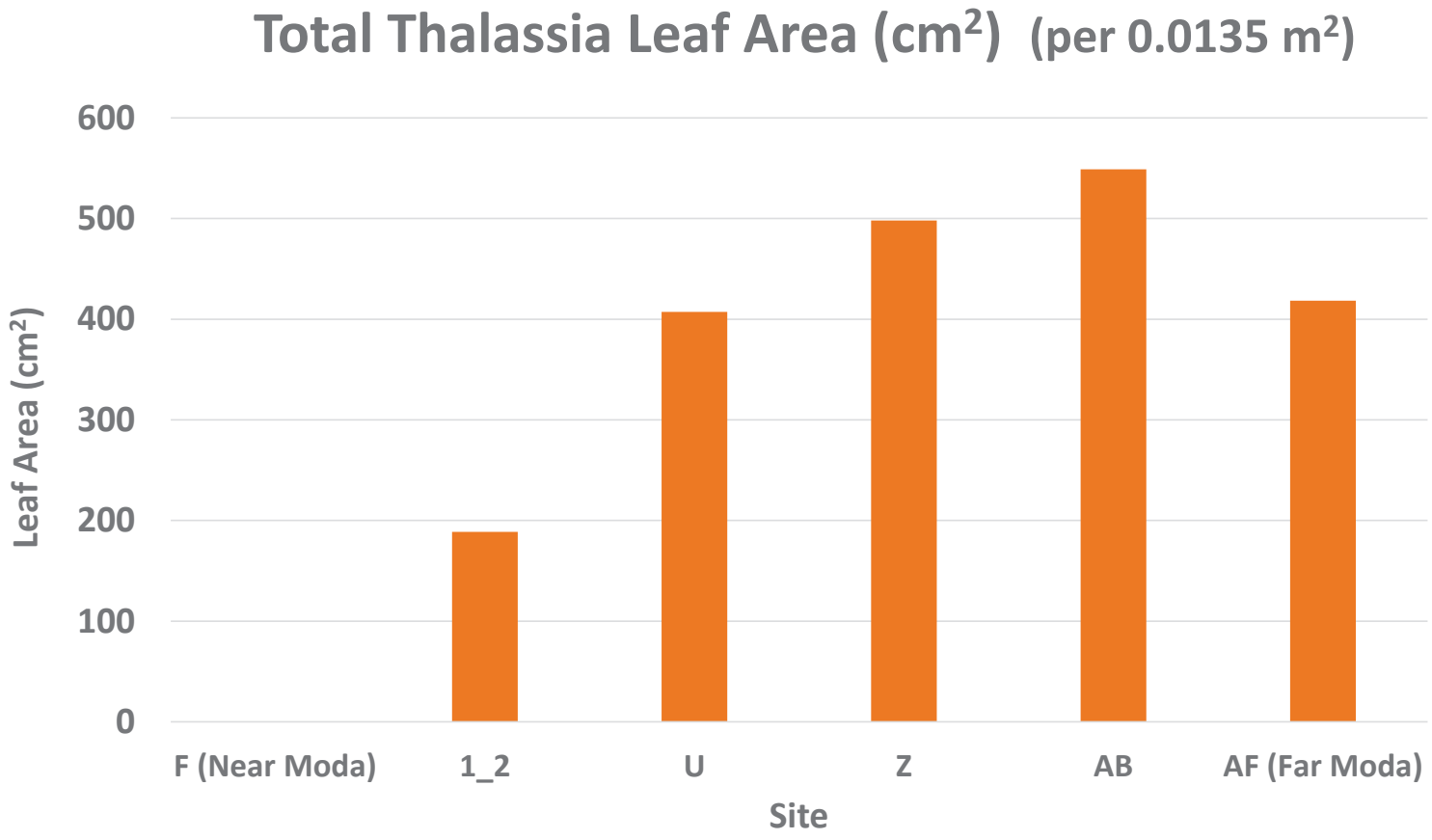

Leaf Length, Leaf Biomass, Epiphyte Biomass all exhibited similar pattern

(Must be 6-10-21 Data – NOT August 2021)

Prop Scarring at Site AB

UAV Imagery Credit: Hua Zhang, PhD

Blue = Light level

Site AF
(Far MODA)

Top Loggers

June 3
(Stormy)

June 4
(Cloudy)

June 5
(Sunny)

Site F
(Near MODA)

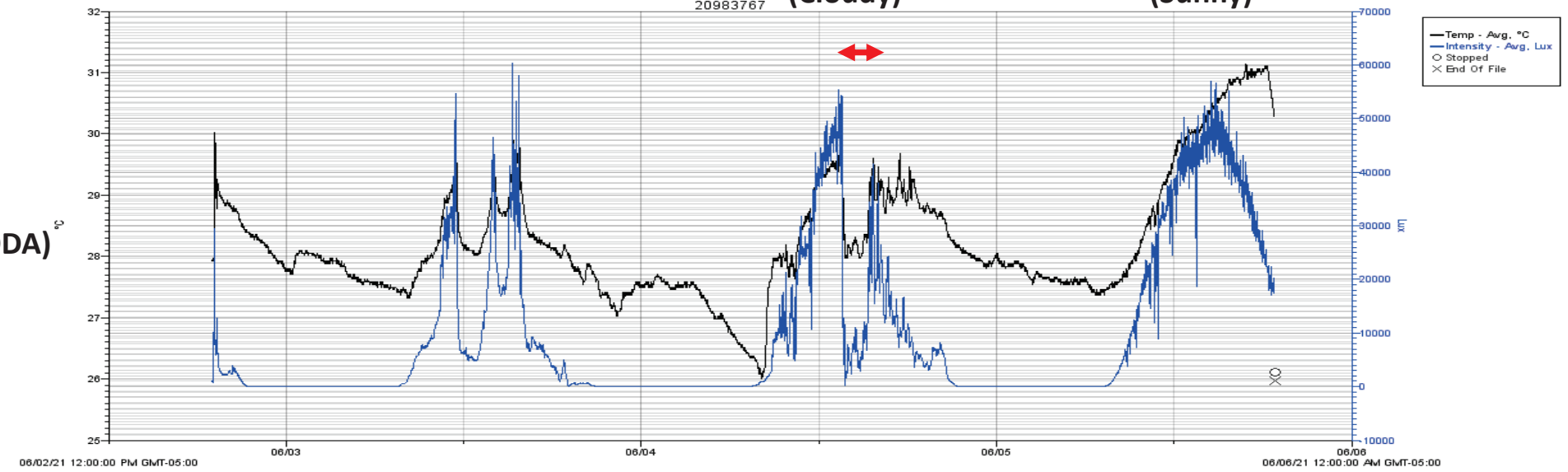

Vessel wake contributions to erosion at exposed and sheltered shorelines near a tidal shipping channel

Alexandra C. Muscalus[1] and Kevin A. Haas[2]

1. Ph.D. Candidate, Ocean Science and Engineering, Georgia Institute of Technology, amuscalus@gatech.edu
2. Associate Professor, Civil & Environmental Engineering, Georgia Institute of Technology, khaas@gatech.edu

Highlights

- The hydrodynamic power of tidal currents, wind waves, and cargo vessel wake was assessed with measurements at two types of sites: exposed and sheltered
- Hydrodynamic power was used as a proxy for relative contributions to erosion
- Low-frequency vessel wake was the main source of hydrodynamic power at both sites

Abstract

This study investigates the role of low-frequency cargo vessel wake to erosion at Bird/Long Island in the Savannah River, Georgia. The island splits the river into the Main Channel that accommodates cargo vessels traveling to the Port of Savannah, and the shallower, sheltered South Channel. Pressure and velocity data from both channels are used to characterize wind waves, tidal currents, and vessel wake. The relevance of each process to erosion is estimated by using hydrodynamic power as a proxy for erosive potential. Instantaneous water level is compared to the elevation of an eroding scarp to identify "scarp-relevant" power contributions, power occurring when the eroding scarp is at least partly submerged and susceptible to erosion. The analysis shows that scarp-relevant power in the Main Channel is dominated by cargo vessel wake (88%), with smaller contributions from tidal currents (5%) and wind waves (7%). Power in the South Channel is also dominated by cargo vessel wake (65%), followed by tidal currents (34%) and wind waves (1%). A follow-up study confirms that low-frequency cargo vessel wake, which produces waves heights up to 2.01 m in the Main Channel, propagates readily around both ends of the island and into the South Channel, resulting in wave heights up to 0.32 m.

Keywords: Coastal erosion, low-frequency vessel wake, Bernoulli wave, tidal river, shipping channel

1. Introduction

Coastal erosion is of increasing concern as economically vital coastal zones continue to grow more populated while shoreline stability is threatened by both natural processes and anthropogenic effects. One such anthropogenic effect is vessel wake, which is particularly important in commercial shipping channels where large cargo vessels navigate constricted waterways near ports, often located near urban centers. When passing through a channel, cargo vessels generate a low-frequency (LF) wake system in addition to classical wedge-shaped Kelvin wake. The LF wake stems from a water level depression surrounding the vessel in a shallow waterway, and at the shoreline it presents as a water level drawdown and return surge with a typical duration of about two minutes. The return surges can vary in form from a gentle rise in

water level to a large bore traveling alongshore at the speed of the ship; the latter is particularly dangerous. The surge is generally followed by low-frequency fluctuations that may persist long after the vessel has passed. While it may not be as obvious to the eye as higher-frequency wake systems, LF wake can carry massive amounts of energy that erode channel shorelines and threaten the safety of boaters and beachgoers.

LF wake is one of several wake components whose properties vary by sailing regimes determined by the depth Froude number, Fr

$$Fr = \frac{S}{\sqrt{gh}} \tag{1}$$

where S is the ship speed, g is gravitational acceleration, and h is water depth. In the subcritical regime ($Fr < 0.7$), the most visually obvious component of vessel wake is Kelvin wake, a wedge of higher-frequency transverse and lower-frequency diverging waves that may be described with linear theory (e.g. Thomson, 1887). The Kelvin wedge evolves, and nonlinear features become more significant as Fr increases into the transcritical ($0.7 < Fr < 1$) and critical ($Fr = 1$) regimes. For instance, linear theory dictates that as Fr approaches 1, the wedge of Kelvin wake widens into the entire half-plane behind the vessel, and the transverse and diverging waves form nearly straight waves wave moving at the speed of the vessel with a crest perpendicular to sailing line. However, as reviewed by Soomere (2007), wake features in this regime are more thoroughly characterized with nonlinear equations such as the Boussinesq equation, the nonlinear Schrödinger equation, the Korteweg–de Vries (KdV), and the Kadomtsev–Petviashvili equations. Nonlinear features include envelope wave packets within and bordering the Kelvin wedge (e.g. Brown et al., 1989 and Munk et al., 1987), narrow v-shaped turbulent wake left behind by the vessel (e.g. Munk et al., 1987 and Durkee et al., 2000), and long-crested solitary waves resembling KdV solitons (e.g. Wu, 1987). These "precursor solitons" radiate ahead of the vessel with properties dependent on Fr and wave interactions (e.g. Soomere 2006, Torsvik et al. 2006, Shi et al. 2018). For example, initially curved soliton crests in a channel may be straightened in the critical sailing regime ($Fr = 1$) when a nonlinear curved wave forms at the bow of the vessel and interacts with Mach reflections of the channel side walls (Katsis and Akylas, 1987). At the low end of the supercritical regime ($1.0 < Fr < 1.2$), the solitons begin to break (e.g. Lee et al. 1989) and may form a flat shelf of water or a bore traveling ahead of the vessel (e.g. Gourlay, 2001), but solitons no longer exist at $Fr > 1.2$. Kelvin wake is also changed in the supercritical regime; the Kelvin wedge is narrowed, the curvature of the diverging waves is reduced, energy is concentrated in the leading diverging waves, and the transverse waves no longer exist.

Low-frequency (LF) Bernoulli wake results from a water surface depression surrounding the vessel and is not limited to a particular sailing regime. The depression magnitude decays with distance away from the vessel and is negligible in the deep open water environment, but it becomes substantial when large vessels navigate shallow open water environments or narrow channels due to flow constrictions. To an observer on a channel margin, LF wake manifests as a gradual "drawdown" of the water level as the vessel passes offshore, followed by a return "surge" after the vessel has passed that often exceeds the mean water level; this drawdown and surge is herein called the "Bernoulli wave."

The magnitude of the return current and the depression have been related to vessel and channel characteristics in physical experiments (e.g. Johnson 1958, El-Kiki et al., 2007 and Macfarlane and Graham-Parker, 2019) and can be computed with models (e.g. Hochstein and

Adams, 1986, 1989; Maynord, 1996, 2007; Sorensen, 1997) utilizing the Schijf equations (Schijf 1949), which are derived from volume conservation and Bernoulli principles. While these Schijf-based depression models work well for predicting the Bernoulli depression near the vessel, they do not account for shoaling and refraction behaviors. To capture such effects, more advanced fully 3D (e.g. Shepsis et al., 2001; Fenical et al., 2002; MacDonald, 2003; Gharbi et al., 2010; Lee et al., 2005) and Boussinesq (e.g. Shi et al., 2018; Stockstill and Berger, 1994) models are required. Although questions remain about the characteristics of the Bernoulli wave in shallow water, models reliably show that the depression magnitude generally increases with vessel speed and "blockage ratio," the cross-sectional area of the vessel divided by that of the channel.

The impacts of commercial vessels in the nearshore environment are increasingly of interest as growing vessel sizes, faster vessel speeds, and increasing maritime trade augment the cumulative effects of vessel ship wake. While wake research has largely focused on offshore vessel efficiency, the coastal effects of wake rose to importance when high-speed ferries introduced in the 1980s were linked to sediment mobilization (e.g. Velegrakis et al., 2006), an increase in hydrodynamic energy, (e.g. Kelpsaite et al., 2009), enhanced runup (Didenkulova et al., 2009), coastal erosion (e.g. Kirkegaard et al., 1998; Parnell et al., 2007), and far-field water level fluctuations observed kilometers away from the sailing line (Parnell et al., 2008). This body of research is summarized and linked to resulting wake management strategies in New Zealand and Denmark by Parnell and Kofoed-Hanson (2001).

The LF wake of cargo vessels has also been linked to channel erosion, but the significance of its role varies by location. For example, ship traffic was determined to be a major source of erosion in the Sabine-Neches Waterway, Texas (Herbich and Schiller, 1984); Wootton Creek, United Kingdom (Garel et al. 2008); and Venice Lagoon, Italy (Scarpa et al., 2019). The detailed wake measurements (Zaggia et al. 2017) in the Venice lagoon reported wake-induced velocities up to 2 m/s, Bernoulli wave heights of 2.5 m, and suspended sediment concentrations (SSC) of at least thirty times background levels, the maximum measurements capabilities of the SSC sensors (Rapaglia et al. 2011). In contrast, LF wake was not significant to the erosion at Cockspur Island in the Savannah River, Georgia (Houser 2010, 2011), where shoreline changes were instead attributed to wind waves and pilot boat generated wake, perhaps owing to speed restrictions for large vessels at the site.

The present study investigates the significance of LF vessel wake, with respect to tidal currents and wind waves, to the long-term erosion documented by Alexander and Calabria (2019) along a segment of the Savannah River without vessel speed restrictions. Four weeks of velocity and pressure measurements were collected in October 2017 on the margins on the main shipping channel and a sheltered secondary channel. Data signals are divided into tidal, mid-band, and wind-wave signals using band-pass filters. Events in the mid-band signal, containing LF wake frequencies, are compared to vessel traffic to identify the relationship between vessel passages and mid-band hydrodynamic signals. For each of the three bands, the power density is computed as power per meter shoreline and referred to as "power" throughout. Because the erosion along the main shipping channel occurs on a scarp at the top of the beach, "scarp-relevant" power is distinguished as the power occurring at times when water levels exceed the elevation of the base of the scarp. The eroding feature in the secondary channel is always partially or fully submerged, so all power measured is considered relevant to erosion that site. At both sites, the average power of the three bands is compared to estimate the relative erosion potential of the associated processes. Upon identifying significant mid-band power in the

sheltered secondary channel, a set of alongshore pressure measurements were collected to confirm the propagation of LF wake into the secondary channel.

2. Site Information

2.1. *Site Characteristics*

The present study uses four-week field measurements of pressure and velocities to examine the significance of LF wake to erosion at two shallow-water sites near Bird/Long Island, an undeveloped dredge-spoil island located between the Main and South channels of the Savannah River, as shown in **Figure 1**. Located 10 km from the inlet of the river, the island is in a tidally dominant environment with a tidal range of up to 2.8 m. Tidal currents reach 2 m/s in the center of the Main Channel and about 1 m/s in the South Channel, and due to its upriver position, the island is sheltered from large wind waves. Field site "M" is located in the Main Channel, on a 1/30 sloped shelf connecting Bird/Long Island to the shipping channel, as shown by the channel cross-section in **Figure 2**. The site is directly exposed to cargo vessel wake as the Main Channel contains a shipping channel 300 m offshore that was about 150 m wide and 16 m deep with respect to mean sea level (MSL) at the time of data collection and accommodates about 2,000 vessel calls annually (Georgia Ports Authority, 2021b). The second field site, Site S is located southwest of Bird/Long Island in the South Channel of the Savannah River. As demonstrated by the cross-section in **Figure 2**, the South Channel is relatively shallow, so it is mostly used by recreational and fishing vessels and sheltered by the island from direct exposure to cargo vessel wake.

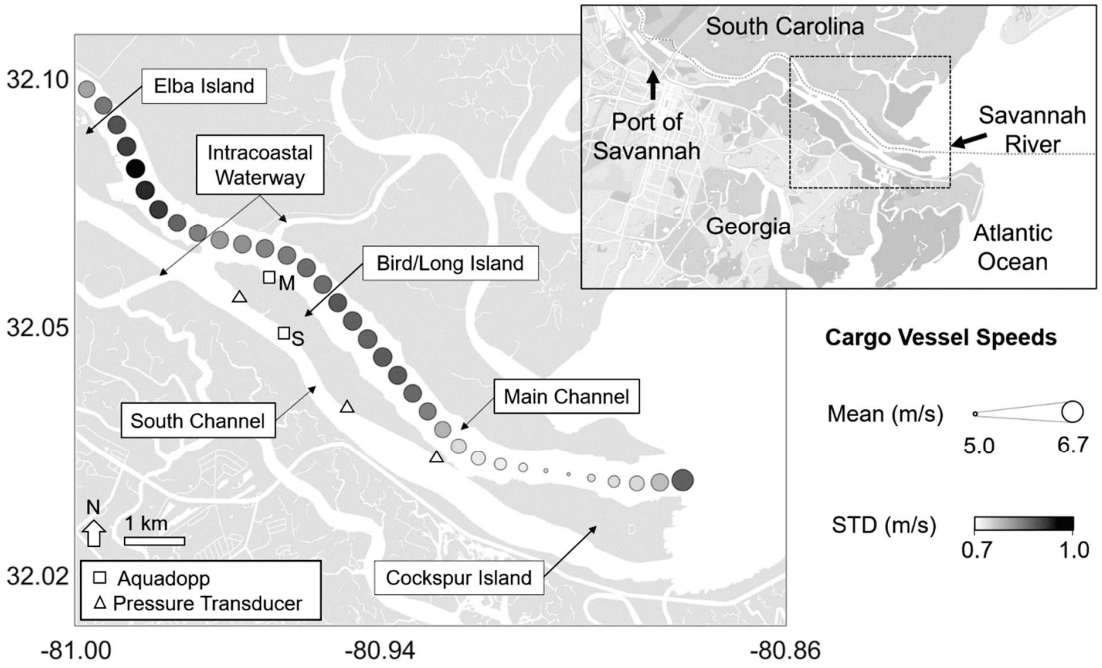

Figure 1: Aquadopp (squares) and pressure sensor (triangles) locations near Bird/Long Island in the Savannah River, GA. Mean cargo vessel speeds, averaged over a representative month of passages, are indicated with circle size. The standard deviation of speed is indicated with circle shading.

The Main Channel shoreline of Bird/Long Island varies between sandy beaches and muddy banks fronting upland trees and high marsh, while the South Channel shore consists mostly of muddy slopes and marsh. Both shores are threatened by significant erosion, which is of concern because the island serves as a wetland mitigation bank for the Georgia Department of Transportation and houses an archeological site with a Civil War artillery battery. At Site M, erosion is occurring on the scarp between the beach and tree line, but at Site S, erosion occurs over the full extent of a steep muddy slope in front of the marsh.

As documented by Alexander and Calabria (2019), the annual average erosion rates based on the 1933 to 2017 shoreline change are 1.39 m/year in the Main Channel and 0.35 m/year in the South Channel. Though not the focus of the present work due to the nonoccurrence during the measurements, extreme storms do cause rapid erosion at Bird/Long Island. For example, the annual average erosion rate based on the shoreline change from 2016 to 2017, which includes Hurricane Matthew, are 3.74 m/year in the Main Channel and 0.90 m/year in the South Channel; the authors noted that erosion rates remained elevated for at least the one year after the hurricane, the temporal extent of their measurements. However, these types of events are rare; only four hurricanes have affected Georgia in the past 50 years (NOAA, 2022). The present work does not investigate the episodic erosion driven by extreme conditions but instead focuses on identifying the source of the steady erosion at Bird/Long Island.

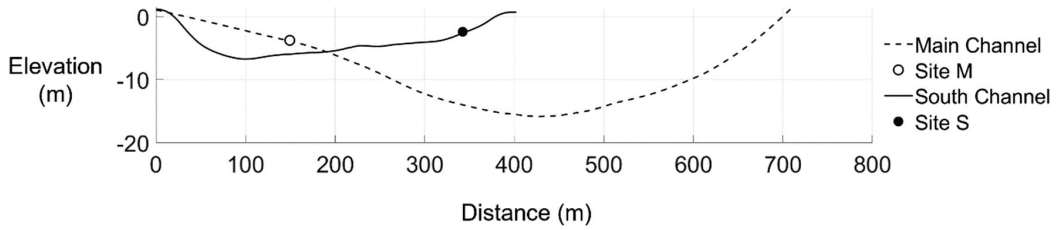

Figure 2: Representation of the cross-sections in the Main Channel (dashed line) and South Channel (solid line) at Site M (open circle) and Site S (solid circle). Both transects begin at the southwestern shore of the channel with distance increasing to the northeast.

2.2. Vessel Traffic

Information about vessel traffic in the vicinity of the site is obtained from Automatic Information System (AIS) data, which is broadcast from navigation safety devices on large vessels at regular intervals and includes vessel characteristics, position, absolute speed, and status information. AIS data broadcast during October 2017, coinciding with the deployment period, was obtained from three different sources: a publicly available database (*marinecadastre.gov)*, commercial port logistics software, and from the United States Army Corps of Engineers (USACE). When comparing the quantity of data across the three sources, it was observed that no one source was comprehensive; each was missing some vessel passages included in at least one of the other data sets. The USACE AIS data had average temporal resolution of 20 seconds for all vessel types and 10 seconds for cargo vessels while the resolution of the other sources was about 3 minutes. Therefore, the USACE data was used preferentially, and missing vessel passages were filled in from the other sources as necessary.

The vessel types and lengths from the October 2017 AIS data (**Figure 3)** indicate that vessel traffic along the island is predominantly post-Panamax cargo vessels transiting at subcritical depth Froude numbers to and from the Port of Savannah. It is of note that although pilot boats

were the dominant source of vessel-induced erosion at Cockspur Island (Houser, 2010), their typical route does not extend upriver to Bird/Long Island, and their passages at this site are much less frequent than their passages along Cockspur Island.

The absolute speeds reported in the AIS data are discontinuous owing to the coarse time resolution of the speed data and rounding to the nearest knot in the reported values. Therefore, the absolute speed was instead calculated as the time rate-of-change of interpolated position data that was low-pass filtered to remove small-amplitude, high-frequency noise. The calculated speeds were compared to the reported speeds as a means of quality control.

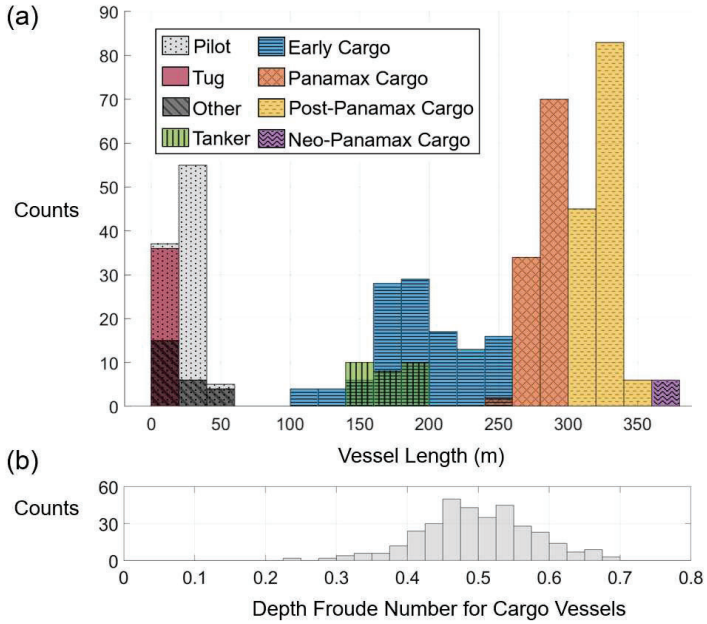

Figure 3: Vessel traffic in the Main Channel along Bird/Long Island for a representative month of AIS data characterized with **(a)** overlayed histograms of vessel lengths by type and **(b)** the distribution of depth Froude numbers for Early, Panamax, Post-Panamax, and Neo-Panamax cargo vessels combined traveling offshore of Site M.

The resulting absolute speeds were characterized for 343 passages of large vessels, vessels more than 100 m in length. **Figure 1** shows the mean and standard deviation of the absolute speeds for large vessel passages, both eastbound and westbound, along 14 km of the shipping channel near Bird/Long Island. As indicated by large marker sizes, the fastest mean vessel speeds for the region occur near the entrance to the Savannah River, at the eastern end of Cockspur Island where vessels transition into or out of their higher open-water speeds. The standard deviation of vessel speeds is also high at the river entrance, reflected by the dark marker shading. Only two kilometers upriver, along the western half of Cockspur Island, vessels are traveling at their slowest speeds (small markers) for the region, and speed variability between vessel passages is at its lowest (light markers). This slowdown is due to the Coast Guard station on Cockspur Island and its associated speed restrictions. **Figure 1** also shows that the highest standard deviations (dark markers) in vessel speed occur along Elba Island. This is because Elba Island houses a Liquid Natural Gas (LNG) facility and a port along the Main Channel for LNG

tanker vessels; cargo vessels pass the island more slowly when an LNG tanker is in port than when the port is empty.

Because Bird/Long Island is undeveloped, vessel speed along its length is not affected by coastal infrastructure. Compared to speeds at Cockspur and Elba Islands, both mean vessel speeds and the standard deviations of vessel speed are spatially consistent along much of the length of Bird/Long Island. **Table 1** provides basic summary statistics for the absolute speeds of eastbound and westbound vessels passing Site M and demonstrates that the speed characteristics do not differ substantially with direction.

Table 1: Absolute Speeds of Large Vessels Passing Site M

Direction	N (vessels)	Mean (m/s)	Median (m/s)	Std. (m/s)	Maximum (m/s)
Eastbound	155	6.20	6.25	0.81	8.31
Westbound	188	6.08	6.13	0.86	8.39
Combined	343	6.14	6.16	0.84	8.39

Vessel sailing regimes and corresponding wake characteristics are dictated by Fr, which depends on the speed of the vessel relative to the medium on which it sails. Since the Savannah River is tidally-dominant in the area of interest, large vessel speeds were evaluated relative to tidal currents in the shipping channel using model output from the USA Tidal Current Constituent Database (Defne et al. 2011, 2012). The resulting relative speeds of large vessels as they passed Site M reach 8.8 m/s, with both a mean and median of 6.1 m/s and no substantial differences between eastbound and westbound vessels. Relative vessel speeds and tidally-varying channel depths were used to compute Fr, shown in **Figure 3b**, which ranges from 0.23 to 0.69, fully within the subcritical regime.

The information just provided describes vessel traffic at the time of the field measurements in 2017, but it is now outdated due to rapid growth of maritime trade in the region. For example, the Port of Savannah experiences approximately 7% annual growth in container trade (Georgia Ports Authority, 2021b), and the ongoing harbor expansion project allows for the accommodation of increasingly large vessels. At the time of the data collection in 2017, the largest vessel to have called on the Port of Savannah was 366 m in length and 48 m in width, but at the time of writing, the port has accommodated vessels up to 396 m in length and 54 m in width. It is also of note that South Carolina has plans to construct a port on the northern shore of the Savannah River near where it intersects the Intracoastal Waterway, which is directly north of Site M. It is therefore important to identify the role of vessel wake in the erosion on Bird/Long Island, which the present work accomplishes by analyzing the power of tidal currents, wind waves, and vessel wake at both sites M and S.

3. Data Collection and Processing

3.1. Aquadopp Data Collection

Hydrodynamic data was collected simultaneously at Sites M and S with bottom-mounted, upwards-facing Nortek Aquadopp Current Profilers ("Aquadopps") deployed from October 6th, 2017 to November 3rd, 2017. The Aquadopps collected mean velocity profile data with 0.25 m vertical bins and pressure data at 10-minute intervals using 1-minute averaging durations. In addition, pressure and depth-averaged velocities were recorded at 1 Hertz (Hz) in 1024-point

bursts with intervals of 20 minutes. This corresponds to a burst duration of 17 minutes and 4 seconds, so there are 2 minutes and 56 seconds between each burst that are not measured. This deployment scheme was selected to capture the full deployment period within internal battery and storage constraints.

The Aquadopps were secured to cross-shaped aluminum channel frames with metal feet at each of the four ends to dig into bed sediment and included lead bars for additional weight. An anchor chain was attached to each frame at one end and a large lead anchor at the other, to which a marker buoy was connected. The buoy and anchor were distanced from the frame to avoid interference of the buoy line with the acoustic signal of the Aquadopp. In total, the frames weighed 100 and 60 pounds at Sites M and S, respectively, and remained stationary for the full deployment.

The Aquadopp at Site M was deployed at a mean depth of 3.52 m, with tidally-varying depths ranging between 2.03 m and 4.97 m. The Aquadopp at Site S was deployed about 1 m shallower, with a mean depth of 2.45 m, and tidally-varying depths from 0.79 m to 3.93 m.

Premature battery failure at the Site M Aquadopp resulted in a sharp drop in voltage on the evening of October 27th, after which the data was of unusably low quality. The duration of usable data is therefore 21.28 days at Site M and 27.87 days at Site S.

3.2. Aquadopp Data Processing

The Aquadopp burst data was quality-controlled by discarding data within 0.20 m of the surface and data for which the beam amplitudes were less than 50 counts, indicating weak return of the acoustic signal. Bursts and profiles collected after the sharp drop in battery voltage at Site M were also discarded. Band-pass filters were applied to the pressure and velocity data to distinguish measurements of several hydrodynamic processes. Tidal fluctuations were obtained using a low-pass filter with a cutoff frequency of $(3\ \text{hours})^{-1}$, while wind waves were extracted with a high-pass filter with a cutoff frequency corresponding to 1/10 Hz; Kelvin wake is also captured in the wind-wave band. The signals between the cutoff frequencies of $(3\ \text{hours})^{-1}$ and 1/10 Hz are treated as "mid-band" signals and include LF vessel wake.

4. Results

Hydrodynamic power is used an estimative proxy for the erosive capacity of the processes because direct observations of sediment transport were not measured. This method does not take into account the interaction of the processes with the shoreline nor the frictional losses as the energy travels from the measurement location to the shoreline. However, it is assumed that the overall trends in relative power contributions of various hydrodynamic processes at the measurement location, just offshore of the eroding shoreline, are similar to the trends at the shoreline. Ultimately, the identification of which processes are relevant to erosion is determined from only the relative contributions between the processes.

The Aquadopp measurements were used to directly compute the power, P, associated with each process at the two sites. Hydrodynamic processes primarily induce erosion when the water level is at or exceeds the elevation of the eroding feature. This is important at Site M given the large tidal range and the localization of erosion at Site M to the scarp at the back of the beach. The scarp has a base elevation z_s of 1.2 m with respect to Mean Water Level (MWL). This elevation is used to designate hydrodynamic power as "scarp-relevant" if it occurs when the water level exceeds z_s and is therefore sufficiently high to contact the scarp and contribute to erosion. In contrast, power measured when the water level is below and therefore not contacting

the scarp is considered irrelevant to the scarp erosion. The "total power" at Site M reports all power measured at the instrument, regardless of whether or not it is relevant to the scarp. Since the eroding feature at Site S is always partially or fully submerged and thus continuously exposed to hydrodynamic power, all power measured is considered relevant to erosion at the site.

For each process, several quantities of power are computed from the power time series and are presented in a table to support comparison between the processes. First, the "peak power" is taken as the maximum instantaneous power in the time series, and it provides insight into the strength of the most impactful occurrence of the process. The "average daily peak power" is computed by first finding the maximum instantaneous power on each day of the deployment and then taking the average across those daily values, and it reflects the power of the most energetic occurrence of a process on a typical day. The "average (avg.) power" is the mean of the power time series and is essential for comparing the power contributions of processes with different cumulative time series durations. However, the time-averaging for processes with very short-lived and/or episodic periods of high energy results in low average power values that do not fully reflect the significance of these events. For Site M, the total power time series is used to compute the "total" values for the four quantities described above. Likewise, the scarp-relevant power time series, with zeros inserted during times when the water level is below z_s, is used to compute the "scarp-relevant" values.

4.1. Tidal Frequency Band

The characteristics of tidal currents, captured in the frequency band with a low-pass cutoff corresponding to 3 hours, differ substantially between the two sites. In the Main Channel, flood currents at Site M persisted for an average of 5.7 hours and reached a peak at 0.76 m/s, while ebb currents persisted for an average of 6.7 hours and peaked at 0.57 m/s. In the South Channel, the Site S flood and ebb conditions were more similar in duration, lasting on average 6.3 and 6.1 hours, respectively. The difference in peak velocities at Site S were also similar; peak flood velocity was 0.58 m/s, and peak ebb velocity was 0.51 m/s. Overall, Site M had stronger tidal currents than Site S, and it varied between strongly flood-dominant and strongly ebb-dominant throughout the spring-neap cycle. Site S was weakly ebb-dominant throughout the full spring-neap cycle.

The power of tidal currents, P_{tc}, is calculated from the profiling data. Velocities are depth-averaged and low-pass filtered with a (3 hours)$^{-1}$ cutoff frequency to eliminate effects of wind waves and ship wake, isolating the tidal current velocity v_{tc}. Pressure from the profiling data are also low-pass filtered with the same (3 hours)$^{-1}$ cutoff frequency to isolate only tidal contributions to depth, h_t. P_{tc} (kW/m) is then calculated as

$$P_{tc} = \left(\frac{1}{2}\right)\rho|v_{tc}^3|h_t \times 10^{-3} \quad (3)$$

where ρ is the water density at the field site, $1020\ kg/m^3$; v_{tc} is the tidal current velocity; and h_t is the depth accounting only for tidal stage. The time series of total P_{tc} and scarp-relevant P_{tc} is shown alongside the tidal stage time series in **Figure 4** and clearly fluctuates with both the semi-diurnal and spring-neap tidal cycles, with the most powerful conditions typically occurring on the falling tide. At Site M (**Figure 4a**), when the scarp-relevant portions of the power time series (black) are compared to the tidal water level time series and overlaid scarp elevation z_s, it is clear that tidal currents affect the scarp only for very high tidal stages, primarily spring high tide. In contrast, the tidal current power at Site S (**Figure 4b**) affects the eroding sediment

continuously. Since currents are weaker at Site S, the tidal current power is more sensitive to the tidally-varying water depth. Therefore, peak tidal current power often occurs nearer to high tide at Site S than it does at Site M, where the temporal velocity variation plays a stronger role. The relative phasing of tidal currents and tidal stage, which varies with the spring-neap cycle at both sites, is also important to the magnitude of tidal current power and is described in the *Discussion.*

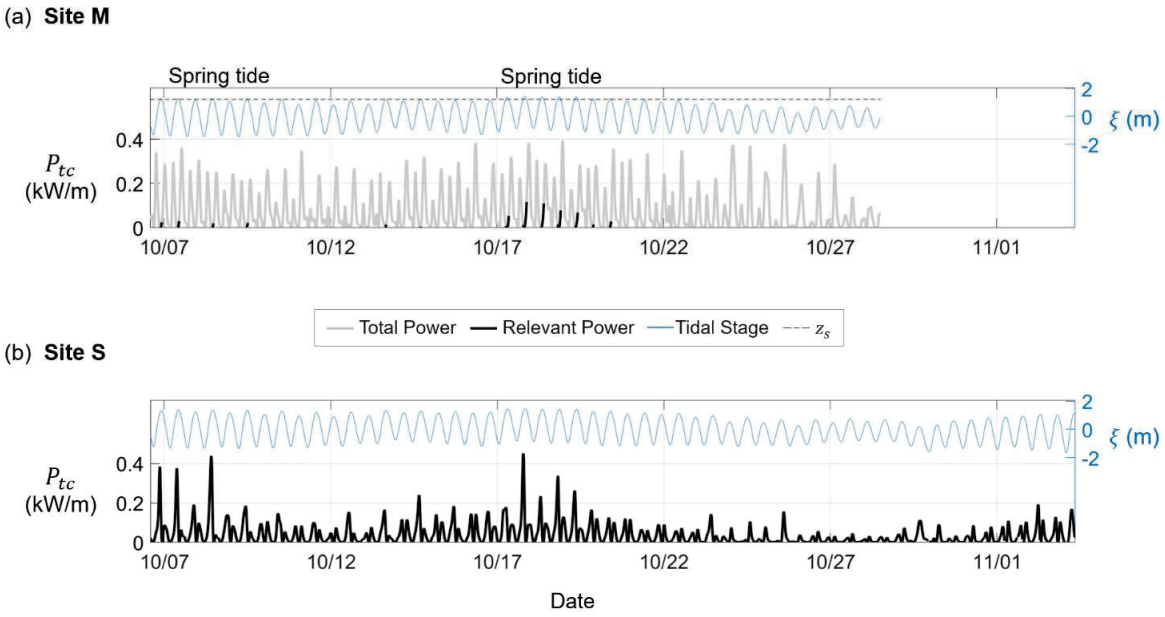

Figure 4: Time series of tidal current power (P_{tc}) and tidal stage (ξ) at (**a**) Site M and (**b**) Site S during October 2017. Power is plotted on the left axis, and tidal stage is plotted on the right axis. For Site M, the total power is shown in grey, and the scarp-relevant portion of that power is shown in black. The scarp elevation, z_s, is shown overtop the tidal stage. At Site S, all power is considered relevant to erosion.

The overall peak power (kW/m), average daily peak power (kW/m), and average power (kW/m) of tidal currents are calculated from the power time series and reported for both sites in **Table 2**.

Table 2: Tidal Current Power

Site	Peak P_{tc} (kW/m)	Avg. Daily Peak P_{tc} (kW/m)	Avg. P_{tc} (kW/m)
Site M, Total	3.94×10^{-1}	3.10×10^{-1}	7.85×10^{-2}
Site M, Scarp-relevant	1.16×10^{-1}	3.96×10^{-2}	5.88×10^{-4}
Site S	4.54×10^{-1}	1.79×10^{-1}	4.01×10^{-2}

4.2. Wind-Wave and Kelvin Wake Frequency Band

Wind waves and Kelvin wake are both captured in the wind-wave high-pass frequency band with a frequency cutoff of 1/10 Hz. Significant wave height H_{mo} is calculated from the portion of the spectrum within this frequency band for each burst of Aquadopp data and is used to

represent the total wave field within this frequency band for each burst; individual Kelvin waves are not resolved sufficiently to be analyzed in isolation. The mean and maximum H_{mo} are 0.06 m and 0.27 m, respectively, at Site M, and 0.02 m and 0.19 m at Site S. The mean energy period, T_E, is 2.78 seconds at Site M and 2.82 seconds at Site S.

The wind wave power, P_{ww}**,** is approximated by representing the wave field of each burst by a single wave with a period equal to the energy period of that burst. Group velocity C_g is computed from the wavelength k_E corresponding to that energy period through the dispersion relation, so then the power to due to wind waves (P_{ww}) is

$$P_{ww} = (\frac{1}{8}\rho g {H_{mo}}^2)(C_g) \quad (4)$$

It is noted that with a measurement Nyquist frequency of 0.5 Hz, high-frequency wind waves are not well-resolved in the measurements. The loss of higher frequencies leads to an underestimate of the power, while aliasing into lower frequencies produces an overestimate due to a possible peak shift to lower frequencies, which in turn increases C_g estimates. It cannot be determined whether the overall effect is an over- or under-estimate. However, these poorly resolved waves are expected to have small amplitudes and negligible energy in the context of this study.

The time series of total and scarp-relevant P_{ww} is given in **Figure 5**. The power is low at both sites but is an order of magnitude greater at Site M (**Figure 5a**) than at Site M (**Figure 5b**). High wind speeds elevate wind waves, and northeast winds generate larger responses due to their alignment with the channel, maximizing the local fetch. It is also apparent from the scarp elevation z_s overlaid on top of the tidal water level time series in **Figure 5a** that high tides are required for wind waves to affect the scarp at Site M.

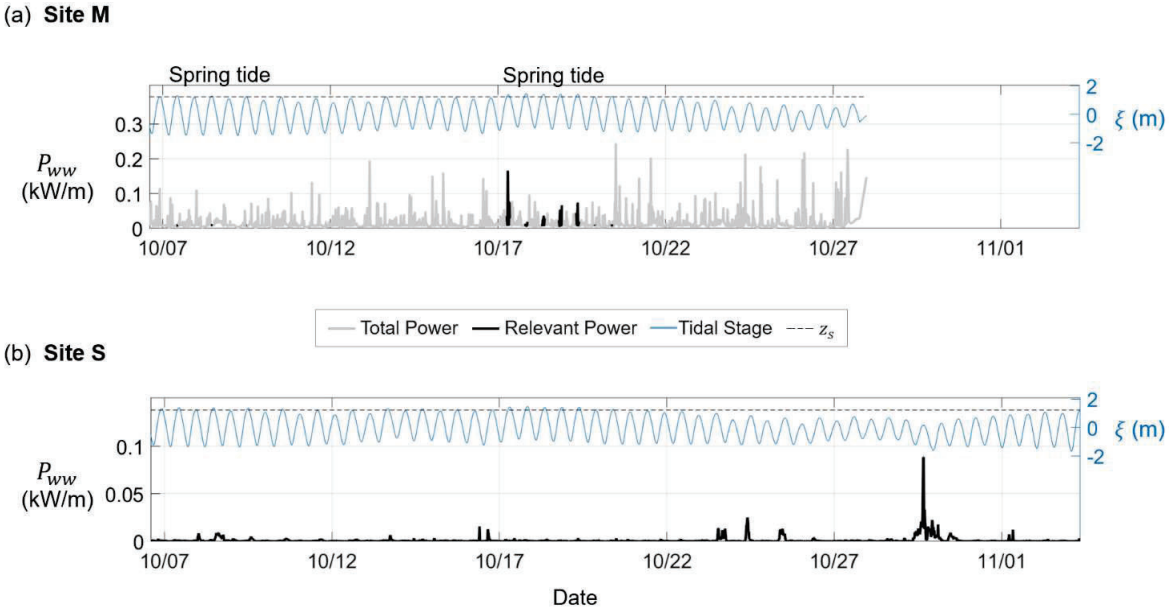

Figure 5: Time series of wind wave power (P_{ww}) and tidal stage (ξ) at (**a**) Site M and (**b**) Site S during October 2017. Power is plotted on the left axis, and tidal stage is plotted on the right axis. For Site M, the total power is shown in grey, and the scarp-relevant portion of that power is shown in black. The scarp elevation, z_s, is shown overtop the tidal stage. At Site S, all power is considered relevant to erosion.

The overall peak power (kW/m), average daily peak power (kW/m), and average power (kW/m) of wind waves are calculated from the power time series and reported for both sites in **Table 3**.

Table 3: Wind Wave Power

Site	Peak P_{tc} (kW/m)	Avg. Daily Peak P_{tc} (kW/m)	Avg. P_{tc} (kW/m)
Site M, Total	2.42 x 10^{-1}	1.37 x 10^{-1}	1.67 x 10^{-2}
Site M, Scarp-relevant	1.63 x 10^{-1}	4.31 x 10^{-2}	7.19 x 10^{-4}
Site S	8.88 x 10^{-2}	9.03 x 10^{-3}	1.24 x 10^{-3}

4.3. Mid-Band Frequency Band

"Mid-band" processes have frequencies between those of tidal currents, (3 hours)$^{-1}$, and wind waves, 1/10 Hz. This includes the frequencies of LF vessel wake and cross-channel seiching.

The power in the mid-band frequencies is evaluated with a direct nonlinear energy flux calculation. First the velocity and pressure data of a burst are detided with a one-hour polynomial curve fit. The velocity is split into tidal ($\vec{V}$) and fluctuating ($\overrightarrow{v'}$) components. Similarly, the pressure is split into a tidal component (p_t) and a mid-band fluctuating (p') component; because the mid-band pressure fluctuations are relatively low frequency and in shallow water, they are assumed to be hydrostatic. The effects of wind waves and high frequency wake components are

removed from the detided signals using a low-pass filter with a (1/10) Hz cutoff frequency. The resulting mid-band velocities and pressure are used to compute a time series of the instantaneous mid-band power magnitude per meter shoreline, P_{mb}

$$P_{mb} = \left|\vec{V} + \overrightarrow{v'}\right| \left(p' + \frac{1}{2}\rho|\vec{v}'|^2\right)\left(\frac{p_t + p'}{\rho g}\right) \quad (5)$$

where $\left(p' + \frac{1}{2}\rho|\vec{v}'|^2\right)$ is the energy due to mid-band fluctuations, $\left(\frac{p_t+p'}{\rho g}\right)$ is the instantaneous water depth, and $\left|\vec{V} + \overrightarrow{v'}\right|$ reflects the advection of the energy by both the tidal and mid-band contributions to velocity.

When determining whether power is scarp-relevant at Site M, z_s is compared against the total instantaneous water level, which includes the effects of the surge in the low-frequency wake but does not account for shoaling of that surge. Shoreward shoaling would increase the proportion of the mid-band power that impacts the scarp.

The time series of the mid-band power magnitude $|P_{mb}|$ over the full deployment period is provided in **Figure 6**, which demonstrates that very strong spikes in mid-band power occur sporadically at both Site M (**Figure 6a**) and Site S (**Figure 6b**) and need not necessarily occur at high spring tide to affect the scarp. Comparison of these mid-band spikes with AIS vessel traffic data, shown for a 72-hour example period in **Figure 6,** shows that mid-band spikes are produced in response to the cargo vessel passages, marked on the time series with filled green circles. The LF wake of the vessels can produce sufficiently large surges that reach the scarp even at non-peak tidal stages. LF wake in the Main Channel produces Bernoulli wave heights up to 2.01 m. Wake responses in the South Channel are also linked to cargo vessel passages in the Main Channel, suggesting that LF wake propagates from the Main Channel to the South Channel, where the maximum recorded wave height was 0.32 m.

All instances of significant mid-band power were associated with vessel passages based on manual inspection of the P_{tc} time series and vessel traffic records. However, because the burst data is discontinuous, it is insufficient for accurately computing the portion of mid-band power produced by known vessel passages. With LF wake signals persisting 30 minutes for a single event, no full wake system is captured by a 17-minute burst. Even Bernoulli waves alone, the first wave of the LF system, were only fully captured within individual bursts for half the cargo vessel passages.

The overall peak power (kW/m), average daily peak power (kW/m), and average power (kW/m) of the mid-band processes are calculated from the power time series and reported for both sites in **Table 4**. Because it is directly exposed to cargo vessel wake, Site M has nearly three times more mid-band power than Site S. However, only a small fraction of that power at Site M is scarp-relevant such that the scarp-relevant mid-band power at Site M is actually less than that at Site S.

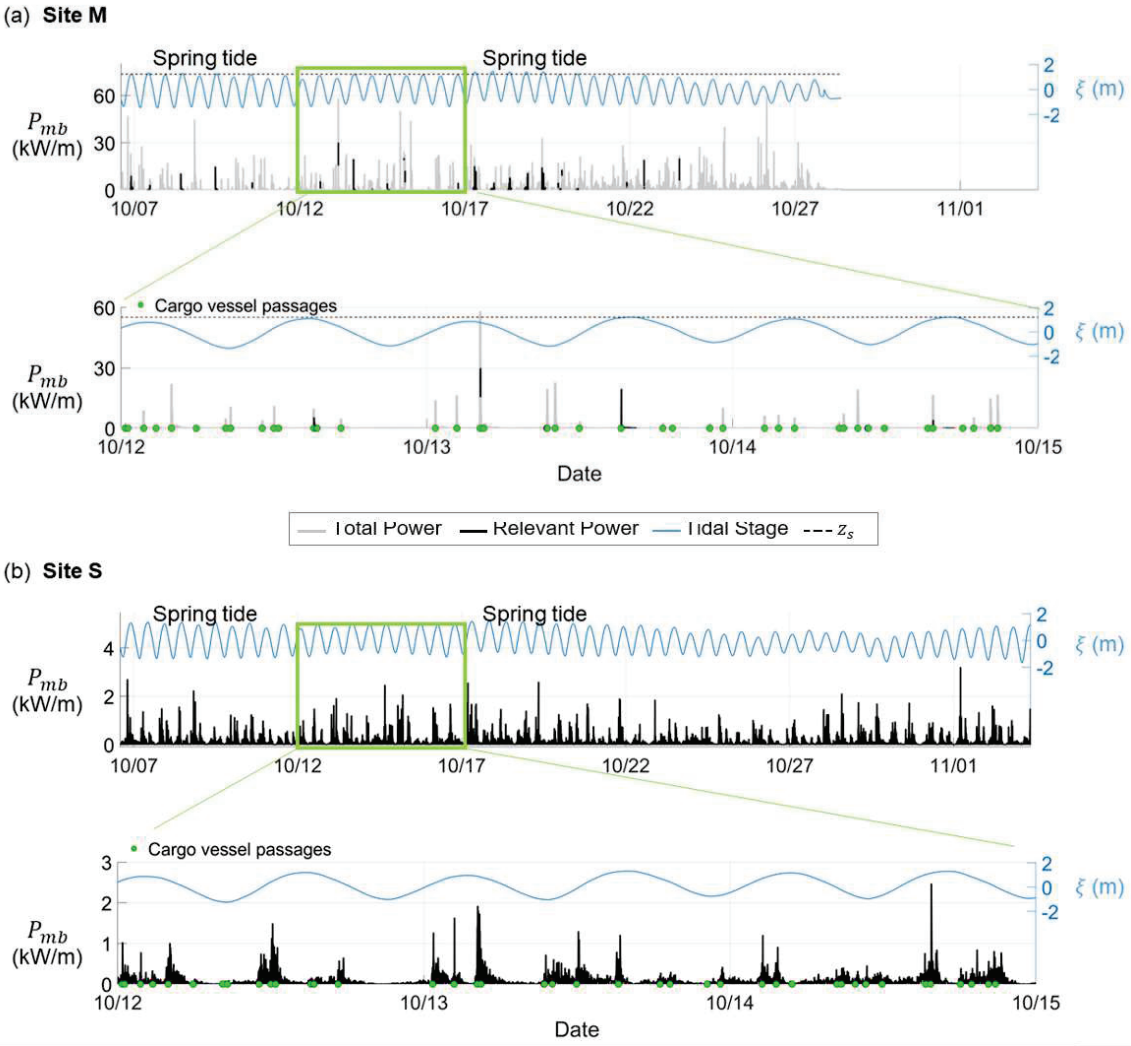

Figure 6: Time series of mid-band power (P_{mb}) and tidal stage (ξ) at (**a**) Site M and (**b**) Site S during October 2017. Power is plotted on the left axis, and tidal stage is plotted on the right axis. For Site M, the total power is shown in grey, and the scarp-relevant portion of that power is shown in black. The scarp elevation, z_s, is shown overtop the tidal stage. At Site S, all power is considered relevant to erosion. Three-day segments of each power time series are enlarged and supplemented with the times of cargo vessel passages (circles) to highlight the coincidence between vessel passages and spikes in mid-band energy at both sites.

Table 4: Mid Band Power

Site	Peak P_{tc} (kW/m)	Avg. Daily Peak P_{tc} (kW/m)	Avg. P_{tc} (kW/m)
Site M, Total	59.2	29.2	2.47×10^{-1}
Site M, Scarp-relevant	29.6	10.9	9.69×10^{-3}
Site S	3.21	1.70	7.63×10^{-2}

462 *4.4. Relative Contributions*

463 The relative average power contributions of currents, wind waves, and mid-band frequencies
464 at the two sites are shown in **Figure 7**. Mid-band frequencies are by the far the dominant source
465 of power at both sites. At Site M, mid-band processes account for about 72% of the total power
466 and 88% of the scarp-relevant power. At Site S, mid-band processes account for 65% of the
467 power. Tidal currents are the second-most important process. They constitute 23% of the total
468 power and 5% of the scarp-relevant power at Site M, but are more important at Site S, where
469 they account for 34% of the power. Wind waves and Kelvin wake make up 5% of the total power
470 and 7% of the scarp-relevant power at Site M, and only 1% of the power at Site S.

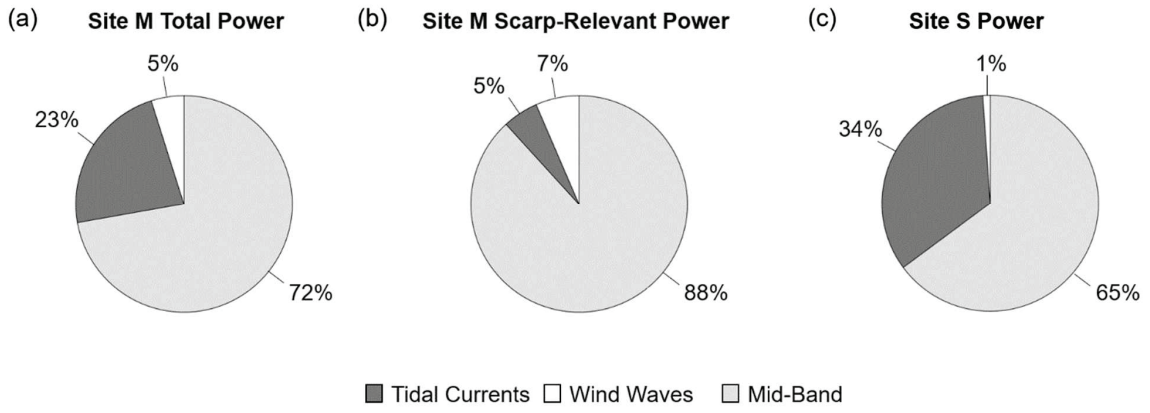

471

472 **Figure 7:** Relative contributions from tidal currents (dark grey), wind waves (white), and mid-band
473 processes (light grey) to (**a**) total power at Site M (**b**) scarp-relevant average power at Site M and (**c**)
474 power at Site S. All power at Site S is considered relevant to erosion.

475 **5. Discussion**

476 The hydrodynamic power at the instrument is used as a proxy for erosion potential. It is
477 assumed that the relative power contributions measured at the instrument are reasonably
478 representative of the contributions at the eroding shoreline itself. Processes introducing greater
479 amounts of hydrodynamic power to the shoreline are assumed responsible for greater amounts of
480 the observed erosion.

481 *5.1. The Role of Tidal Currents and Wind Waves*

482 Tidal currents contribute a significant fraction of the scarp-relevant power at Site S, but not at
483 Site M. This disparity in the contribution can be explained by the requirement that water levels
484 must exceed z_s for power to be considered scarp-relevant at Site M and by differences in the
485 phasing of tidal stage (ξ) and tidal current ($\vec{V}$, flood positive), shown in **Figure 8**. First, as shown
486 in **Figure 8a**, tidal water levels only exceed z_s at spring tide, when flood currents (positive
487 $\vec{V}$) and ebb currents (negative $\vec{V}$) both peak just before mid-tide. The currents during the highest
488 water level of the spring high tide are weak. Therefore, during the limited times when the water
489 levels reach the scarp, the tidal current power is low, as demonstrated by low P_{tc} at high ξ in
490 **Figure 8c**. The relative phasing between tidal currents and tidal stage is slightly different at neap
491 tide; flood currents (positive $\vec{V}$) peak just after mid-tide, but ebb currents (negative $\vec{V}$) still peak

before mid-tide. All tidal water levels are too low during neap tides for the currents to affect the scarp at Site M.

At Site S, tidal current impacts are not limited to a particular tidal stage, but like Site M, the relative phasing of the tidal currents and tidal stage varies throughout the spring-neap cycle. As seen in **Figure 8b**, during a spring tide, Site S flood currents peak at high tide, while the ebb currents peak near mid-tide. In contrast, during a neap tide, flood currents peak at mid tide while ebb current peak near high tide. For most tidal cycles, the peak velocities for flood and ebb occur at $\xi \geq 0$. Since tidal current power scales with the depth $\bar{h} + \xi$, where $\bar{h}$ is the mean deployment depth, the coincidence of the strong currents with higher tidal stages produces considerable tidal current power, as demonstrated by high P_{tc} at high ξ in **Figure 8**. Therefore, the peak flood currents at spring high tide are especially important to the overall tidal current power at Site S.

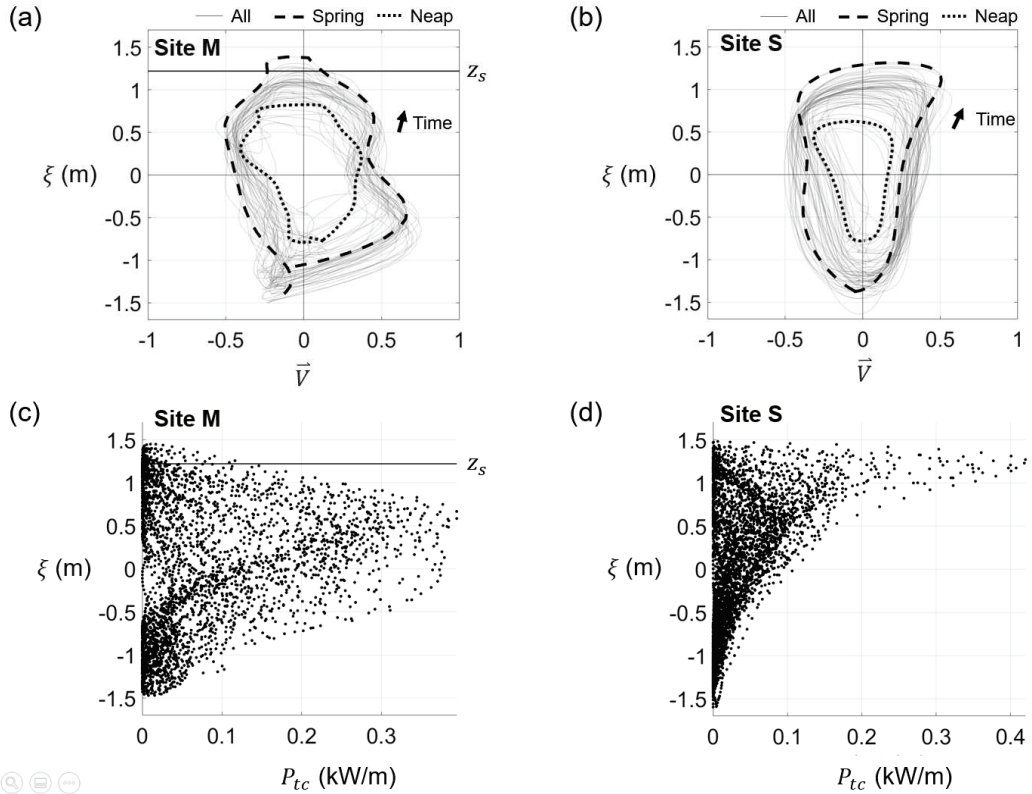

Figure 8: Stage-velocity diagrams from the profiling data for all tidal cycles measured at (**a**) Site M and (**b**) Site S, with representative spring and neap tides indicated in dashed and dotted lines, respectively. Temporal progression is counterclockwise, and $\vec{V}$ is positive in the flood direction. Tidal stage (ξ) vs. tidal current power P_{tc} for (**c**) Site M, with z_s indicating the elevation the base of the scarp, and for (**d**) Site S.

It is important to note that this analysis method overestimates the contributions of tidal currents by evaluating power over the full water column at the instrument. For wind waves and wake, it is reasonable to assume that most of the power measured at the instrument propagates to shore with the waves, but tidal current power moves with the primarily longshore flow and is not conserved in the cross-shore. Rather, tidal current power generally decreases shoreward due to both frictional losses slowing current speeds and the decrease in depth. The available velocity

514 measurements were collected at mean depths of 3.52 m and 2.45 m at Sites M and S,
515 respectively, and for consistency with the other processes, tidal current power was evaluated for
516 the depth at the instrument. The actual "effective depth" over which the current can impact
517 sediment at the eroding portion of the shore is unknown and likely dependent upon tidal stage,
518 flow velocity, and sediment characteristics. However, as a demonstration of sensitivity, if an
519 effective depth of 0.5 m is used in the computation of total P_{tc} at Site M, i.e., h_t in (3) is replaced
520 with 0.5 m, the total average P_{tc} at Site M decreases 86% from the value measured at the
521 instrument (**Table 1**). In this scenario, the relative contribution (compared to **Figure 7**) of tidal
522 currents to the total power at Site M is reduced to 4%, while wind wave contributions increase to
523 6%, and mid-band contributions increase to 90%. If currents speeds are weakened by 25% to
524 represent frictional losses while the effective depth is kept at 0.5 m, the total average P_{tc}
525 decreases by 94%. This decreases the relative contribution of tidal currents to just 2%, while
526 wind waves contributions increase to 6%, and mid-band contributions increase to 92%.
527 Therefore, in reality, tidal currents are expected to be even less significant to erosion than is
528 suggested by the results in **Figure 7**.
529 Wind waves and Kelvin waves are small at both sites. The lack of large wind waves is due to
530 the sheltered upriver location of the island, which is not exposed ocean wind waves and has an
531 extremely limited fetch for all winds except those aligning southeast or northwest with the river.
532 During the measurement period of record, there were no extreme storms, but there were several
533 events with moderate sustained winds. On October 17th, 8 m/s to 11 m/s northeast winds
534 persisted for 16 hours, producing significant wave heights up to 19 cm at Site M and 3 cm at Site
535 S. On October 25th, 7 m/s to 9 m/s northwest winds were sustained for 4 hours and produced
536 significant wave heights up to 20 cm at Site M and 8 cm at Site S. The strongest event took place
537 on October 29th, when 11 m/s to 14 m/s northwest winds were sustained for 14 hours, producing
538 significant wave heights of 19 cm at Site S; the effects were not captured at Site M due to battery
539 failure.
540 Based on the Sverdrup Munk Bretschneider (SMB) wave forecasting curve (USACE, 2008),
541 one hour sustained 22 m/s (50 mph) winds perfectly aligned with the southeast direction of
542 maximum local fetch would produce 1 m waves, assuming an average depth of 7.5 m.
543 Hurricanes could produce waves exceeding 2 m under these same worst-case-scenario
544 assumptions, but such conditions are rare. According to the NOAA Hurricane Research Division
545 (NOAA, 2022), Georgia has been affected by hurricanes four times in the past 50 years, but only
546 two of these hurricanes produced sustained winds exceeding 22 m/s (50 mph).
547 Kelvin wake frequencies overlap those of wind waves and are not easily separated from the
548 wind wave signal, but given the overall low power contribution of this frequency band, it may be
549 assumed that they do not contribute substantial power to the hydrodynamic environment.
550

551 5.2. *Low-Frequency Vessel Wake in the Main Channel*

552 The dominance of power at the mid-band frequencies at both sites motivates the investigation
553 of low-frequency vessel wake. This is accomplished by first using the AIS data to determine
554 when vessels pass Site M, and then by identifying the corresponding low-frequency wake
555 response in the mid-band data. The response has a reliable low-frequency signature, consistent
556 across all vessel passages. A time series of the water level, power magnitude, and velocity
557 fluctuations in a typical wake event observed at Site M is given in **Figure 9**, and the

characteristics are described here from the perspective of an observer on the shore of Bird/Long Island looking into the Main Channel. As a vessel approaches, water flows alongshore towards the vessel (negative v'_x) and offshore (positive v'_y) while the water level drops. This reduction in water level is the shallow-water presentation of the Bernoulli depression that surrounds the vessel. Once the vessel and its attached depression have passed offshore of the site, the drawdown transitions into the surge. The water level rises, often exceeding the mean water level, and the current reverses direction, now flowing in the direction of vessel travel (positive v'_x) and onshore (negative v'_y). It should be noted that Bernoulli wave theory does not include cross-shore velocities, so these may be a shallow-water or shelf effect. High-frequency Kelvin wake is usually superimposed on top of the surge but has a much smaller amplitude and therefore less energy than the surge itself. Continued low-frequency oscillations, termed "trailing waves" here, may persist more than 30 minutes after the vessel passes. Overall, the wake features are very consistent among events in the Site M data since it located very near the shipping channel. A lagged mid-band response to cargo vessel traffic is also evident at Site S, but its signature is not as clean or consistent as the signature at Site M.

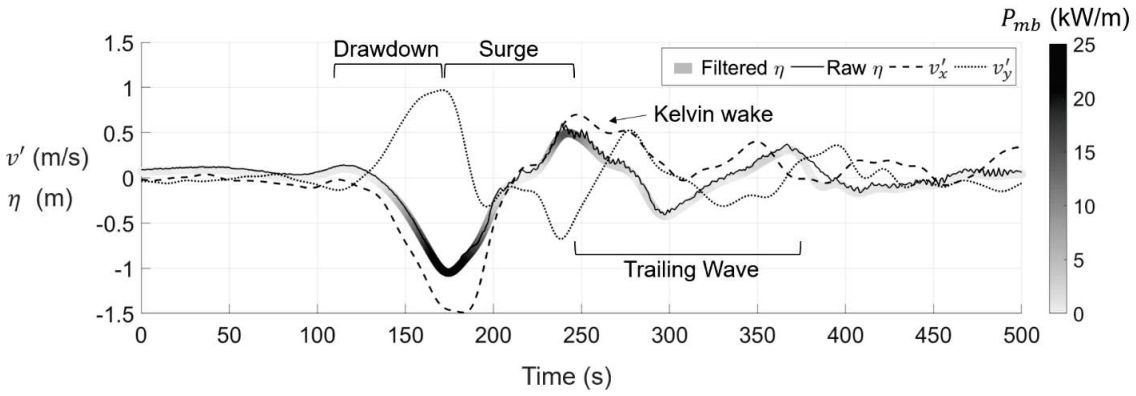

Figure 9: Water level (η) and velocity fluctuation (v') time series from an Aquadopp wave burst shaded by power P_{mb} for a sample LF wake event. Velocity fluctuations are positive longshore in the direction of vessel travel (v'_x) and offshore ($v_y{}'$). Characteristics in the low-pass filtered signal (thick line) include the drawdown, surge, and first trailing wave. High-frequency Kelvin waves appear in the raw η data (thin line) at the top of the surge.

Bernoulli waves, defined from the zero down-crossing into the drawdown to the zero down-crossing following the surge, were fully captured within individual bursts at Site M for the passages of 176 large vessels. The characteristics of these waves as measured at Site M are reflected in **Figure 10**, which gives the distribution of Bernoulli wave drawdowns and surges, velocity fluctuations in the along-shore (v'_x) and cross-shore (v'_y) directions, and Bernoulli wave energy density (E), which was computed by integrating the mid-band power time series over the duration of the Bernoulli wave. The extrema of the large events include a maximum drawdown of 1.40 m, maximum surge of 0.62 m, maximum Bernoulli wave height of 2.01 m, maximum velocity fluctuation magnitude, $|v'|$, of 2.45 m/s, and maximum E of 2.45 megajoules per meter shoreline (MJ/m). In general, the magnitude of the drawdown is greater than that of the surge. The alongshore velocities during the drawdown, flowing against the direction of ship travel, are highly variable with a mean of 0.64 m/s and standard deviation of 0.39 m/s. The

alongshore velocities aligned with the vessel direction and occurring during the surge, however, are more tightly limited to smaller values, with a mean of 0.32 m/s, and standard deviation of 0.25 m/s. Cross-shore velocities are distributed similarly in the onshore and offshore direction. The energy density of the Bernoulli wave is highly variable between wake events. Across the 176 analyzed wake events, the mean Bernoulli wave energy density is 0.41 MJ/m, the median is 0.30 MJ/m, and standard deviation is 0.41 MJ/m, coincidentally equivalent to the mean. Twelve wake events exceeded 1 MJ/m. Surprisingly, no statistically significant correlations could be identified between measurements of wake characteristics, vessel characteristics, and/or hydrodynamic conditions.

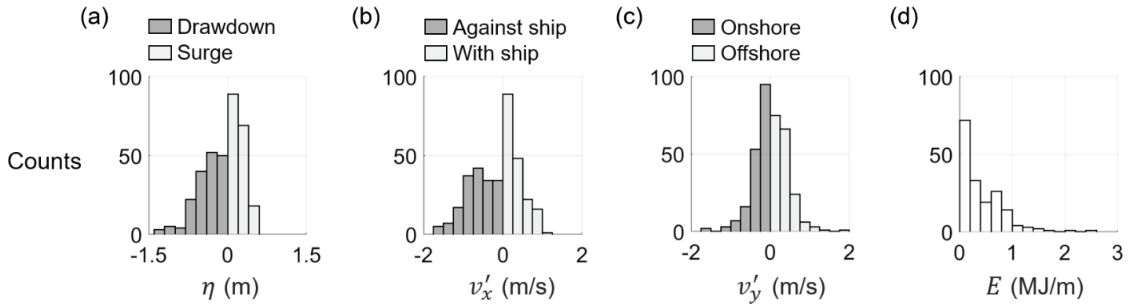

Figure 10: Histograms of Bernoulli wave characteristics measured at Site M during cargo vessel passages in October 2017: (**a**) maximum water level fluctuations (η) of the drawdown and surge, (**b**) alongshore velocity fluctuations (v'_y), (**c**) cross-shore velocity fluctuations (v'_x), and (**d**) energy density of the Bernoulli wave (E).

Low-Frequency Vessel Wake in the South Channel

It was previously assumed that Bird/Long Island shelters Site S from vessel wake, so the dominance of mid-band processes at Site S was an unexpected result. While the mid-band fluctuations in the Site S water levels and velocities do not produce as consistent of a wake signature like that at Site M, spikes in mid-band power do coincide with the passage of cargo vessels.

To further investigate the response in the South Channel to vessel wake generated in the Main Channel, two days of follow-up field measurements were collected on November 8th through 10th, 2018 to search for evidence of LF wake propagation in the South Channel. As shown in **Figure 11**, pressure transducers were deployed at Sites A, C, and D at depths of 2.21, 2.53, and 2.27 m respectively in an array spanning the length of Bird/Long Island in the South Channel. An Aquadopp was deployed at Site B, near the same location as Site S but at a deeper mean depth of 4.19 m. Sampling frequencies varied throughout the measurements but with a minimum of 1/3 Hz, which is sufficient to capture mid-band frequencies.

Following the procedures used previously, AIS data was processed for the Bird/Long Island region during the deployment period, and vessel position data was used to estimate when each vessel passed the two entrances to the South Channel around Bird/Long Island; the entrances are the Intracoastal Waterway and the "blowout" between Bird/Long Island and Cockspur Island. It is assumed that when a vessel passes an entrance, it generates LF wake that propagates both upriver and downriver in the South Channel. The times at which the wake should arrive at the instruments were calculated by modeling the LF wake as a linear shallow-water wave traveling

with celerity $\sqrt{gh_S}$, in which depth h_S represents the spatial mean of depths in the South Channel, approximately 3.5 m, and varies temporally with tidal stage. Although a spatially-varying depth would yield more accurate results, updated and detailed bathymetry with sufficient accuracy for this location is unavailable at this time.

The calculated arrival times were compared to the time series of each instrument and largely coincided with the presence of waves. Notably, waves are in fact introduced into the South Channel at both entrances and propagate both upriver and downriver, regardless of vessel direction. An example event is shown in **Figure 11** for an outbound vessel that first passes the Intracoastal Waterway entrance, where it generates its first South Channel wave, and then 17 minutes later passes the blowout, where it produces another South Channel wave that propagates upriver. Though the waves are largest in amplitude near the entrances from which they originate, they are clearly distinguishable at all instrument locations in the array. This implies that wake can propagate in the South Channel along the full 6 km length of Bird/Long Island, and that sites behind the island receive two sets of wake for a given vessel, one originating from each of its ends. The propagation of wake in opposite directions for a single passage implies that the LF wake in the South Channel has fully detached from the vessel.

This follow-up study confirmed that LF vessel wake readily enters and propagates the 6 km of the South Channel behind Bird/Long Island, and the confirmation that each vessel passages produces two sets of wake lends insight into the large proportion of hydrodynamic energy at Site S that is contributed by mid-band processes. However, substantial questions remain about the relationship between a Bernoulli depression and the LF wake system it generates at the shore, the parameters which govern the proportion of a vessel's wake energy that enters the South Channel, and the extent to which LF wake can propagate into secondary channels.

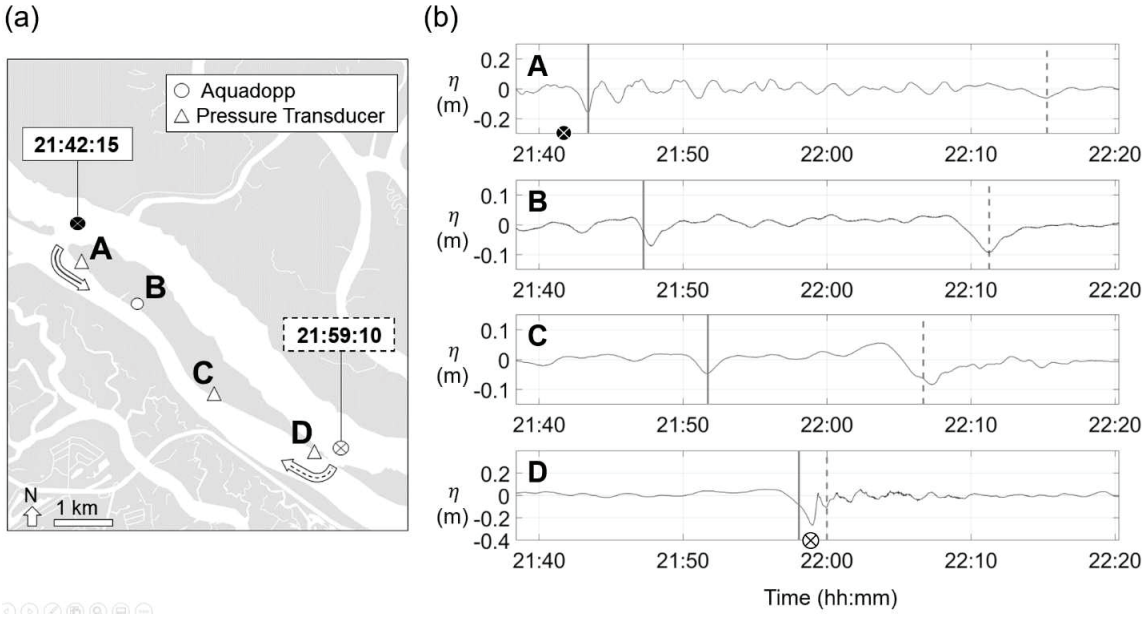

Figure 11: (**a**) Instrument sites and (**b**) detided η time series showing the propagation of LF wake down the South Channel for an outbound container ship. When the vessel passes the north end of Bird/Long Island at 21:42:15, it produces wake (solid line) that propagates southward down the South Channel, past sites A, B, C, and then D. When the vessel reaches the south end of the island at 21:59:10, it produces a second wake (dashed line) that propagates northward up the South Channel past sites D, C, B, and then A.

6. Conclusions

Through the analysis of hydrodynamic measurements and AIS vessel data and the application of a hydrodynamic power-proxy for assessing scarp-relevant erosion potential, it is shown that LF cargo vessel wake is the dominant contributor to erosion for two sites located along Bird/Long Island in the Savannah River: one exposed site (Site M) along the main shipping channel, the Main Channel, and one sheltered site (Site S) in the secondary channel behind the island, the South Channel.

The power-proxy analysis reveals that the mid-band processes, energized by LF vessel wake, account for about 88% of the scarp-relevant power at Site M and 65% of the power at Site S. The mid-band processes are characterized by intermittent strong spikes in power that are directly linked to vessel passages with AIS data. The LF wakes produced by these vessels are characterized by a water level depression, surge, and continued oscillations. The maximum LF wave height recorded in this study was 2.01 m, and the maximum wake-induced velocity magnitude was 2.25 m/s.

Tidal currents accounted for 5% of the scarp-relevant power at Site M and 34% of the power at Site S, although this is likely an overestimate due to expected shoreward reduction of tidal current energy. The effect of the currents was limited at Site M because the currents are weak at spring high tide, the only time when water levels are in contact with the eroding scarp at the back of the beach and thus contributing to the erosion. There is no such limitation at Site S, where the eroding feature is at least partially submerged at all tidal stages.

Because the sites are located upriver and sheltered from wind waves originating from the ocean, wind waves were small. They accounted for 7% of the scarp-relevant power at Site M, and 1% of the power at Site S, which is sheltered by marsh. These values also include the effects of Kelvin wake, which was much smaller in amplitude and energy than LF wake. The measurements did not capture any major storm events, which would increase the significance of wind waves by both increasing water levels with storm surge and producing larger waves.

The significance of LF vessel wake at the sheltered Site S behind Bird/Long Island prompted a follow-up study of wake propagation in the South Channel. These additional measurements confirmed that cargo vessel wake propagates into the South Channel and along, at minimum, the full 6 km extent of the island. Therefore, the scarp-relevant effects of LF wake are not limited to shorelines directly exposed to the shipping channel.

The difference between the findings presented here Bird/Long Island and those reported at Cockspur Island, a neighboring island in the Savannah River, by Houser (2010) illustrate that the relative significance of erosive processes can exhibit high spatial variability. Cockspur Island is closer to the mouth of the Savannah River and subject to large wind-waves originating in the ocean, while Bird/Long Island is entirely sheltered from oceanic wind waves. Furthermore, the large vessel speed restrictions in place at Cockspur Island but not at Bird/Long Island likely plays a key role in the overall significance of large vessel wake. However, additional work is needed to robustly relate vessel and hydrodynamic conditions to the characteristics of the LF wake as it presents on the shallow-water margins of shipping channels.

Acknowledgements: The authors would like to thank the Georgia Department of Transportation, Office of Research for funding this work under contract 0015304, the United States Army Corps of Engineers for their assistance with AIS data, and the boat captains at Skidaway Institute of Oceanography Marine Operations for their help with instrument deployment and recovery.

References

Alexander, C., and Calabria, J. (2019). Bird-Long Island Management Study Phase 1A: The Application of Geospatial Tools to Qualify Shoreline Change and the Threat to Cultural and Natural Resources on Bird-Long Island (No. FHWA-GA-19-1633). Georgia. Dept. of Transportation.

Brown, E. D., Buchsbaum, S. B., Hall, R. E., Penhune, J. P., Schmitt, K. F., Watson, K. M., and Wyatt, D. C., (1989). "Observations of a Nonlinear Solitary Wave Packet in the Kelvin Wake of a Ship," J. Fluid Mech., 204, pp. 263–293.

Defne, Z., Haas, K. A., Fritz, H. M., Jiang, L., French, S. P., Shi, X. & Stewart, K. M. (2012). National geodatabase of tidal stream power resource in USA. Renewable and Sustainable Energy Reviews, 16(5), 3326-3338.

Defne, Z., Haas, K. A., & Fritz, H. M. (2011). Numerical modeling of tidal currents and the effects of power extraction on estuarine hydrodynamics along the Georgia coast, USA. Renewable Energy, 36(12), 3461-3471.

Didenkulova, I., Parnell, K. E., Soomere, T., Pelinovsky, E., and Kurennoy, D. (2009). Shoaling and runup of long waves induced by high-speed ferries in Tallinn Bay. Journal of Coastal Research, 491-495.

Didenkulova, I., Sheremet, A., Torsvik, T., and Soomere, T. (2013). Characteristic properties of different vessel wake signals. Journal of Coastal Research, (65), 213-218.

Durkee, P. A., Chartier, R. E., Brown, A., Trehubenko, E. J., Rogerson, S. D., Skupniewicz, C., and Nielsen, K. E., (2000). Composite Ship Track Characteristics. J. Atmos. Sci., 57, pp. 2542–2553.

El-Kiki, M., Hamed, Y., Balah, M., and Kitamura, E. (2007). Experimental study on effects of ship movement in narrow navigation channel side slopes on water surface profile fluctuations. Port-Said Engineering Research Journal 11(2), 11-14.

Fenical, S., MacDonald, N., and Yang, F. (2002). Vessel hydrodynamic investigations. In Proc 1st Onshore and Offshore Pollution Prevention Symposium and Technology Exhibition.

Garel, E., Fernández, L. L., and Collins, M. (2008). Sediment resuspension events induced by the wake wash of deep-draft vessels. Geo-Marine Letters, 28(4), 205-211.

Georgia Ports Authority (2021a). Port of Savannah Total Annual Container Trade for Calendar Years 2016 through 2020. By the Numbers. *https://gaports.com/wp-content/uploads/2021/03/CY20-Annual-Container-Trade.pdf?1649772178.* Accessed 4/10/2022.

Georgia Ports Authority (2021b). Port of Savannah Total Annual Vessel Calls for Calendar Years 2016 through 2020. By the Numbers. *https://gaports.com/wp-content/uploads/2021/03/CY20-Annual-Vessel-Calls-Savannah.pdf?1649696120.* Accessed 4/10/2022.

Gharbi, S., Valkov, G., Hamdi, S., and Nistor, I. (2010). Numerical and field study of ship-induced waves along the St. Lawrence Waterway, Canada. Natural hazards, 54(3), 605-621.

Gourlay, T. P. (2001). The supercritical bore produced by a high-speed ship in a channel..

Herbich, J. B., and Schiller Jr, R. E. (1984). Surges and waves generated by ships in a constricted channel. In Coastal Engineering 1984 (pp. 3212-3226).

Hochstein, A. B., and Adams Jr, C. E. (1986). A Numerical Model of the Effects of Propeller Wash and Ship-Induced Waves from Commercial Navigation in an Extended Navigation Season on Erosion, Sedimentation, and Water Quality in the Great Lakes Connecting Channels and Harbors. US Army Corps of Engineers. Baton Rouge, Louisiana.

Hochstein, A. B., and Adams, C. E. (1989). Influence of vessel movements on stability of restricted channels. Journal of Waterway, Port, Coastal, and Ocean Engineering, 115(4), 444-465.

Houser, C. (2010). Relative importance of vessel-generated and wind waves to salt marsh erosion in a restricted fetch environment. Journal of Coastal Research, 26(2 (262)), 230-240.

Houser, C. (2011). Sediment resuspension by vessel-generated waves along the Savannah River, Georgia. Journal of Waterway, Port, Coastal, and Ocean Engineering, 137(5), 246-257.

Johnson, J. W. (1958). Ship waves in navigation channels. In Proc. of 6th Conf. on Coastal Eng., Florida, 666-690.

Katsis, C., & Akylas, T. R. (1987). On the excitation of long nonlinear water waves by a moving pressure distribution. Part 2. Three-dimensional effects. Journal of Fluid Mechanics, 177, 49-65.
Kelpšaite, L., Parnell, K. E., and Soomere, T. (2009). Energy pollution: the relative influence of wind-wave and vessel-wake energy in Tallinn Bay, the Baltic Sea. Journal of Coastal Research, 812-816.
Kirkegaard, J., Kofoed-Hansen, H., and Elfrink, B. (1998). Wake wash of high-speed craft in coastal areas. In Coastal Engineering 1998 (pp. 325-337).
Lee, L. M., Tate, J. N., and Berger, R. C. (2005). Texas City ship channel deepening study, hydrodynamic model.
Lee, S. J., Yates, G. T., & Wu, T. Y. (1989). Experiments and analyses of upstream-advancing solitary waves generated by moving disturbances. Journal of Fluid Mechanics, 199, 569-593.
MacDonald, N. J. (2003). Numerical modelling of coupled drawdown and wake. In Proc Canadian Coastal Conf (pp. 15-17).
Macfarlane, G. J., and Graham-Parker, K. J. (2019). Marine vessel wave wake: transient effects when accelerating or decelerating. Journal of Waterway, Port, Coastal, and Ocean Engineering, 145(1), 04018027.
Maynord, S. (1996). Return velocity and drawdown in navigable waterways. Army Engineer Waterways Experiment Station, Vicksburg, MS, Hydraulics Lab.
Maynord, S.T. (2007). Ship Forces on the Shoreline of the Savannah Harbor Project." Technical Report ERDC/CHL TR-07-7. US Army Corps of Engineers, Engineer Research and Development Center, Vicksburg, MS.
Munk, W. H., Scully-Power, P., and Zachariasen, F., (1987). Ships From Space, The Bakerian Lecture 1986. Proc. R. Soc. London, Ser. A, 412, pp. 231–254.
National Oceanic and Atmospheric Administration (2022). Continental United States Hurricane Impacts/Landfalls 1851-2020. Hurricane Research Division, Atlantic Oceanographic and Meteorological Laboratory. *https://www.aoml.noaa.gov/hrd/hurdat/All_U.S._Hurricanes.html*. Accessed 04/11/2022.
Parnell, K. E., McDonald, S. C., and Burke, A. E. (2007). Shoreline effects of vessel wakes, Marlborough Sounds, New Zealand. Journal of Coastal Research, 502-506.
Parnell, K., Delpeche, N., Didenkulova, I., Dolphin, T., Erm, A., Kask, A., ... and Soomere, T. (2008). Far-field vessel wakes in Tallinn Bay. Estonian Journal of Engineering, 14(4).
Parnell, K., Kofoed-Hansen, H. (2001). Wakes from large high-speed ferries in confined coastal waters: Management approaches with examples from New Zealand and Denmark. Coastal Management, 29 (3), 217–237. DOI: 10.1080/08920750152102044
Rapaglia, J., Zaggia, L., Ricklefs, K., Gelinas, M., and Bokuniewicz, H. (2011). Characteristics of ships' depression waves and associated sediment resuspension in Venice Lagoon, Italy. Journal of Marine Systems, 85(1-2), 45-56.
Scarpa, G. M., Zaggia, L., Manfè, G., Lorenzetti, G., Parnell, K., Soomere, T., ... and Molinaroli, E. (2019). The effects of ship wakes in the Venice Lagoon and implications for the sustainability of shipping in coastal waters. Scientific reports, 9(1), 1-14.
Shi, F., Malej, M., Smith, J. M., and Kirby, J. T. (2018). Breaking of ship bores in a Boussinesq-type ship-wake model. Coastal Engineering, 132, 1-12.
Schijf, J. (1949). Proceedings of the 17th International Navigation Congress. PIANC, Section 1, Subject 2, Lisbon, 61-78.
Shepsis, V., Fenical, S., Hawkins-Bowman, B., Dohm, E., and Yang, F. (2001). Deep-Draft Vessels in Narrow Waterway: Port of Oakland 50-Foot Deepening Project. In Ports' 01: America's Ports: Gateway to the Global Economy,1-10.
Soomere, T. (2006). Nonlinear ship wake waves as a model of rogue waves and a source of danger to the coastal environment: a review. Oceanologia, 48(S).
Sorensen RM (1997) Prediction of vessel-generated waves with reference to vessels common to the upper Mississippi River System. ENV Report 4, US Army Corps of Engineers, 50 pp.
Stockstill, R. L., and Berger, R. C. (1994). HIVEL2D: A two-dimensional flow model for high-velocity channels (No. WES/TR/REMR-HY-12). Army Engineering Waterways Experiment Station Vicksburg, MS..
Thomson, W. (1887). On ship waves. *Proceedings of the Institution of Mechanical Engineers*, *38*(1), 409-434.

Torsvik, T., Dysthe, K., and Pedersen, G. (2006). Influence of variable Froude number on waves generated by ships in shallow water. Physics of Fluids, 18(6), 062102.
United States Army Corps of Engineers (USACE) (2008). Coastal Engineering Manual. Engineering Manual: 1110-2-1100.
Velegrakis, A. F., Vousdoukas, M. I., Vagenas, A. M., Karambas, T., Dimou, K., and Zarkadas, T. (2006). Field observations of waves generated by passing ships: A note. Coastal Engineering, 54(4), 369-375.
Wu, T. Y. (1987). Generation of Upstream Advancing Solitons by Moving Disturbances. J. Fluid Mech., 184, pp. 75–99.
Zaggia, L., Lorenzetti, G., Manfé, G., Scarpa, G. M., Molinaroli, E., Parnell, K. E., and Soomere, T. (2017). Fast shoreline erosion induced by ship wakes in a coastal lagoon: Field evidence and remote sensing analysis. PloS one, 12(10).

JOURNAL OF GEOPHYSICAL RESEARCH, VOL. 115, D08301, doi:10.1029/2009JD012675, 2010

Quantification of NO_2 and SO_2 emissions from the Houston Ship Channel and Texas City industrial areas during the 2006 Texas Air Quality Study

Claudia Rivera,[1] Johan Mellqvist,[1] Jerker Samuelsson,[1] Barry Lefer,[2] Sergio Alvarez,[3] and Monica R. Patel[2]

Received 16 June 2009; revised 21 November 2009; accepted 10 December 2009; published 23 April 2010.

[1] In August–September 2006, as part of the Second Texas Air Quality Study, NO_2 and SO_2 emissions from the Houston Ship Channel and Texas City industrial areas were quantified using mobile mini-differential optical absorption spectroscopy instruments. The measured NO_2 emissions from the Houston Ship Channel and Texas City industrial areas were 2542 and 452 kg h^{-1}, respectively, yielding NO_x emissions 70% and 43%, respectively, above the reported inventory values. Quantified SO_2 emissions from the Houston Ship Channel area were 1749 kg h^{-1} and were found to be 34% above the values reported in the inventory. Short-term variability of NO_2 and SO_2 emissions was found at the Houston Ship Channel. On 31 August 2006, a plume was detected at the HSC during three consecutive measurements, yielding a HCHO flux of 481 kg h^{-1}. This event has been mainly attributed to photochemical production.

Citation: Rivera, C., J. Mellqvist, J. Samuelsson, B. Lefer, S. Alvarez, and M. R. Patel (2010), Quantification of NO_2 and SO_2 emissions from the Houston Ship Channel and Texas City industrial areas during the 2006 Texas Air Quality Study, *J. Geophys. Res.*, *115*, D08301, doi:10.1029/2009JD012675.

1. Introduction

[2] Air pollution is a problem in many cities of the world, and the Houston-Galveston, Texas, area (HGA) is no exception, with one of the most severe ozone (O_3) problems in the United States. The process of tropospheric O_3 production by photochemical oxidation of industrial hydrocarbons involving NO and NO_2 as catalysts has been described in the literature [*Crutzen*, 1979]. This process is highly dependent on the concentration and chemical composition of hydrocarbons [*Grover and Bradford*, 2001], as well as on NO_x [*Jacob et al.*, 1996; *Kasibhatla et al.*, 1991; *Martin et al.*, 2002; *Murphy et al.*, 1993; *Penner et al.*, 1991]. Both NO_x and VOCs are a product of combustion processes, from either stationary or mobile sources, and have biogenic sources as well [*Conley et al.*, 2005; *Finlayson-Pitts and Pitts*, 2000]. In the HGA, emissions of these compounds are associated with petrochemical industrial facilities as well as traffic [*Berkowitz et al.*, 2005; *Buzcu-Guven and Fraser*, 2008; *De Gouw et al.*, 2009; *Gilman et al.*, 2009; *Jobson et al.*, 2004; *Leuchner and Rappenglück*, 2010; *Smith et al.*, 2007; *Xie and Berkowitz*, 2007].

[3] The Texas Air Quality Study 2000 (TexAQS 2000) demonstrated that industrial complexes in the HGA are large emitters of NO_x and hydrocarbons, which originate spatially localized plumes rich in O_3 and hydrocarbon oxidation products (i.e., formaldehyde) [*Daum et al.*, 2003, 2004; *Kleinman et al.*, 2002; *Ryerson et al.*, 2003]. Detailed studies have demonstrated that the high O_3 production rates in the HGA are linearly dependent on the ratio of total nonmethane hydrocarbons to NO_x [*Berkowitz et al.*, 2005]. In the HGA, the production tends to be more rapid and efficient than in other urban areas [*Kleinman et al.*, 2002; *Lei et al.*, 2004]. In addition a detailed particulate growth study in the HGA concluded that SO_2-rich plumes were associated with particle formation and substantial particle volume growth [*Brock et al.*, 2003].

[4] Formaldehyde has a very short lifetime (generally 2–4 h) in the presence of sunlight, which is determined mainly by photolysis and reaction with OH radicals [*Garcia et al.*, 2006; *Wert et al.*, 2003]. It can be directly emitted by incomplete combustion or industrial processes or be secondarily formed by oxidation of VOCs [*Finlayson-Pitts and Pitts*, 2000]. Studies have shown that oxidation of ethene, propene, and isoprene tends to efficiently produce HCHO [*Dodge*, 1990; *Goldan et al.*, 2000; *Lee et al.*, 1998; *Wert et al.*, 2003]. During TexAQS 2000, *Wert et al.* [2003] concluded that there was no evidence for strong primary emissions of HCHO when compared to the secondary emissions produced in several Houston area plumes.

[5] Worsening air quality in the HGA has increased the concern of the general public and policymakers regarding

[1]Radio and Space Science, Chalmers University of Technology, Gothenburg, Sweden.
[2]Department of Geosciences, University of Houston, Houston, Texas, USA.
[3]Institute for Air Science, Baylor University, Waco, Texas, USA.

0148-0227/10/2009JD012675

environmental problems generated by outdoor pollution and its relationship with human health [*Brody et al.*, 2004; *Conley et al.*, 2005]. Because O_3 threshold mixing ratios established by the National Ambient Air Quality Standard are frequently exceeded, the HGA has been designated an O_3 nonattainment region, and it is therefore important to identify and quantify O_3 precursors and reduce their emissions [*Allen et al.*, 2004; *Byun et al.*, 2007; *Grover and Bradford*, 2001; *Kleinman et al.*, 2002]. With the objective to provide detailed accurate emission information, a 5-week field campaign in the HGA was performed during the summer of 2006. NO_2, SO_2, and HCHO differential vertical columns were quantified in the Houston Ship Channel (HSC) and Texas City (TC) industrial areas by traversing the plume of these industrial complexes using a mini-differential optical absorption spectroscopy (DOAS) instrument installed on a car. The DOAS measurements of NO_2 and SO_2 presented here were conducted in parallel with airborne and mobile solar IR measurements to quantify VOC emissions [*De Gouw et al.*, 2009]. The latter study shows large discrepancies between measured and reported emissions. It was therefore of great interest to investigate whether discrepancies exist also for NO_2 and SO_2 emissions. The objective of this paper is to determine the consistency of our measurements with available emission inventories of the HGA.

2. Method and Data Analysis

[6] DOAS is a technique that allows the remote detection of trace gases. It is based on the absorption of electromagnetic radiation by matter and is widely used for continuously quantifying atmospheric gases [*Finlayson-Pitts and Pitts*, 2000; *Platt*, 1994; *Platt et al.*, 1979; *Platt and Stutz*, 2008]. DOAS measurements can be performed using a wide variety of experimental setups. In this field campaign, passive DOAS using scattered sunlight by air molecules and particles has been used in zenith scattered light configuration. Zenith scattered sunlight measurements offer a large variety of applications, are one of the earliest applications of passive DOAS, and have been used to study stratospheric chemistry and the radiative transport in clouds [*Platt and Stutz*, 2008].

2.1. Mobile Mini-Differential Optical Absorption Spectroscopy

[7] A mobile miniDOAS instrument, described in detail by *Galle et al.* [2002], was used to perform the measurements presented in this paper. MiniDOAS instruments have been widely adopted by the scientific community to quantify emissions from urban [*Johansson et al.*, 2008, 2009], industrial [*McGonigle et al.*, 2004; *Rivera et al.*, 2009], and volcanic [*Bobrowski et al.*, 2003; *Bobrowski and Platt*, 2007; *Galle et al.*, 2002; *Mori et al.*, 2006] sources. Our system utilizes an 8 mrad field of view telescope to collect scattered UV light. The telescope has a quartz lens and, only for SO_2 measurement purposes, a Hoya U-330 filter was used to reduce stray light, blocking visible light with wavelength higher than 360 nm. The telescope is then coupled to a 600 μm quartz fiber optic which transfers light into an Ocean Optics S2000 spectrometer with spectral resolution of approximately 0.6 nm and spectral range of 280–420 nm (SO_2 and HCHO) and 336–480 nm (NO_2). The spectrometer and a GPS were connected to a laptop computer controlled by custom-built software, Mobile DOAS [*Johansson and Zhang*, 2004], which acquired and preliminarily evaluated spectra in real time.

2.2. Measurement Method

[8] The mobile miniDOAS instrument was mounted on a car and aligned toward zenith, and spectra were recorded encircling the sources of pollution. Differential vertical columns of the species of interest were measured upwind and downwind of the sources in order to derive inflow and outflow, respectively, with the flux being the difference between them. For the Texas City industrial area, measurements were conducted traversing the downwind plume. Typically measurements were done 100 m to about 10 km (only the case of the HSC industrial area) downwind of the sources since these are distributed over large areas with no accessibility except for public roads. Every measurement series started with the recording of a background reference spectrum, considered to be the reference for all the following spectra recorded during the measurement series. Ideally the reference spectrum is expected not to include any concentration above ambient of the trace species of interest; however, in urban and industrial areas this is difficult to achieve, and therefore our measurement in this case will produce the difference in vertical columns between the background reference spectrum and all measured spectra across the plume for every measurement series. All vertical columns derived from spectra collected after the reference spectrum are relative to the latter and will be further referred to as differential vertical columns.

[9] It is important to notice that we have assumed that the light path is vertical and no air mass factor has been applied to the differential vertical columns, which could bring uncertainties to the results of our measurements. The measurements presented in this study were conducted during days of clear blue sky without presence of clouds. In order to give insight for high aerosol loads which could lead to enhanced light paths through multiple scattering, the oxygen dimer (O_4) was included into the DOAS fit. All measurements conducted during the field campaign that showed indication of enhanced light paths during the traverses were disregarded. More details about this procedure are given by *Johansson et al.* [2008]. In section 2.5, the uncertainty related to light path extension inside the plume (multiple scattering) as well as to scattering of photons into the instrument's field of view by particles beneath the plume (light dilution) is further discussed.

[10] Stratospheric NO_2 variations are expected to be small in the short time period (few minutes to 1 h) our measurements take when compared with tropospheric NO_2 variations present in the polluted plumes we are quantifying. In addition, using a background reference spectrum for each measurement series eliminates the stratospheric NO_2 part and has less influence of instrumental instabilities, as already pointed out by *Sinreich et al.* [2005].

[11] GPS data were recorded providing time and position before and after each spectrum was collected. Fluxes from traverses were calculated by multiplying differential total vertical columns by the distance traversed perpendicular to the wind direction and by the wind speed. Wind information

Table 1. Fitting Intervals and Molecules Included in the Differential Optical Absorption Spectroscopy Fit

Fitting Interval Wavelength Range (nm)	Species
310–325	SO_2, O_3, NO_2, HCHO, Ring
324–347	HCHO, O_3, NO_2, SO_2, O_4, Ring
420–460	NO_2, O_3, O_4, H_2O, Ring

was obtained from GPS sondes regularly launched during the field campaign (see section 2.4).

2.3. Spectral Evaluation

[12] SO_2, HCHO, and NO_2 were retrieved from the recorded spectra using the WinDOAS software (version 2.1) (*Van Roozendael and Fayt*, 2001) in the wavelength regions of 310–325, 324–347, and 420–460 nm, respectively. This procedure has been described in detail elsewhere [*Galle et al.*, 2002; *Platt and Stutz*, 2008]. The cross sections used in the DOAS fit (SO_2 [*Bogumil et al.*, 2003], HCHO [*Meller and Moortgat*, 2000], and NO_2 [*Vandaele et al.*, 1998]) were collected from the literature and degraded to our instrument's resolution. In addition, the cross sections of O_3 [*Voigt et al.*, 2001], O_4 [*Hermans et al.*, 1999], and H_2O [*Coheur et al.*, 2002; *Fally et al.*, 2003] were included in the fitting procedure as well. To compensate for the filling up of the Fraunhofer lines in the solar spectrum by inelastic scattering, the so-called Ring effect [*Platt and Stutz*, 2008], a synthetic Ring spectrum calculated from a high-resolved solar spectrum (R. L. Kurucz, I. Furenlid, J. Brault, and L. Testerman, 1984, Solar flux atlas from 296 to 1300 nm) (http://kurucz.harvard.edu/sun/fluxatlas/) using the DOASIS software [*Kraus*, 2003] was also included in the fit. Details of every fitting interval and cross sections used are shown in Table 1. Examples of DOAS fits for NO_2, HCHO, and SO_2 are shown in Figure 1. The number of spectra collected for the SO_2 and NO_2 measurements was in all cases automatically adapted to give a time resolution of approximately 5 s per measurement point. However, for HCHO evaluation, spectra were coadded in order to increase the signal-to-noise ratio, resulting in a time resolution of 86 s per measurement point.

2.4. Wind Data

[13] Wind speed and wind direction data were obtained from wind fields recorded by GPS balloon sondes (RS80-15N-V2D-A-GPS) obtained from Environmental Science Corporation, Boulder, Colorado. GPS sondes were launched in between our measurements and nearby the measurement paths used. Typically, three or four balloon sondes were launched every day; the rise speed of the balloons was typically 5 m s^{-1}. In the HSC the soundings were carried out close to the Lynchburg Ferry crossing (Figure 2), and in Texas City the soundings were launched westward of the town (Figure 3). When balloon sondes were not available, wind data were used from a radar profiler operated by the Texas Commission of Environmental Quality within the NOAA profiler network at the La Porte Airport south of the HSC.

[14] The measurements presented in this study were conducted in sunny conditions. Under these conditions the industrial emission plumes mix rather quickly in the vertical, giving a homogeneous distribution of the pollutants versus height through the mixing layer even several kilometers downwind. In addition to the atmospheric mixing, the plumes from process industries exhibit an initial lift since they are usually hotter than the surrounding air. This assumption of rapid mixing agrees with Doppler lidar measurements conducted from the ship RV *Ronald H. Brown* by NOAA during the TexAQS 2006 [*Tucker et al.*, 2009]. From these measurements information about mixing height and the vertical mixing of the atmosphere could be obtained showing typical daytime vertical mixing speeds of ± (0.5–1.5) m s^{-1}.

[15] The measurements presented in this study were typically conducted at a plume transport time of 200–500 s

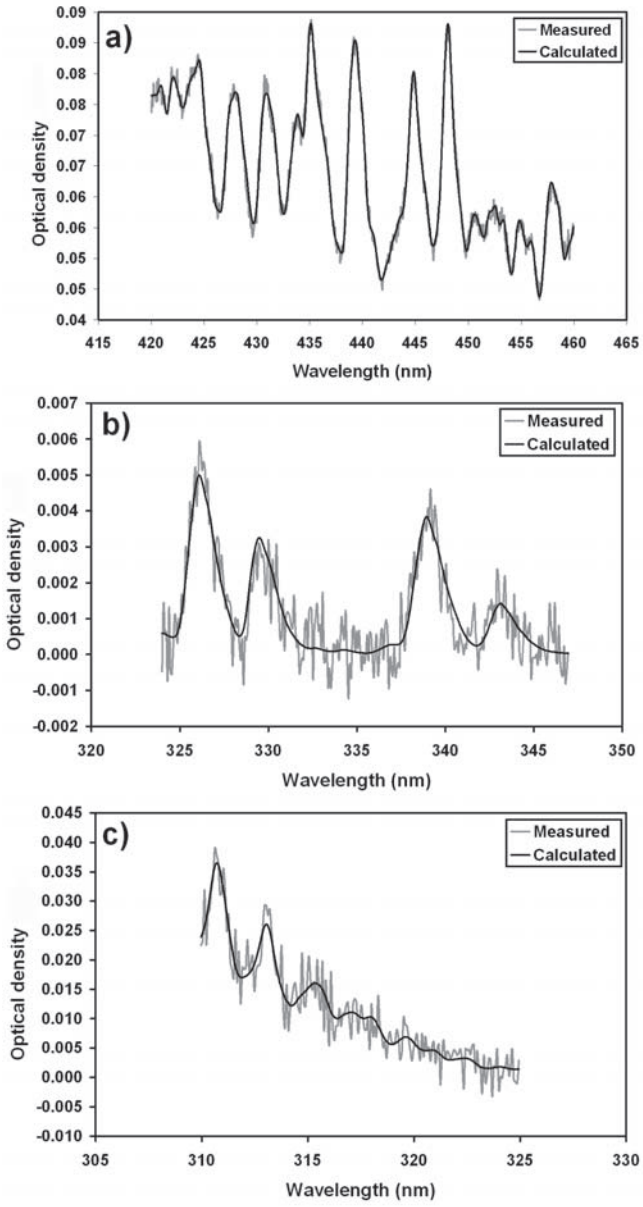

Figure 1. Examples of differential optical absorption spectroscopy (DOAS) fit in different wavelength regions. Fitted cross sections of (a) NO_2 in the wavelength region of 420–460 nm, (b) HCHO in the wavelength region of 324–347 nm, and (c) SO_2 in the wavelength region of 310–325 nm.

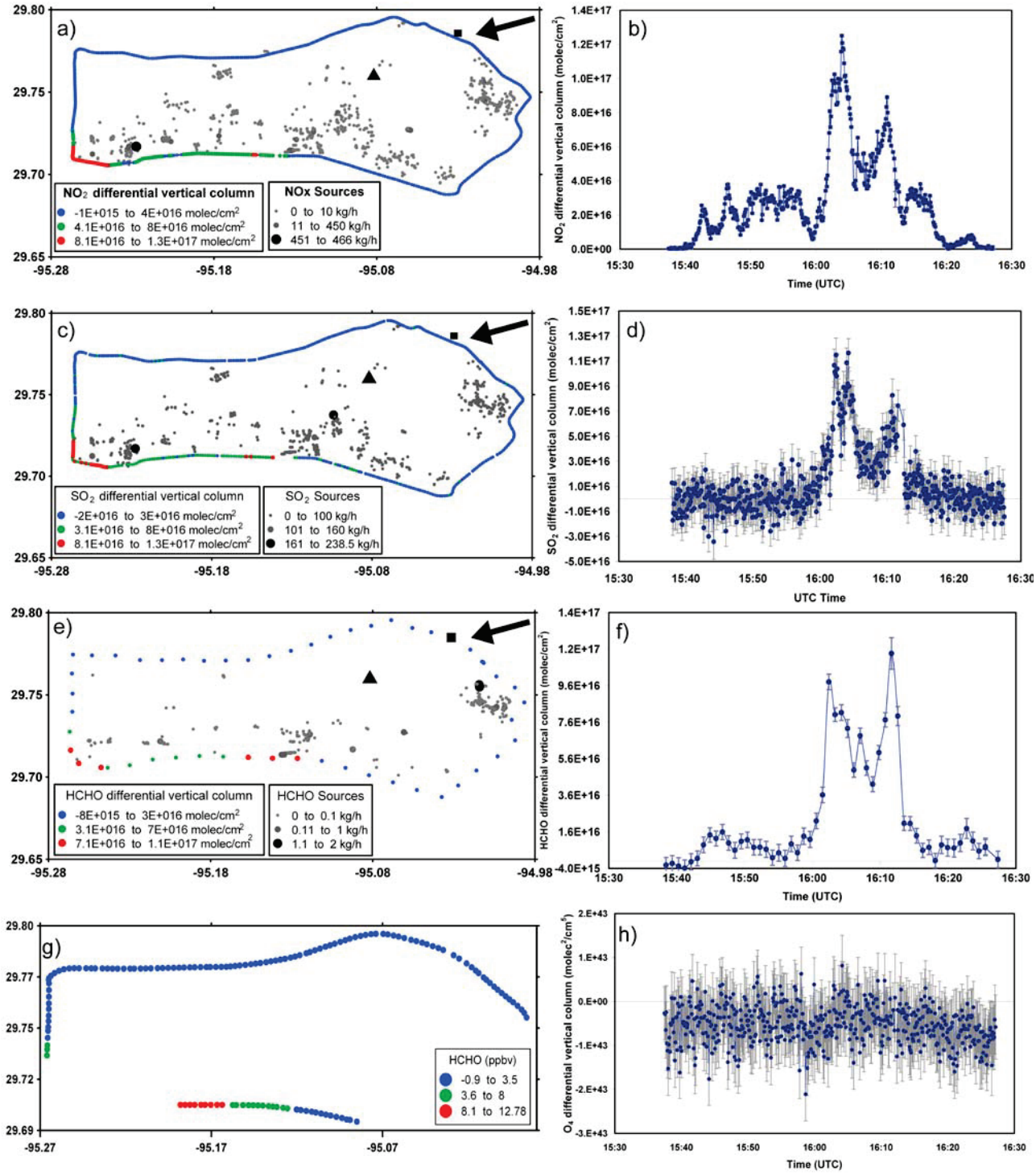

Figure 2. Measurement performed on 31 August 2006 starting at 1037 LT at the Houston Ship Channel. Shown are the spatial distributions of (a) NO_2, (c) SO_2, and (e) HCHO along the Houston Ship Channel quantified during the traverse, the measured differential vertical columns of (b) NO_2, (d) SO_2, and (f) HCHO, (g) the spatial distribution of HCHO measured by the Piper Aztec aircraft, and (h) the differential vertical column of O_4 measured during the traverse. The black square indicates the starting point of the traverse. The site where balloon sondes were launched (close to the Lynchburg Ferry crossing) is indicated by a black triangle. In gray scale, the known NO_x, SO_2, and HCHO sources from the EI in the HSC are shown. The black arrow at the right upper corner of Figures 2a, 2c, and 2e indicates the wind direction obtained from wind fields recorded by a GPS balloon sonde launched at 0953 LT.

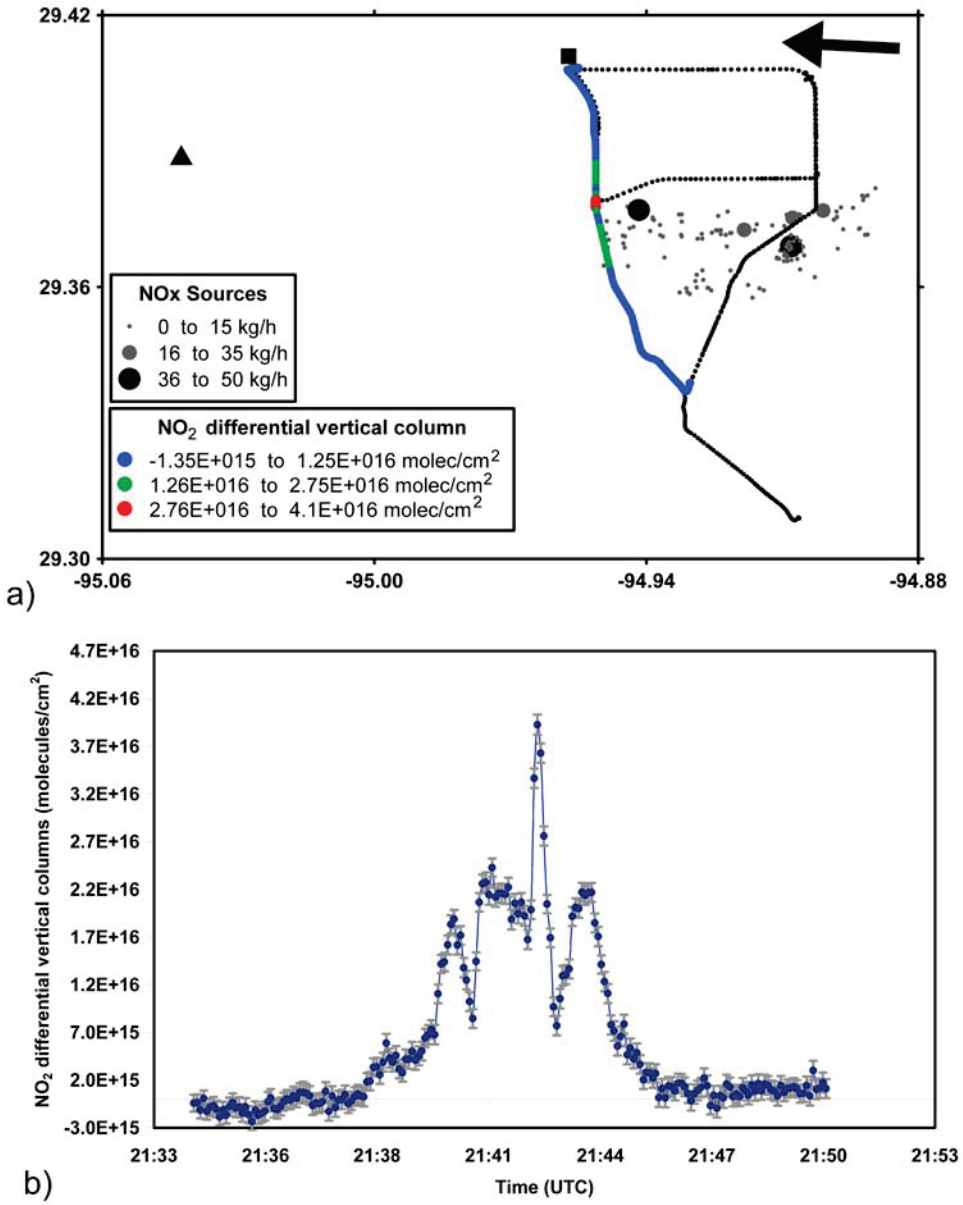

Figure 3. Measurement performed on 20 September 2006 starting at 1634 LT at Texas City. (a) The spatial distribution of NO_2 along the measurement path quantified during the traverse. (b) Measured differential vertical columns of NO_2 along the traverse. The black square indicates the starting point of the traverse. The site where balloon sondes were launched is indicated by a black triangle. In gray scale, the known NO_x sources from the EI in Texas City are shown. The black arrow at the right upper corner of Figure 3a indicates the wind direction obtained from wind fields recorded by a GPS balloon sonde launched at 1428 LT.

downwind of the industries, which, according to the discussion above, means that sufficient time has elapsed for the emission plume to mix at heights of up to several hundred meters above the ground. For this reason we have used the average wind over the lower 500 m of the atmosphere as a proxy for the mass-weighted wind.

2.5. Emission Error Estimation

[16] Several types of errors can affect the calculation of emissions using a miniDOAS instrument. A spectroscopic error is related to errors in the absorption cross sections, temperature changes in the spectrometer, fitting errors, and spectral interferences. The spectroscopic error in this study reflects the error in calculated emissions due to the DOAS retrieval of the differential vertical column and was calculated as 10%, 14%, and 40% for NO_2, HCHO, and SO_2 respectively.

[17] A scattering error is expected due to light path extension inside the plume (multiple scattering) as well as to scattering of photons into the instrument's field of view by particles beneath the plume (light dilution). The scattering error strongly depends on meteorological conditions (i.e., cloud coverage, fog, and rain) [*Millán*, 1980; *Moffat and Millán*, 1971] and changes as a function of the distance of

Table 2. Summary of Total Quantified Fluxes (Median) and Comparison With Emissions Inventory[a]

NO_2		NO_x (kg h^{-1})		SO_2			HCHO		
Flux (kg h^{-1})	No. Meas.	Adjusted Values[b]	EI	Flux (kg h^{-1})	No. Meas.	EI	Flux (kg h^{-1})	No. Meas.	EI
Houston Ship Channel									
2542 (214)	9	3435 (289)	2015	1749 (160)	3	1308	481 (21)	3	14
Texas City									
452 (115)	11	619 (158)	433						

[a]The median absolute deviation from the median is shown in parentheses. Abbreviation is as follows: EI, emission inventory.
[b]The NO_x fluxes have been adjusted from the original quantified total NO_2 values according to the NO_2/NO_x ratio derived by aircraft measurements: 0.74 for Houston Ship Channel and 0.73 for Texas City. NO_x fluxes have no further correction applied for rapid photochemical NO_x loss.

the instrument from the plume and the wavelength region used in the DOAS retrieval, becoming more significant at shorter wavelengths for the case of SO_2 [*Mori et al.*, 2006]. Because the measurements presented in this study were conducted during days of clear blue sky without presence of clouds and care was taken to disregard measurements with clear indication of enhanced light paths during the traverses (see section 2.2), the scattering error was assumed to be 10% for this study.

[18] The main uncertainty, however, is due to assumptions about the vertical distribution of the plume, which will lead to errors in attributing the true wind speed for each molecule in the plume. Because we are not able to calculate the plume height with our measurements, we have assumed that the emission plume from an industry mixes rather quickly vertically, due to convection from solar heating of the ground, with a speed of about 0.5–1.5 m s^{-1} in addition to initial plume lifting due to high temperature. Further discussion about the wind data used in this study can be found in section 2.4 and the paper of *Mellqvist et al.* [2010]. Uncertainty in the wind speed and wind direction from GPS balloon sondes, used to calculate emissions presented in this study, is about 30% [*Mellqvist et al.*, 2010]. Our estimated uncertainty in the wind field accounts for possible measurement errors and systematic spatial wind differences, in addition to errors in estimated plume height and therefore errors in wind speed and wind direction used to calculate fluxes, as well as errors due to changes in wind speed and wind direction during the period of time a measurement is being conducted. Further details about expected errors using this technique are given by *Johansson et al.* [2008] and *Rivera et al.* [2009].

[19] Another uncertainty regarding the measurement method is the fact that the measurements are conducted using a mobile van and driving on roads exposed to traffic emissions. Because in this study it is not possible to separate industrial plumes from traffic emissions, we have assumed that emissions from traffic are negligible compared to emissions by industries and form part of the background emissions.

[20] The combined uncertainty for calculated emissions taking into consideration all errors and uncertainties is therefore 33%, 35%, and 51% for NO_2, HCHO, and SO_2, respectively.

2.6. Airborne Measurements

[21] A Piper Aztec (N6670Y) aircraft operated by the Baylor Institute for Air Science conducted several research tasks during the TexAQS 2006 field experiment. Aircraft-based measurements were focused on the collection of lower tropospheric air quality data from August through October 2006 in the Houston region.

[22] NO, NO_2, HCHO, and reactive alkenes, among other parameters, were measured during the conducted flights. NO and NO_2 data recorded during flights conducted on the same measurement paths as our measurements by the Piper Aztec aircraft were used in this study with the objective to gain knowledge of the NO_2/NO_x ratio. NO was measured using an Eco Physics CLD 77. NO_2 mixing ratios were measured using the photolysis-chemiluminescence technique [*Kley and McFarland*, 1980], consisting of a Thermo Environmental 42C instrument and a Droplet Measurement Technologies BLC photolytic converter. Baseline corrections, from the periodic in-flight zeroing of the instruments, were applied automatically for both species. Corrections for both ambient water and pressure were also applied. The uncertainty of NO and NO_2 was 0.4 and 0.2 ppbv, respectively [*Alvarez et al.*, 2007].

3. Results and Discussion

[23] Measurements were performed between 30 August and 29 September 2006 aimed at quantifying emissions from different areas in the HGA. All measurements were compared with reported values in order to give insight into the consistency of our measurements with the available emission inventories of the area. An emissions inventory (EI) developed by the Texas Commission on Environmental Quality was used in this study (the 2006 Point Source Emissions Inventory) (http://www.tceq.state.tx.us/implementation/air/industei/psei/psei.html). It contains daily averaged emission data for approximately 3000 sources for the time period 15 August to 15 September 2006. During this period, some industrial facilities in the HGA reported their monitored hourly emissions of NO_x, SO_2, and VOCs, among other pollutants. In the EI used, these data have been merged with an annual database, providing daily emissions for sources not included in the hourly monitored data set. It is important to notice that daily emissions reported by the industries show very little variability (about 1%) during the days our measurements were compared with the inventory.

[24] Table 2 shows a comparison between the median of total fluxes measured in this field study and reported emissions in the inventory for HSC and TC sites. The median absolute deviation from the median (MAD) refers to the variability of daily quantified fluxes during the field campaign and not to uncertainty of the measurement itself (discussed in section 2.5). In addition, a detailed account of

Table 3. NO_2, SO_2, and HCHO Quantified Fluxes During the Field Campaign

Date	Start Time (LT)	Species	Wind Direction (°)	Wind Speed (m s^{-1})	Flux (kg h^{-1})
		Houston Ship Channel			
31 Aug 2006	0833	NO_2	75	2.07	2756
	0946	NO_2	75	2.07	2650
		HCHO			542
	1037	NO_2	75	2.07	2540
		SO_2			3493
		HCHO			481
	1153	NO_2	85	2.04	1411
		SO_2			1589
		HCHO			460
4 Sep 2006	1250	NO_2	81	3.64	946
		SO2			1749
19 Sep 2006	1127	NO_2	47	10.78	4075
	1221		31	6.55	2817
	1512		38	4.26	2542
	1604		38	4.26	2402
		Texas City			
2 Sep 2006	1340	NO_2	99	1.51	186
	1405		105	2.23	250
14 Sep 2006	0950	NO_2	102	3.96	452
	1118		102	3.96	449
20 Sep 2006	1012	NO_2	67	6.16	567
	1059		67	6.16	634
	1310		77	4.9	404
	1425		93	3.72	375
	1506		93	3.72	499
	1619		93	3.72	644
	1634		93	3.72	596

daily measurements carried out during the field campaign is presented in Table 3.

3.1. NO_x Emissions

[25] Figure 2a shows the spatial distribution of differential NO_2 columns (color coded) quantified during a measurement conducted at the HSC on 31 August 2006 starting at 1037 LT. The known emission sources from the EI inside the HSC are shown as gray dots. Figure 2b shows the differential NO_2 columns quantified during the measurement. The traverse started at the northeast part of the HSC (black square in Figure 2a) and continued toward the west. Two main peaks were found during the traverse; the highest peak found at the southwest is thought to include most of the accumulated emissions of the HSC, while the second, smaller peak most likely represents emissions from the eastern part of the HSC. As discussed in section 2.2, the oxygen dimer (O_4) was included into the DOAS fit in order to indicate the presence of high aerosol loading, which could lead to enhanced light paths through multiple scattering. Figure 2h shows the differential O_4 columns quantified during the measurement where a stable behavior of the oxygen dimer during the traverse is evident, indicating no enhanced light paths during the traverse.

[26] From NO_2 emissions data reported in Table 3, it can be seen that differences in NO_2 emission rates were found at the HSC during the same day and among different days. On 31 August, NO_2 quantified emissions dropped by half comparing a traverse conducted at 1153 LT to traverses conducted previously during the same day.

[27] Figure 3a shows the spatial distribution of differential NO_2 columns (color coded) quantified during a measurement conducted at TC on 20 September 2006 starting at 1634 LT. The known NO_x emission sources of the TC area are shown as gray dots. Figure 3b shows the differential NO_2 columns quantified during the measurement. The traverse started at the north part of a highway located west of TC (black square in Figure 3a) and continued toward the southeast. A main peak was identified during the traverse, found at the western part of the TC industrial area. This peak is thought to represent one of the largest sources of NO_x in the area located at the western part. The other, smaller peaks most likely represent emissions from the whole TC area in general. Some differences were found in NO_2 quantified emissions at TC among different days (Table 3).

[28] The instrument used in this field campaign is capable of quantifying NO_2 but not NO_x, which is given in the inventories. Knowledge about the ratio NO_2/NO_x becomes important in order to assess the consistency of our measurements with the available inventories. Here we have used data from measurements conducted by the Piper Aztec aircraft flying above the same measurement paths we have used to quantify emissions from the HSC and TC industrial sites. Aircraft-based measurements indicate a NO_2/NO_x ratio of 0.74 for HSC and 0.73 for TC along the measurement paths we have used. Figure 4 shows recorded NO_2 and NO_x mixing ratios by the Piper Aztec aircraft while performing a vertical profile between 356 and 1265 m above mean sea level along the HSC on 31 August 2006 at 0800-0815 LT. As can be seen, most of the quantified NO_x is in the form of NO_2. For this field experiment, NO_x average emissions have been estimated from the original quantified total NO_2 values according to the NO_2/NO_x ratio derived by aircraft measurements: 0.74 for HSC and 0.73 for TC. This ratio was estimated for only 1 day for each industrial area; however, it was extrapolated to other measurement days, slightly adding uncertainty to our emission estimates of NO_x.

[29] In summary, large differences in quantified NO_2 emissions were found during and among different days of the field campaign. Our results show that NO_x-derived emissions from the HSC and TC industrial areas are 70%

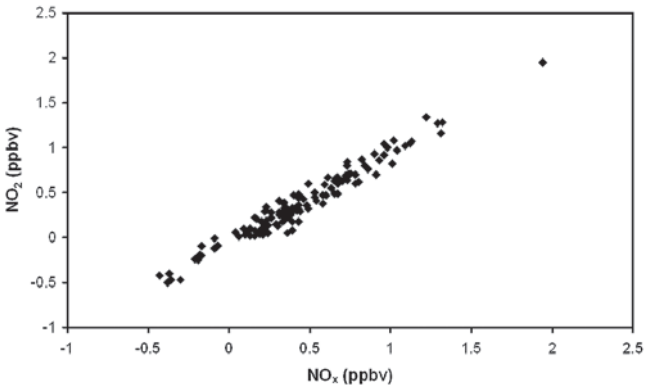

Figure 4. NO_2 and NO_x mixing ratios recorded by the Piper Aztec aircraft while performing a vertical profile between 356 and 1265 m above mean sea level along the Houston Ship Channel on 31 August 2006 at 0800–0815 LT.

and 43%, respectively, above the reported inventory values, with 33% uncertainty.

[30] A study conducted by *Williams et al.* [2009] during the TexAQS 2006 reveals that NO_x emissions from commercial marine shipping in the HGA are significant and present large variability (30%–40% relative standard deviation), which could explain NO_x emissions measured in excess in the HSC and probably to a lesser extent in TC, as well as the measured short-term variability in emissions found at the HSC during the field campaign.

3.2. SO_2 Emissions

[31] During the measurement period, SO_2 plumes were only successfully quantified in the HSC industrial area. Figure 2c shows the spatial distribution of differential SO_2 columns (color coded) quantified during a measurement conducted at the HSC on 31 August 2006 starting at 1037 LT. The known SO_2 emission sources from the EI inside the HSC are shown as gray dots. Figure 2d shows the differential SO_2 columns quantified during the measurement. The traverse started at the northeast part of the HSC (black square in Figure 2c) and continued toward the west. Two main SO_2 peaks were found during the traverse, coinciding with the previously discussed NO_2 peaks. As for the case of NO_2, the highest SO_2 peak found at the southwest is thought to include most of the accumulated emissions of the HSC, while the second, smaller peak most likely represents emissions from the eastern part of the HSC.

[32] Table 2 shows a comparison between measured SO_2 fluxes and reported values in the inventory. The reported daily emissions from the EI are also presented for comparison. In addition, a full summary of daily SO_2 measurements carried out during the field campaign is presented in Table 3. Table 2 indicates that the quantified SO_2 fluxes at the HSC industrial area were 34% higher than the emissions reported in the inventory, with a range of uncertainty, however, that encompasses the inventory.

3.3. HCHO Event

[33] On only 1 day during the field campaign was it possible to clearly identify the presence of HCHO in the plumes from the HGA. On 31 August 2006, HCHO was quantified during three consecutive measurements performed at the HSC industrial site between 0946 and 1245 LT (1446-1745 UTC). Figure 2e shows the spatial distribution of differential HCHO columns (color coded) quantified during a measurement conducted at the HSC on 31 August 2006 starting at 1037 LT. The known HCHO emission sources from the EI inside the HSC are shown as gray dots. Figure 2f shows the differential HCHO columns quantified during the measurement. The traverse started in the northeastern part of the HSC (black square in Figure 2e) and continued toward the west. As for the case of the NO_2 and SO_2 emissions measured during the same traverse, two main HCHO peaks were found during this traverse; the smaller peak found in the southeastern corner is thought to include the accumulated flux of the entire HSC, while the second, larger peak most likely represents the flux from the eastern part of the HSC where most of the HCHO sources are located.

[34] The three consecutive transects yielded a median flux of 481 kg h^{-1} with a MAD of 21 kg h^{-1}. From HCHO fluxes data reported in Table 3, it can be seen that the quantified HCHO fluxes during the three consecutive traverses give very similar values. The high HCHO quantified flux at the HSC is unexpected, especially when compared to the emissions inventory of 14 kg h^{-1} of HCHO for the HSC area (Table 2), representing primary emissions from the industries. It is important to note that only a small fraction of industrial facilities specify, in the data reported in the EI, the type of VOC emitted. In this case we have added all sources located inside the HSC that specifically report HCHO emissions; however, it is possible that some facilities have been missed because of the way of reporting HCHO as VOCs in general.

[35] During the morning flight of 31 August 2006, the Piper Aztec aircraft measured elevated mixing ratios of HCHO over the HSC. Figure 2g shows the spatial distribution of HCHO along the HSC measured by the Piper Aztec aircraft. The peak on the HCHO mixing ratio measured by the aircraft at the southern part of the HSC (Figure 2g) coincides with measurements reported in this study conducted by the mobile miniDOAS instrument.

[36] It is highly likely that the quantified HCHO in the HSC during this field observation was not directly emitted but rather was formed by oxidation of emitted VOCs. During this flight, the Piper Aztec aircraft also measured elevated mixing ratios of reactive alkenes at the southwestern part of the HSC [*Alvarez et al.*, 2007], coinciding with HCHO measurements reported in this study conducted by the mobile miniDOAS instrument. In addition, *Mellqvist et al.* [2007, 2010] measured large and highly variable emissions of propene, 200–2000 kg h^{-1}, on the same day and upwind of the location where the high formaldehyde differential columns were measured with the mobile miniDOAS instrument [*Mellqvist et al.*, 2007]. In addition, 31 August 2006 was characterized by low wind speeds (about 2 m s^{-1}), suggesting both more concentrated VOC levels and a longer photochemical processing time between the VOC emission and sampling time.

[37] We consider that the presence of HCHO in the HSC on 31 August 2006 is an isolated event rather than a permanent situation since it was only observed for a short period of time (3 h) and only once during 5 weeks of measurements conducted in the HGA. The occurrence of industrial emission events in the HGA has been previously identified and studied. They typically last hours to days and are largely made up of ethene and propene. Some events are reported to release a few hundred kilograms [*Murphy and Allen*, 2005], while others have been reported to lead to emission rates of up to several thousand kilograms per hour [*Vizuete et al.*, 2008]. More than half of the mass of highly reactive VOC emission events has been attributed to ethene and almost one third to propene; the remainder consists of isomers of butene and 1,3-butadiene [*Murphy and Allen*, 2005]. In this case, the HCHO quantified in the HSC cannot be regarded as an emission but rather as the photochemical production of HCHO by the oxidation of emitted alkenes, which tend to efficiently produce HCHO [*Dodge*, 1990; *Goldan et al.*, 2000; *Lee et al.*, 1998; *Wert et al.*, 2003].

[38] In addition, as part of the TexAQS 2006 field experiment, *Brooks et al.* [2009] report extreme pollution events in the early morning hours of 31 August 2006 during measurements conducted atop the Moody Tower

TexAQS II Radical Measurement Project site. Their findings include the highest fine particulate mercury value observed on 31 August 2006, along with extremely high values of VOCs, SO_2, aerosol mass, and most other primary pollutants. At 1430 UTC spikes in HCHO (23 ppb), PAN (3.6 ppb), and O_3 (~100 ppb) were reported as well. Back trajectories and wind direction showed air parcels coming from the Houston Ship Channel [*Brooks et al.*, 2009].

4. Conclusions

[39] In summary, measurements conducted during the TexAQS 2006 field experiment show that measured SO_2 emissions at HSC were 34% higher than the emissions reported in the inventory, with a range of uncertainty, however, that encompasses the inventory. The derived NO_x emissions at the HSC and TC industrial areas were 70% and 43%, respectively, above the reported inventory values, with 33% uncertainty. This should be compared to mobile solar infrared measurements and airborne measurements showing an order of magnitude difference in measured and reported ethene emissions from industrial sources in the HGA [*De Gouw et al.*, 2009]. Short-term variability of NO_x and SO_2 emissions were also found. On 31 August 2006, the measured emissions of NO_2 and SO_2 at the HSC dropped by half between a traverse conducted at 1153 LT when compared to traverses conducted previously during the same day.

[40] During the TexAQS 2006 field experiment, it was possible to identify a HCHO event occurring on 31 August 2006 yielding HCHO fluxes an order of magnitude greater than the reported primary emissions in the inventory. For this reason and due to the fact that during daytime, generally the amount of primary emitted HCHO is considerably smaller than the amount that is secondarily photochemically produced [*Wert et al.*, 2003], it is highly likely that the quantified HCHO in the HSC was formed by oxidation of emitted alkenes since these tend to efficiently produce HCHO, implying a very rapid photochemical conversion.

[41] **Acknowledgments.** Funding for this work was provided by Texas Environmental Research Consortium (TERC) under project H53. The authors would like to thank Craig Clements for conducting some of the GPS soundings and John Johansson for estimation of NO_2/NO_x ratios. We thank TCEQ for supplying wind profiler data. The Baylor Piper Aztec data were funded by TERC under project H63. We thank Levi Kauffman, Tim Compton, Grazia Zanin, Maxwell Shauck, and Martin Buhr for conducting part of the work with the Piper Aztec and Noor Gillani for flight planning.

References

Allen, D., C. Murphy, Y. Kimura, W. Vizuete, T. Edgar, H. Jeffries, B. Kim, M. Webster, and M. Symons (2004), Variable industrial VOC emissions and their impact on ozone formation in the Houston Galveston area: Final report on Texas Environmental Research Consortium project H-13, Univ. of Tex., Austin.

Alvarez, S., L. Kauffman, T. Compton, G. Zanin, M. Shauck, and M. Buhr (2007), H-63 aircraft measurements in support of TexAQS II: Project H63 final report, Tex. Environ. Res. Consortium, Houston.

Berkowitz, C. M., C. W. Spicer, and P. V. Doskey (2005), Hydrocarbon observations and ozone production rates in western Houston during the Texas 2000 Air Quality Study, *Atmos. Environ.*, *39*, 3383–3396, doi:10.1016/j.atmosenv.2004.12.007.

Bobrowski, N., and U. Platt (2007), SO_2/BrO rations studied in five volcanic plumes, *J. Volcanol. Geotherm. Res.*, *166*, 147–160, doi:10.1016/j.jvolgeores.2007.07.003.

Bobrowski, N., G. Hönninger, B. Galle, and U. Platt (2003), Detection of bromine monoxide in a volcanic plume, *Nature*, *423*, 273–276, doi:10.1038/nature01625.

Bogumil, K., et al. (2003), Measurements of molecular absorption spectra with the SCIAMACHY pre-flight model: Instrument characterization and reference data for atmospheric remote-sensing in the 230–2380 nm region, *J. Photochem. Photobiol. A Chem.*, *157*, 167–184, doi:10.1016/S1010-6030(03)00062-5.

Brock, C. A., et al. (2003), Particle growth in urban and industrial plumes in Texas, *J. Geophys. Res.*, *108*(D3), 4111, doi:10.1029/2002JD002746.

Brody, S. D., B. M. Peck, and W. E. Highfield (2004), Examining localized patterns of air quality perception in Texas: A spatial and statistical analysis, *Risk Anal.*, *24*, 1561–1574, doi:10.1111/j.0272-4332.2004.00550.x.

Brooks, S., W. Luke, M. Cohen, P. Kelly, B. Lefer, and B. Rappenglück (2009), Mercury species measured atop the Moody Tower TRAMP site, Houston Texas, *Atmos. Environ.*, doi:10.1016/j.atmosenv.2009.02.009.

Buzcu-Guven, B., and M. P. Fraser (2008), Comparison of VOC emissions inventory data with source apportionment results for Houston, TX, *Atmos. Environ.*, *42*, 5032–5043, doi:10.1016/j.atmosenv.2008.02.025.

Byun, D. W., S.-T. Kim, and S.-B. Kim (2007), Evaluation of air quality models for the simulation of a high ozone episode in the Houston metropolitan area, *Atmos. Environ.*, *41*, 837–853, doi:10.1016/j.atmosenv.2006.08.038.

Coheur, P.-F., S. Fally, M. Carleer, C. Clerbaux, R. Colin, A. Jenouvrier, M.-F. Mérienne, C. Hermans, and A. C. Vandaele (2002), New water vapor line parameters in the 26000–13000 cm^{-1} region, *J. Quant. Spectrosc. Radiat. Transfer. 74*, 493–510.

Conley, F. L., R. L. Thomas, and B. L. Wilson (2005), Measurement of volatile organic compounds in the urban atmosphere of Harris County, Texas, *J. Environ. Sci. Health.*, *40*, 1689–1699.

Crutzen, P. (1979), The role of NO and NO_2 in the chemistry of the troposphere and stratosphere, *Annu. Rev. Earth Planet. Sci.*, *7*, 443–472, doi:10.1146/annurev.ea.07.050179.002303.

Daum, P. H., L. I. Kleinman, S. R. Springston, L. J. Nunnermacker, Y.-N. Lee, J. Weinstein-Lloyd, J. Zheng, and C. M. Berkowitz (2003), A comparative study of O_3 formation in the Houston urban and industrial plumes during the 2000 Texas Air Quality Study, *J. Geophys. Res.*, *108*(D23), 4715, doi:10.1029/2003JD003552.

Daum, P. H., L. I. Kleinman, S. R. Springston, L. J. Nunnermacker, Y.-N. Lee, J. Weinstein-Lloyd, J. Zheng, and C. M. Berkowitz (2004), Origin and properties of plumes of high ozone observed during the Texas 2000 Air Quality Study (TexAQS 2000), *J. Geophys. Res.*, *109*, D17306, doi:10.1029/2003JD004311.

De Gouw, J. A., et al. (2009), Airborne measurements of ethene from industrial sources using laser photo-acoustic spectroscopy, *Environ. Sci. Technol.*, *43*, 2437–2442, doi:10.1021/es802701a.

Dodge, M. C. (1990), Formaldehyde production in photochemical smog as predicted by three state-of-the-science chemical oxidant mechanisms, *J. Geophys. Res.*, *95*, 3635–3648, doi:10.1029/JD095iD04p03635.

Fally, S., P.-F. Coheur, M. Carleer, C. Clerbaux, R. Colin, A. Jenouvrier, M.-F. Mérienne, C. Hermans, and A. C. Vandaele (2003), Water vapor line broadening and shifting by air in the 26,000–13,000 cm^{-1} region, *J. Quant. Spectrosc. Radiat. Transf.*, *82*, 119–131.

Finlayson-Pitts, B. J., and J. N. Pitts (2000), *Chemistry of the Upper and Lower Atmosphere: Theory, Experiments and Applications*, Academic, San Diego, Calif.

Galle, B., C. Oppenheimer, A. Geyer, A. J. S. McGonigle, M. Edmonds, and L. Horrocks (2002), A miniaturised ultraviolet spectrometer for remote sensing of SO_2 fluxes: A new tool for volcano surveillance, *J. Volcanol. Geotherm. Res.*, *119*, 241–254, doi:10.1016/S0377-0273(02)00356-6.

Garcia, A. R., R. Volkamer, L. T. Molina, M. J. Molina, J. Samuelsson, J. Mellqvist, B. Galle, S. C. Herndon, and C. E. Kolb (2006), Separation of emitted and photochemical formaldehyde in Mexico City using a statistical analysis and a new pair of gas-phase tracers, *Atmos. Chem. Phys.*, *6*, 4545–4557.

Gilman, J. B., et al. (2009), Measurements of volatile organic compounds during the 2006 TexAQS/GoMACCS campaign: Industrial influences, regional characteristics, and diurnal dependencies of the OH reactivity, *J. Geophys. Res.*, *114*, D00F06, doi:10.1029/2008JD011525.

Goldan, P. D., D. D. Parrish, W. C. Kuster, M. Trainer, S. A. McKeen, J. Holloway, B. T. Jobson, D. T. Sueper, and F. C. Fehsenfeld (2000), Airborne measurements of isoprene, CO, and anthropogenic hydrocarbons and their implications, *J. Geophys. Res.*, *105*, 9091–9105, doi:10.1029/1999JD900429.

Grover, R., and M. L. Bradford (2001), Texas NO_x state implementation plan for Houston-Galveston area, *Environ. Prog.*, *20*, 197–205, doi:10.1002/ep.670200407.

Hermans, C., A. C. Vandaele, M. Carleer, S. Fally, R. Colin, A. Jenouvrier, B. Coquart, and M.-F. Mérienne (1999), Absorption cross-sections of atmospheric constituents: NO_2, O_2, and H_2O, *Environ. Sci. Pollut. Res.*, *6*, 151–158, doi:10.1007/BF02987620.

Jacob, D. J., et al. (1996), Origin of ozone and NO_x in the tropical troposphere: A photochemical analysis of aircraft observations over the South Atlantic basin, *J. Geophys. Res.*, *101*, 24,235–24,250, doi:10.1029/96JD00336.

Jobson, B. T., C. M. Berkowitz, W. C. Kuster, P. D. Goldan, E. J. Williams, F. C. Fehsenfeld, E. C. Apel, T. Karl, W. A. Lonneman, and D. Riemer (2004), Hydrocarbon source signatures in Houston, Texas: Influence of the petrochemical industry, *J. Geophys. Res.*, *109*, D24305, doi:10.1029/2004JD004887.

Johansson, M., and Y. Zhang (2004), Mobile DOAS, version 4.1, Opt. Remote Sens. Group Chalmers Univ. of Technol., Göteborg, Sweden.

Johansson, M., B. Galle, T. Yu, L. Tang, D. Chen, H. Li, J. X. Li, and Y. Zhang (2008), Quantification of total emission of air pollutants from Beijing using mobile mini-DOAS, *Atmos. Environ.*, *42*, 6926–6933, doi:10.1016/j.atmosenv.2008.05.025.

Johansson, M., C. Rivera, B. de Foy, W. Lei, J. Song, Y. Zhang, B. Galle, and L. Molina (2009), Mobile mini-DOAS measurement of the outflow of NO_2 and HCHO from Mexico City, *Atmos. Chem. Phys.*, *9*, 5647–5653.

Kasibhatla, P. S., H. Levy, W. J. Moxim, and W. L. Chameides (1991), The relative impact of stratospheric photochemical production on tropospheric NO_y levels: A model study, *J. Geophys. Res.*, *96*, 18,631–18,646, doi:10.1029/91JD01665.

Kleinman, L. I., P. H. Daum, D. Imre, Y. N. Lee, L. J. Nunnermacker, S. R. Springston, J. Weinstein-Lloyd, and J. Rudolph (2002), Ozone production rate and hydrocarbon reactivity in 5 urban areas: A cause of high ozone concentration in Houston, *Geophys. Res. Lett.*, *29*(10), 1467, doi:10.1029/2001GL014569.

Kley, D., and M. McFarland (1980), Chemiluminescence detector for NO and NO_2, *Atmos. Technol.*, *12*, 63–69.

Kraus, S. (2003), DOAIS intelligent system, Inst. of Environ. Phys. Univ. of Heidelberg, Germany.

Lee, Y.-N., et al. (1998), Atmospheric chemistry and distribution of formaldehyde and several multioxygenated carbonyl compounds during the 1995 Nashville/Middle Tennessee Ozone Study, *J. Geophys. Res.*, *103*, 22,449–22,462, doi:10.1029/98JD01251.

Lei, W., R. Zhang, X. Tie, and P. Hess (2004), Chemical characterization of ozone formation in the Houston-Galveston area: A chemical transport model study, *J. Geophys. Res.*, *109*, D12301, doi:10.1029/2003JD004219.

Leuchner, M., and B. Rappenglück (2010), VOC source-receptor relationships in Houston during TexAQS-II, *Atmos. Environ.*, in press.

Martin, R. V., et al. (2002), An improved retrieval of tropospheric nitrogen dioxide from GOME, *J. Geophys. Res.*, *107*(D20), 4437, doi:10.1029/2001JD001027.

McGonigle, A. J. S., C. L. Thomson, V. I. Tsanev, and C. Oppenheimer (2004), A simple technique for measuring power station SO_2 and NO_2 emissions, *Atmos. Environ.*, *38*, 21–25, doi:10.1016/j.atmosenv.2003.09.048.

Meller, R., and G. K. Moortgat (2000), Temperature dependence of the absorption cross sections of formaldehyde between 223 and 323 K in the wavelength range 225–375 nm, *J. Geophys. Res.*, *105*, 7089–7101, doi:10.1029/1999JD901074.

Mellqvist, J., J. Samuelsson, C. Rivera, B. Lefer, and M. Patel (2007), Measurements of industrial emissions of VOCs, NH_3, NO_2 and SO_2 in Texas using the solar occultation flux method and mobile DOAS: Project H053.2005, Tex. Environ. Res. Consortium, Houston.

Mellqvist, J., J. Samuelsson, J. Johanssson, C. Rivera, B. Lefer, S. Alvarez, and J. Jolly (2010), Measurements of industrial emissions of alkenes in Texas using the solar occultation flux method, *J. Geophys. Res.*, *115*, D00F17, doi:10.1029/2008JD011682.

Millán, M. M. (1980), Remote sensing of air pollutants. A study of some atmospheric scattering effects, *Atmos. Environ.*, *14*, 1241–1253, doi:10.1016/0004-6981(80)90226-7.

Moffat, A. J., and M. M. Millán (1971), The application of optical correlation techniques to the remote sensing of SO_2 plumes using skylight, *Atmos. Environ.*, *5*, 677–690, doi:10.1016/0004-6981(71)90125-9.

Mori, T., T. Mori, K. Kazahaya, M. Ohwada, J. Hirabayashi, and S. Yoshikawa (2006), Effect of UV scattering on SO_2 emission rate measurements, *Geophys. Res. Lett.*, *33*, L17315, doi:10.1029/2006GL026285.

Murphy, C. F., and D. T. Allen (2005), Hydrocarbon emissions from industrial release events in the Houston-Galveston area and their impact on ozone formation, *Atmos. Environ.*, *39*, 3785–3798, doi:10.1016/j.atmosenv.2005.02.051.

Murphy, D., D. Fahey, M. Proffitt, S. Liu, C. Eubank, S. Kawa, and K. Kelly (1993), Reactive odd nitrogen and its correlation with ozone in the lower stratosphere and upper troposphere, *J. Geophys. Res.*, *98*, 8751–8773, doi:10.1029/92JD00681.

Penner, J. E., C. S. Atherton, J. Dignon, S. J. Ghan, J. J. Walton, and S. Hameed (1991), Tropospheric nitrogen: A three-dimensional study of sources, distributions, and deposition, *J. Geophys. Res.*, *96*, 959–990, doi:10.1029/90JD02228.

Platt, U. (1994), Differential optical absorption spectroscopy (DOAS), in *Air Monitoring by Spectroscopy Techniques*, edited by M. W. Sigrist, pp. 27–83, Wiley-Interscience, New York.

Platt, U., and J. Stutz (2008), *Differential Optical Absorption Spectroscopy: Principles and Applications (Physics of Earth and Space Environments)*, Springer, Berlin, Germany.

Platt, U., D. Perner, and H. W. Pätz (1979), Simultaneous measurement of atmospheric CH_2O, O_3 and NO_2 by differential optical absorption, *J. Geophys. Res.*, *84*, 6329–6335, doi:10.1029/JC084iC10p06329.

Rivera, C., J. A. Garcia, B. Galle, L. Alonso, Y. Zhang, M. Johansson, M. Matabuena, and G. Gangoiti (2009), Validation of optical remote sensing measurement strategies applied to industrial gas emissions, *Int. J. Remote Sens.*, *30*, 3191–3204, doi:10.1080/01431160802558808.

Ryerson, T. B., et al. (2003), Effect of petrochemical industrial emissions of reactive alkenes and NO_x on tropospheric ozone formation in Houston, Texas, *J. Geophys. Res.*, *108*(D8), 4249, doi:10.1029/2002JD003070.

Sinreich, R., U. Friess, T. Wagner, and U. Platt (2005), Multi axis differential optical absorption spectroscopy (MAX-DOAS) of gas and aerosol distributions, *Faraday Discuss.*, *130*, 153–164, doi:10.1039/b419274p.

Smith, L. A., T. H. Stock, K. C. Chung, S. Mukerjee, X. L. Liao, C. Stallings, and M. Afshar (2007), Spatial analysis of volatile organic compounds from a community-based air toxics monitoring network in Deer Park, Texas, USA, *Environ. Monit. Assess.*, *128*, 369–379, doi:10.1007/s10661-006-9320-8.

Tucker, S. C., W. A. Brewer, R. M. Banta, C. J. Senff, S. P. Sandberg, D. C. Law, A. Weickmann, and R. M. Hardesty (2009), Doppler lidar estimation of mixing height using turbulence, shear, and aerosol profiles, *J. Atmos. Oceanic Technol.*, *26*, 673–688, doi:10.1175/2008JTECHA1157.1.

Vandaele, A. C., C. Hermans, P. C. Simon, M. Carleer, R. Colin, S. Fally, M. F. Mérienne, A. Jenouvrier, and B. Coquart (1998), Measurements of the NO_2 absorption cross-section from 42 000 cm^{-1} to 10 000 cm^{-1} (238–1000 nm) at 220 K and 294 K, *J. Quant. Spectrosc. Radiat. Transf.*, *59*, 171–184, doi:10.1016/S0022-4073(97)00168-4.

Van Roozendael, M., and C. Fayt (2001), WinDOAS, version 2.1, Belg. Inst. For Space Aeronomy, Uccle.

Vizuete, W., B.-U. Kim, H. Jeffries, Y. Kimura, D. T. Allen, M.-A. Kioumourtzoglou, L. Biton, and B. Henderson (2008), Modeling ozone formation from industrial emission events in Houston, Texas, *Atmos. Environ.*, *42*, 7641–7650, doi:10.1016/j.atmosenv.2008.05.063.

Voigt, S., J. Orphal, K. Bogumil, and J. P. Burrows (2001), The temperature dependence (203–293 K) of the absorption cross sections of O_3 in the 230–850 nm region measured by Fourier-transform spectroscopy, *J. Photochem. Photobiol. A Chem.*, *143*, 1–9, doi:10.1016/S1010-6030(01)00480-4.

Wert, B. P., et al. (2003), Signatures of terminal alkene oxidation in airborne formaldehyde measurements during TexAQS 2000, *J. Geophys. Res.*, *108*(D3), 4104, doi:10.1029/2002JD002502.

Williams, E. J., B. M. Lerner, P. C. Murphy, S. C. Herndon, and M. S. Zahniser (2009), Emissions of NO_x, SO_2, CO, and HCHO from commercial marine shipping during Texas Air Quality Study (TexAQS) 2006, *J. Geophys. Res.*, *114*, D21306, doi:10.1029/2009JD012094.

Xie, Y., and C. M. Berkowitz (2007), The use of conditional probability functions and potential source contribution functions to identify source regions and advection pathways of hydrocarbon emissions in Houston, Texas, *Atmos. Environ.*, *41*, 5831–5847, doi:10.1016/j.atmosenv.2007.03.049.

S. Alvarez, Institute for Air Science, Baylor University, Waco, TX 76798, USA.

B. Lefer and M. R. Patel, Department of Geosciences, University of Houston, Houston, TX 77004, USA.

J. Mellqvist, C. Rivera, and J. Samuelsson, Radio and Space Science, Chalmers University of Technology, SE-412 96 Gothenburg, Sweden. (claudia.rivera@chalmers.se)

CHARACTERIZING TRAILING WAVES FROM CARGO SHIP WAKE

Kevin Haas, Georgia Institute of Technology, khaas@gatech.edu
Alexandra Muscalus, Georgia Institute of Technology, amuscalus@gatech.edu

INTRODUCTION

Low-frequency (LF) cargo ship wake is a major source of hydrodynamic energy in shipping channels, where it has increasingly been linked to shoreline erosion. The LF wake consists of a drawdown called the "Bernoulli depression," a return surge, and finally a series of trailing waves that may persist longer than 30 minutes after the vessel passage (Figure 1). While the Bernoulli depression and surge are well-explained by conservation principles, we presently lack a robust explanation of the trailing waves. They are a ubiquitous feature observed at many locations (e.g. Garrel, Lopez, and Collins, 2008), and have frequently been attributed to cross-channel seiching; however, field measurements from the Savannah River, GA, USA suggested that some of the waves may have alongshore progressive characteristics, which contradicts this assumption.

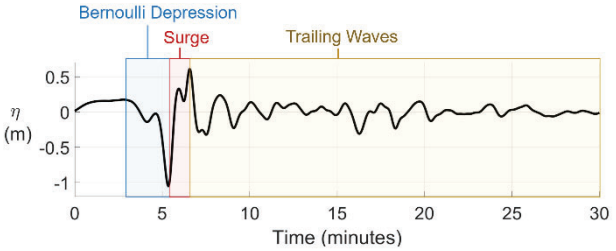

Figure 1 – A sample field measurement of low-frequency cargo ship wake showing the Bernoulli depression, surge, and trailing waves.

Over 500 large vessel wake events were measured with current profilers and pressure transducers in a previous study investigating the source of erosion at Bird/Long Island in the Savannah River, Georgia, USA (Haas and Muscalus, 2019). The island divides the river into two channels, the larger of which – the "Main Channel" - contains a shipping channel with about 5,000 annual cargo ship transits. Measurements on the shelf of the Main Channel along Bird/Long Island revealed that the low-frequency (LF) component of vessel wake is the dominant energy source; its contribution is much stronger than that of tidal currents, wind waves, and Kelvin waves. While the primary wave is the most energetic wave in the LF wake system, the trailing wave system contains on average 40% of the total LF wake energy. Therefore, it is imperative to gain a better understanding of trailing wave characteristics and their generation mechanisms.

CHARACTERIZING TRAILING WAVES IN THE FIELD

In order to characterize the trailing waves, two different field experiments with alongshore arrays of pressure transducers were completed. Within the Savannah River along Bird/Long Island, an alongshore array spanning 290 m with seven variably spaced instruments was deployed in approximately 3 m mean water depth in February 2022, and an alongshore array spanning 240 m with six variably spaced instruments was deployed in a little over 2 m mean depth for several days each (Figure 2). In addition, the channel bathymetry was surveyed along the full island. In February, 37 cargo ship passages and in June 42 cargo ship passages were captured with both inbound and outbound vessels. Figure 3 below shows the occurrence rate of the speed and length of the vessels for the two time periods. Both months had vessels with similar lengths ranging from 100 to 400 m long; however, the February data set had more vessels traversing the channel at higher speeds. While a range of vessel speeds were observed, from 4.5 to over 8 m/s, all depth Froude numbers for the vessels remained well within the subcritical range.

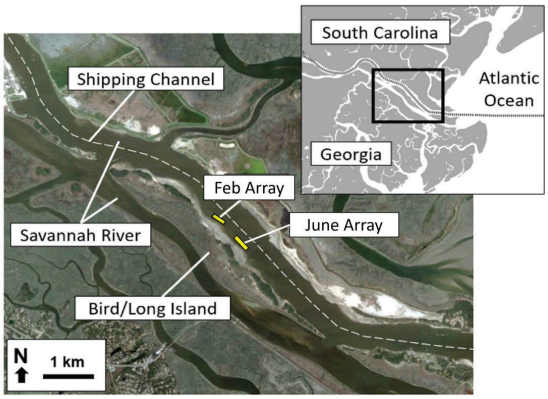

Figure 2 – Map of the location for the seven-instrument (Feb) and six-instrument (June) alongshore arrays near Bird/Long Island in the Savannah River, Georgia, USA.

Figure 4 shows an example time series from an outbound vessel (Cosco Excellence) on June 9, 2022. The 366 m long vessel was traveling approximately 6 m/s when it passed the longshore array around 22:35. The first wave is the Bernoulli depression which is attached to the passing vessel. This event had a large depression around 0.9 m. The progressive nature of this first wave is clearly observed from the time lags as the wave passes through the array starting at PT 1. The second wave, which is the first trailing wave, although much smaller in amplitude also demonstrate progressive behavior in the same direction. However, from the second trailing wave (wave 3) onwards, the characteristics become much more complicated as there are even indications of progressive motion in the opposite direction.

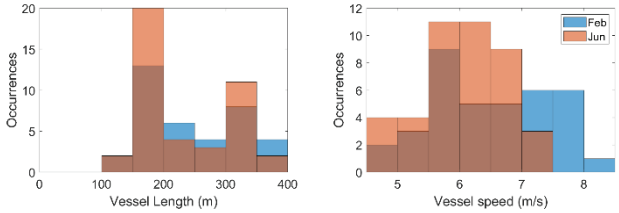

Figure 3 – Histograms of the vessel length (left) and vessel speed (right) from the February and June data sets.

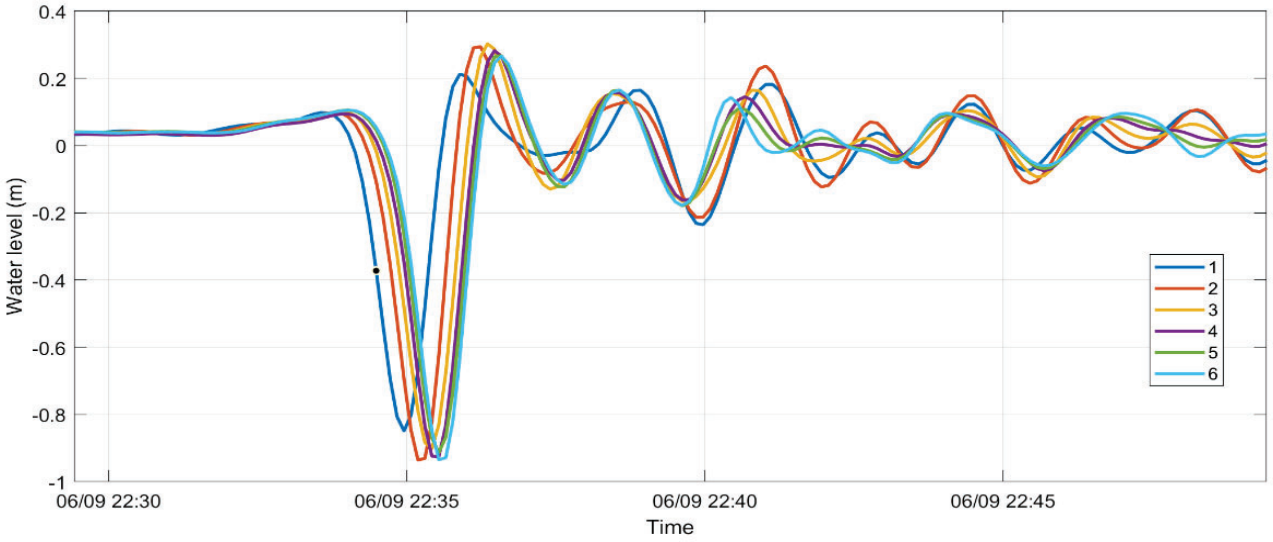

Figure 4 – Time series of the mid-band-pass filtered water level data from each instrument within the longshore array of the Cosco Excellence (366 m long) traveling outbound on June 9, 2022 passing the array around 22:35 moving with an absolute speed about 6 m/s.

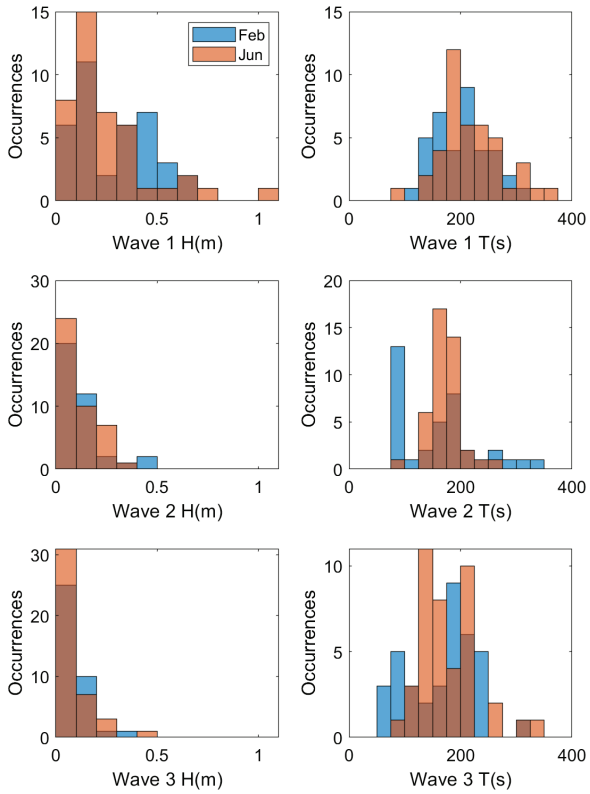

Figure 5 – Histograms of the observed wave height (left column) and period (right column) for the primary "wave 1" (1st row) and the first two trailing waves, "wave 2" and "wave 3" (2nd and 3rd rows, respectively) from the February and June data sets.

The wave heights and periods for the first three waves are computed for each vessel passage and are used to compute the histograms shown in Figure 5. Despite having slower vessels, the June dataset included the largest observed primary wave heights, perhaps from wave shoaling due to that array being in shallower water. The trailing wave heights become decreasingly smaller for both data sets. The periods cover a broad range of values from 100 to nearly 400 s. The primary wave tends to have a longer period than the trailing waves. Interestingly, the first trailing wave tends to have a narrower range of periods than the third wave.

These data sets are going to be further used to analyze the specific characteristics of the trailing waves, in order to determine the presence of progressive and/or standing waves and attribute their generation to the properties of the vessels that created them.

MODELING TRAILING WAVES WITH FUNWAVE-TVD

Cargo ship passages have been simulated with a simplified channel bathymetry in FUNWAVE-TVD, a 2D Boussinesq model. The model simulates the vessel as a pressure source with the same dimensions and speed as a typical cargo ship observed in the field. These initial runs generated trailing waves, which spectral analysis confirmed to be edge waves trapped on the shelf of the channel. Additional suites of simulations were also run with independently varying beach slopes and ship speeds to isolate the effects of these parameters on trailing wave characteristics and confirmed the adherence of the trailing waves to edge wave dispersion.

However, to understand the effect of the more complicated bathymetry and to see if edge waves are still generated, additional simulations will be completed using representative channel cross-sections as measured from the bathymetric survey. These simulations will still utilize a long straight channel, but with a more realistic cross-

section. Finally, simulations of vessel passages using the true bathymetry accounting for the along-channel variability will be completed to fully resolve the impact this has on the trailing wave generation and characteristics.

REFERENCES

Garel, Lopez, and Collins (2008): Sediment resuspension events induced by the wake wash of deep-draft vessels, Geo-Marine Letters, vol. 28, issue 4, pp. 215-211.

Haas and Muscalus (2019): Bird-Long Island Management Study Phase 1B: Hydrodynamic Characterizations for Bird/Long Island. No, FHWA-GA-19-1634. Georgia Department of Transportation.

Ocean and Coastal Management 182 (2019) 104945

Contents lists available at ScienceDirect

Ocean and Coastal Management

journal homepage: www.elsevier.com/locate/ocecoaman

Defining boat wake impacts on shoreline stability toward management and policy solutions

Donna Marie Bilkovic[a,*], Molly M. Mitchell[a], Jennifer Davis[b], Julie Herman[a], Elizabeth Andrews[c], Angela King[c], Pamela Mason[a], Navid Tahvildari[d], Jana Davis[e], Rachel L. Dixon[a,f]

[a] Virginia Institute of Marine Science, William & Mary, PO Box 1346, Gloucester Pt, VA, 23062, USA
[b] NOAA - National Centers for Coastal Ocean Science, 101 Pivers Island Rd, Beaufort, NC, 28516, USA
[c] Virginia Coastal Policy Center, William & Mary Law School, PO Box 8795, Williamsburg, VA, 23187, USA
[d] Department of Civil and Environmental Engineering, Old Dominion University, Norfolk, VA, 23529, USA
[e] Chesapeake Bay Trust, 60 West Street, Annapolis, MD, 21401, USA
[f] Chesapeake Research Consortium, 645 Contees Wharf Road, Edgewater, MD, 21037, USA

ARTICLE INFO

Keywords:
Erosion
Ships
Turbidity
Waves
Wetlands

ABSTRACT

Coastal economies are often supported by activities that rely on commercial or recreational vessels to move people or goods, such as shipping, transportation, cruising, and fishing. Unintentionally, frequent or intense vessel traffic can contribute to erosion of coastlines; this can be particularly evident in sheltered systems where shoreline erosion should be minimal in the absence of boat waves. We reviewed the state of the science of known effects of boat waves on shoreline stability, examined data on erosion, turbidity, and shoreline armoring patterns for evidence of a response to boat waves in Chesapeake Bay, and reviewed existing management and policy actions in Chesapeake Bay and nearby states to make recommendations for actions to minimize boat wake impacts. In the literature, as well as in our analyses, boat wake energy may be linked to elevated turbidity and shoreline erosion, particularly in narrow waterways. In Chesapeake Bay, three lines of evidence suggest boat waves are contributing to shoreline erosion and poor water clarity in some Bay creeks and tributaries: 1) nearshore turbidity was elevated in many waterways during periods of expected high boating activity, 2) armoring was placed along about a quarter of the low energy shorelines of three examined tidal creeks that are exposed to relatively high boating pressure, and 3) 15% of the shorelines we examined throughout the Bay (9000 km) are low energy shorelines that are experiencing high erosion ($\geq$0.3 m/yr) that cannot be attributed to wind wave energy. Still, there remain significant data gaps that preclude the determination of the overall contribution of boat waves to shoreline erosion throughout the Bay, notably, shoreline erosion data in low energy waterways, recreational boating traffic patterns, and nearshore bathymetry. Interim protective measures can be (and have been) applied in high risk waterways, such as small, low energy waterways that have high recreational boating activity, to help reduce shoreline erosion. Policy options used in Bay states and elsewhere include setbacks from the shore, wake restrictions, and speed restrictions; other more restrictive policies may include prohibition on boats of a certain size or limiting the number of passages. Finally, a systems-approach to boat wake impact management using uniform boat wake policies is likely to be the most effective for consistent shoreline protection.

1. Introduction

Human pressures in coastal systems are extensive as a large proportion of the global population inhabits these areas and utilizes the natural resources they provide (McGranahan et al., 2007). The magnitude of some human impacts are well understood, such as those caused by land development and occupation along the coastline. The magnitude of other impacts are poorly quantified, such as the implications of the intensive vessel traffic that supports our maritime and recreational pursuits. Commercial and recreational boating activities

* Corresponding author.
E-mail addresses: donnab@vims.edu (D.M. Bilkovic), molly@vims.edu (M.M. Mitchell), jenny.davis@noaa.gov (J. Davis), herman@vims.edu (J. Herman), eaadrews@wm.edu (E. Andrews), amking02@wm.edu (A. King), mason@vims.edu (P. Mason), ntahvild@odu.edu (N. Tahvildari), jdavis@cbtrust.org (J. Davis), rldixon@vims.edu (R.L. Dixon).

https://doi.org/10.1016/j.ocecoaman.2019.104945
Received 12 December 2018; Received in revised form 20 August 2019; Accepted 1 September 2019
Available online 10 September 2019

are often prominent contributors to a coastal economy, resulting in intensive and frequent vessel traffic. This is especially true when the region is a major route for shipping, transportation, and/or cruise industries. In 2013, the Ocean Economy for U.S. coastal states comprised about 2.2% of both U.S. GDP and employment, a larger share of the U.S. economy than other major natural resource industries, including farming, food products, oil and gas extraction, and forest products. Marine Transportation, the movement of people and goods across oceans and Great Lakes, generated $59 billion in annual total GDP (Kildow et al., 2016). As coastal communities continue to struggle to address rapidly eroding shorelines and increasing nearshore turbidity, more attention has been given to the contribution of boat-generated waves to these issues.

In general, boat wakes have been shown to erode shorelines (e.g., Castillo et al., 2000; Bauer et al., 2002), scour the bottom of the shoreface, and decrease water clarity through turbulence (e.g., U. S. Army Corps of Engineers (USACE) 1994; Asplund 1996). Boat wakes negatively affect coastal systems through two general processes – turbulence and bank erosion. Turbulence causes elevated suspended sediment concentrations which can lead to degraded oyster reefs, light-limitation of submerged aquatic vegetation, and can alter prey resources for fish (e.g., Liddle and Scorgie, 1980; Grizzle et al., 2002; Koch, 2002; Koch et al., 2006; Hallac et al., 2012; Whitfield and Becker, 2014; Campbell, 2015). Bank erosion can cause undercutting, marsh loss or degradation, and disturbance to faunal communities (Parnell and Koefoed-Hansen, 2001).

Boat wake energy is event-dependent and influenced by vessel length, water depth, and boat speed (Sorensen, 1973; Glamore, 2008). While each boat passage generates a complex series of waves with unique characteristics, wake wave height can be reasonably predicted by vessel speed (Sorenson, 1973; Zabawa and Ostrom, 1980; Fonseca and Malhotra, 2012). Wakes tend to be most harmful in shallow and narrow waterways where wake energy has limited ability to dissipate with distance from the vessel. Published values of wave decay after boat passage indicate that even small (16 ft) recreational vessels traveling within 150 m (~500 ft) of shore are capable of producing erosion – causing waves (Sorenson, 1973; Zabawa and Ostrum, 1980). Although periodic in comparison to wind waves, boat wakes may be the primary source of erosion in areas with low wind wave energy due to their greater heights and longer periods. For example, on the Savannah River, boat wake energy contributes less than 5% of the total wave energy, yet it accounts for 30% of the wave force impacting shorelines (Houser, 2010). Adding to the complexity, the relative amount of wave energy attributable to boats versus wind may vary temporally because the intensity of boating activity may vary throughout the year (Zabawa and Ostrom, 1980; Maynord et al., 2008). The frequency of vessel passage influences the overall amount of boat wake energy impacting a given shoreline, with highly traveled waterways more likely to experience boat wake-induced shoreline erosion than those that are less frequently traveled (Zabawa and Ostrom, 1980; Glamore, 2008).

Waves can be attenuated by shoreline vegetation in certain settings; however, frequent exposure to boat wakes may limit the capacity of these shorelines to mitigate erosion. Vegetated marsh shorelines can erode when regularly exposed to 10 cm waves (Coops et al., 1996); when waves are greater than 30 cm for as little of 5% of the time, marsh survival was shown to be compromised in the Gulf of Mexico (Schafer et al., 2003; Roland and Douglas, 2005). Therefore, even infrequent wake impacts may lead to erosion and habitat loss. Several studies in coastal systems have examined the relationship among wave heights, vessel speed, and distance offshore for a variety of typical vessel types and sizes. Generally, for speed ranges of 11–50 km/h within 150 m from shore, maximum wave heights between 10 and 50 cm occurred, suggesting erosion is likely in most cases (Table 1).

The Chesapeake Bay is a major maritime center along the Eastern Seaboard that supports a myriad of marine transportation sectors including military, cargo, transportation, cruise, fisheries, and recreational boating. There are several major ports, most notably, Baltimore and Port of Virginia (includes Norfolk, Portsmouth, Newport News) which handle significant cargo tonnage. There is a large military presence in the Chesapeake Bay, including the Navy, Coast Guard, and Marines Joint Forces, as well as major ship building industries that make use of Chesapeake Bay waterways. In addition to commercial traffic, there are at least 500,000 registered recreational vessels in the Chesapeake Bay (Virginia Department of Game and Inland Fisheries, data from 1997 to 2012; Environmental Finance Center, University of Maryland, 2013). Boating activity has intensified with increasing Bay populations and improved access to waterways from the growing number of private and public piers. Recreational boating can be most concerning for shoreline erosion because of the ability of these small (or shallow-draft) vessels to pass frequently near the shores, often at high speeds.

Table 1
Measured wave heights at varying vessel speeds and distances extracted from Zabawa and Ostrum (1980) for Chesapeake Bay and Sorenson, 1973 for Oakland Estuary, CA. Wave heights of 0.3 m or less have been shown to erode vegetated shores or compromise marsh survival (Coops et al., 1996; Schafer et al., 2003; Roland and Douglas, 2005). Table modified from Bilkovic et al., (2017). * indicates planing hull, ** indicates displacement hull.

Boat type	Distance from sailing line (m)	Speed of boat travel (knots ((km hr^{-1}))	Max wave height (m)
26' (8 m) Recreational boat: Uniflight*	100	10 (19)	0.41
	100	26 (48)	0.29
	150	10 (19)	0.37
	150	27 (50)	0.21
16' (5 m) Recreational boat: Boston Whaler*	50	10 (19)	0.22
	50	24 (44)	0.13
	150	12 (22)	0.14
	150	27 (50)	0.07
45' (14 m) Commercial boat: Tugboat**	30	6 (11)	0.2
	30	10 (19)	0.5
	150	6 (11)	0.1
	150	10 (19)	0.3
263' (80 m) Commercial boat: Barge**	150	10 (19)	0.2
	300	10 (19)	0.1

The Chesapeake Bay region has experienced extensive development over the course of hundreds of years, currently supporting about 18 million inhabitants, which has caused eutrophication, hypoxia, and coastal habitat and species loss. In response to growing pollution issues, the Chesapeake Bay Program (CBP) - a partnership between the states of Maryland, Virginia, Pennsylvania, New York, West Virginia, Delaware, the District of Columbia, federal agencies (represented by the U.S. EPA), and the Chesapeake Bay Commission - was formed in 1983 to guide restoration of the Bay. The Chesapeake Watershed Agreement (2014) designates a series of goals including habitat (tidal marsh, submerged aquatic vegetation) and water quality restoration that could be adversely affected by boat wave-induced erosion. Other Bay Agreement goals may inadvertently exacerbate the issue, such as the goal to increase public access to the Bay waterways.

Here, we: (1) evaluate existing and new data for evidence of enhanced turbidity, high erosion, or enhanced shoreline armoring in response to boat-generated waves in Chesapeake Bay and identify data gaps, and (2) review existing management and policy actions in Chesapeake Bay states and make recommendations for actions to help minimize potential boat wake impacts.

2. Methods

Comprehensive information on boating activity and shore erosion driven by boat wakes is not available for Chesapeake Bay. However,

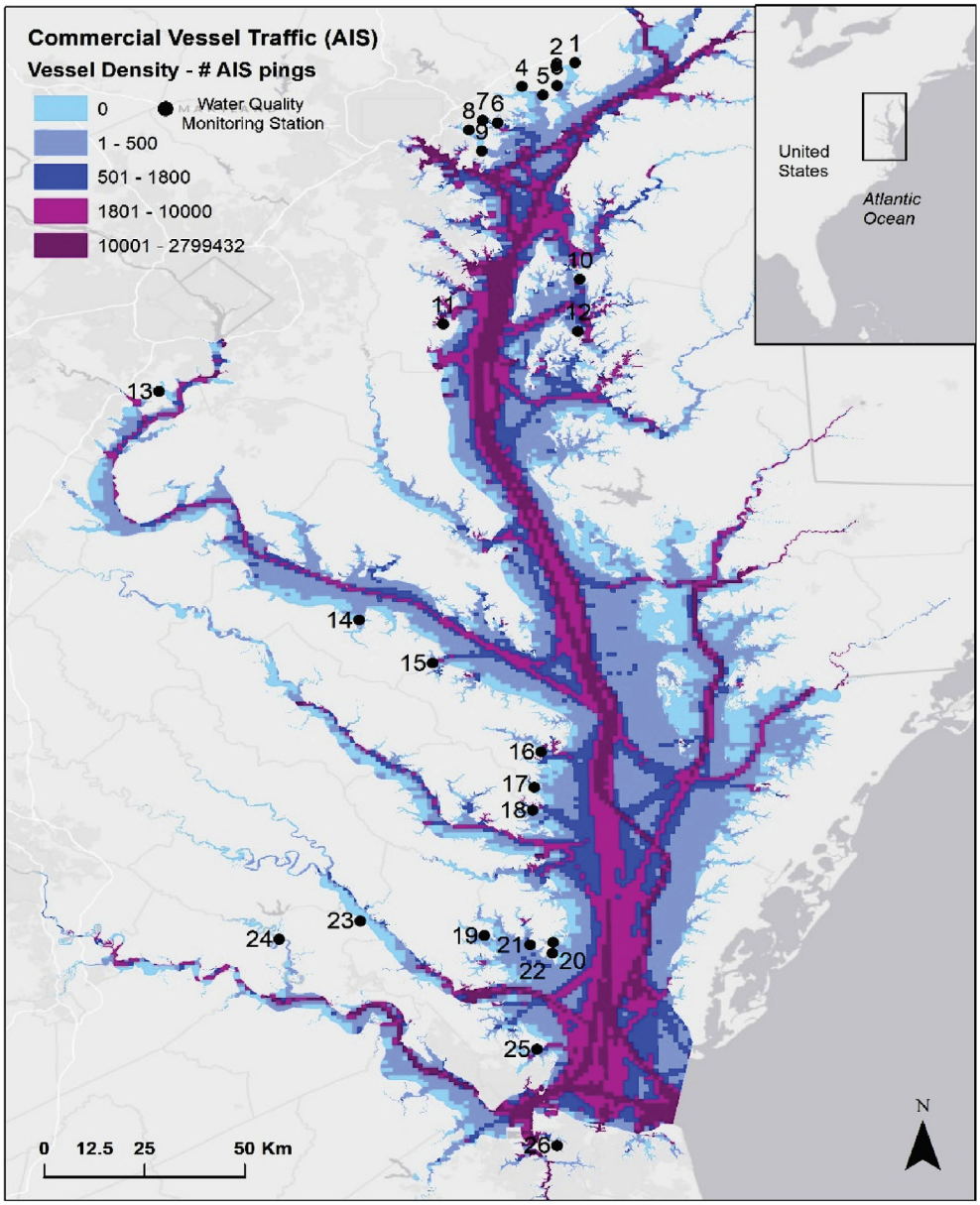

Fig. 1. Distribution of long-term water quality monitoring stations in relation to commercial vessel traffic patterns in Chesapeake Bay. Figure modified from Bilkovic et al., (2017).

surrogate measures can be useful as indicators of the potential for boating to be contributing to shore erosion. Using existing data from Chesapeake Bay, we examined *1)* the relationship between recreational boating activity and nearshore turbidity; *2)* the occurrence of high erosion along shorelines with low wind energy (small fetch), and; *3)* the occurrence of shoreline armoring along shorelines with low wind energy. We acknowledge the limitations in these analyses because the data used were not collected to specifically address boat wake impacts; however, our objectives were to use available data to explore potential trends and identify data gaps.

2.1. Elevated turbidity and recreational boating

We investigated the relationship between nearshore turbidity and recreational boating activity using data from 26 fixed, shallow water monitoring stations at which continuous water quality data, specifically turbidity, were available between the years 2003–2015 (www.vecos.org, www.eyesonthebay.net, Virginia N = 14; Maryland N = 12 stations; Fig. 1). The number and location of continuous water quality monitoring stations have varied as research needs and available resources have changed; stations are often located for a period of 3 years and then moved to another waterway. At each station, water quality parameters including depth, water temperature, salinity, pH, chlorophyll, turbidity, and dissolved oxygen are collected at 15-min intervals using YSI 6600 data sondes. In our analyses, we included monitoring stations with 2–3 years of consecutive data, near to shore (within ~50 m of shore and attached to a pier or dock), and on shore reaches with minimal exposure to commercial vessel traffic and/or wind waves to better isolate the effect of boat waves on nearshore turbidity patterns. We used ship traffic pattern data collected by the U.S. Coast Guard through the Automatic Identification System (AIS) to determine the level of commercial vessel traffic. The AIS is an onboard navigation safety device that transmits and monitors the location and characteristics of large vessels in U.S. and international waters in real time. The Marine Cadastre provides AIS data filtered and summarized into 1-min intervals, with each record (ping) representing a ship's location every

minute. We determined the total number of pings recorded in the vicinity of the stations from 2009 to 2014 and identified stations with low or no commercial traffic (half of the stations were in reaches with no pings, 11 stations had < 500 pings, and 2 sites had less than 1800 pings during the 6-year record) to be used in the analysis (spatial data source: Bilkovic et al., 2016a; and the Marine Cadastre http://marinecadastre.gov/ais) (Fig. 1).

In the Chesapeake Bay there is generally higher recreational boating activity on weekends (Saturday, Sunday) and major warm-weather holidays (i.e., Memorial Day, July 4th, Labor Day) than during weekdays (Monday, Tuesday, Wednesday, Thursday, Friday). As a result, our analytical approach involved comparing levels of turbidity during the week with the weekend and holidays (henceforth referred to as "weekend"). We limited the analysis to include turbidity data from May through September, when recreational boating is most prevalent. We used the 3 most recent years of consecutive data recorded in 15 min intervals for each station (except 4 Maryland stations which had 2 years of data). For each site, we estimated mean turbidity for weekend and weekdays during the three years examined. To control for other environmental factors (sediment sources, storms, tidal flow, etc.) that may affect an individual station's turbidity measures, we developed a turbidity index to represent the relative change in turbidity between weekends and weekdays (Equation (1), Fig. 2).

$$Turbidity\ Index\ (TI) = (mean\ weekend\ turbidity - mean\ weekday\ turbidity) \div mean\ weekday\ turbidity \quad (1)$$

In addition to the primary factor of interest, boating intensity, we included three potential moderating factors on the relative change in turbidity in the analysis: distance to navigational depth (m) from station, maximum fetch (m), and presence of shoreline armoring (bulkhead or riprap revetment). We conducted all estimates of factors for station locations in ArcGIS v. 10.4. We used the total number of piers and marinas upriver of the stations as a proxy measure for relative boating intensity; marinas tend to concentrate boat activity compared to private piers, so these were weighted by a factor of 5 (data source: Chesapeake Bay Shoreline Inventory, CCRM-VIMS, 2016). We defined navigational depth as 1-m to be inclusive of small watercraft (e.g., jetski), and estimated the shortest linear distance (m) from the station to the 1-m depth contour. We used maximum fetch as a surrogate for relative wind wave energy. We determined maximum fetch by estimating fetch, the distance over water that the wind blows in a single direction, for 16 compass directions originating from each station location and taking the largest value (i.e., longest distance). Presence or absence of armoring along the shoreline near the station was determined using aerial imagery and the Chesapeake Bay Shoreline Inventory (CCRM-VIMS, 2016). We then examined the effect of the 4 factors on the turbidity index (TI) using generalized linear models (GLM) with a Gaussian distribution, coupled with Akaike information criterion (AIC) model selection. Boating intensity, maximum fetch, and distance to navigational depth were log-transformed prior to the analysis to meet test assumptions. All possible combinations of the variables were assessed using AICc, which ranks models based on the principle of parsimony (Johnson and Omland, 2004). The top models were based on ΔAICc values < 2, and ΔAICc values between 3 and 7 were considered to be models with moderate but less support (Burnham and Anderson, 2002).

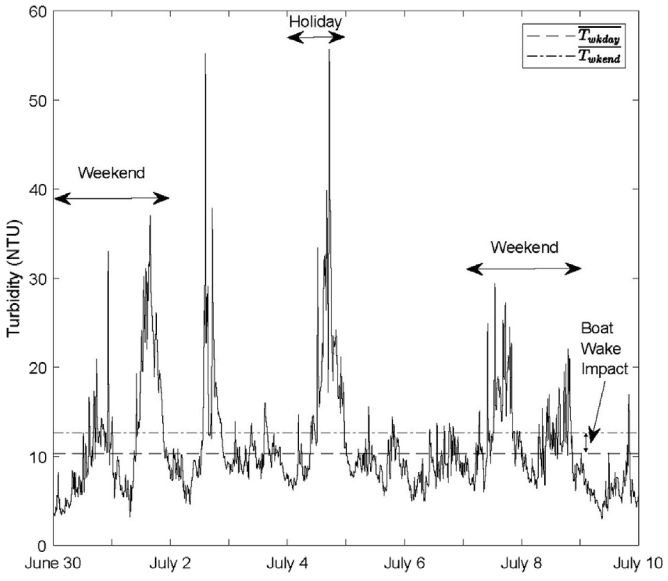

Fig. 2. Elevated turbidity associated with weekends and July 4th, 2007 in Pohick Creek, Virginia. T_{wkday} shows the mean turbidity during weekdays from June 30 to July 10, 2007. T_{wkend} is the mean turbidity during weekends and holidays in the same time frame. Figure modified from Bilkovic et al., (2017).

2.2. Occurrence of high erosion in low energy settings

Absent data on boating activity in relation to shoreline erosion rates, those shorelines that may be experiencing boat wake-induced erosion can be targeted for further study by comparing wind energy (fetch) with shoreline erosion rates. A shoreline with low fetch exposure would not typically have high erosion rates. If this does occur, another driver for the erosion - often boat wakes - is the likely cause. To evaluate the extent that this occurs in Chesapeake Bay, we identified shores potentially experiencing erosion from boating by selecting shorelines with low fetch (< 1000 m) and high erosion (≥ 0.3 m/yr) using GIS (ArcGIS v. 10.5). We determined maximum fetch for points every 50–100 m along all of the Virginia and Maryland tidal shorelines and used those values as the fetch along that reach of shoreline.

We transferred existing shoreline erosion rate data to the same shoreline as our estimated fetch data to facilitate spatial analyses. For both states, erosion rate data (distance/time) were previously developed using digital shoreline analysis system (DSAS) software 2.0 (Maryland) and 4.2 (Virginia) (Thieler et al., 2003; Thieler et al., 2010; https://woodshole.er.usgs.gov/project-pages//; DSAS). For Maryland, erosion rate data were calculated for transects spaced 20 m apart for a series of shorelines in varying time spans, with most occurring in some interval between 1942 and 1995 (MGS, 2003). For Virginia, erosion rate data were taken from the Shoreline Studies Program shoreline evolution database 1937–2009 (Hardaway et al., 2017), which calculated the erosion rate using the linear difference on transects between 1937 and 2009 shorelines. We then summarized the linear distances and percentages of Chesapeake Bay shorelines with low fetch exposure and high erosion rates.

2.3. Occurrence of shoreline armoring in low energy settings

Shoreline erosion can be caused by wind waves, boat wakes, or a combination of the two. Disentangling these effects is challenging, requiring site specific data on vessel traffic patterns combined with wind wave erosion models. Armoring on shorelines exposed to low wind wave energy can be indicative of erosion from other sources. In some instances, property owners have pointed specifically to boat wake erosion as a reason to armor their shorelines (Smith et al., 2017).

To evaluate the possibility that shorelines are being armored in areas not anticipated to have active erosion from wind waves, we compared a recommended shoreline management option for eroding shores on the basis of physical conditions with the actual management approach applied (e.g., bulkhead, riprap revetment, created or enhanced marsh) within three low wind wave energy tidal creeks in Virginia known to experience relatively high recreational boating pressure - Lynnhaven River, Virginia Beach; Lafayette River, Norfolk; Sarah Creek, Gloucester Point. Sarah Creek is a rapidly developing tidal

creek with relatively low wind wave energy and relatively high boating pressure including the presence of several marinas. Lafayette River is an urban tidal creek in Norfolk, Virginia. Lynnhaven River is a highly developed shallow-water tidal river. In this system, very shallow creeks have been dredged to provide residential boat access and there continues to be pressure to dredge additional creeks (Bilkovic, 2011). We used a geospatial Shoreline Management Model (SMM), Version 4.0 that identifies appropriate shoreline management approaches along Virginia's tidal shores using a suite of parameters that can be mapped and measured using GIS including fetch (a surrogate for wind wave energy), nearshore bathymetry, intertidal habitat (e.g., marsh), riparian features, bank height, and permanent structures within the riparian zone (CCRM, 2015). The SMM is based on decision tree logic and guidance that has been vetted through the Virginia Institute of Marine Science Wetlands Advisory Program and state locality shoreline management boards over many years (https://www.vims.edu/ccrm/ccrmp/bmp/decision_tools/index.php). The model extracts information from eleven spatial datasets containing attributes describing the shoreline. Using ESRI's ArcGIS ModelBuilder and scripts written in Python, a series of model pre-steps compiles the datasets into one linear shapefile. The model calls for specific data from the shapefile as a way to evaluate on-site condition, and follows the logic pathways of the decision tree to yield the final model output of shoreline best management approach recommendations for estuarine and tidal fresh shorelines, which is exported as a shapefile. All processing steps occur in ESRI's ArcMap, ArcGIS version 10.4 and 10.5 software.

Shoreline best management approach options in the SMM include three living shoreline treatments: 1) to create a new marsh or to maintain or enhance an existing marsh (maintain/enhance/create marsh), 2) create marsh with a stabilizing sill structure fronting the marsh, or 3) maintain beach or place offshore breakwaters with beach nourishment, and an armoring treatment: riprap revetment. Living shoreline approaches address erosion by providing protection, restoration, enhancement, or creation of vegetated shoreline habitats through strategic placement of plants, stone, sand fill and other structural or organic materials, while maintaining the connection between aquatic and terrestrial habitats (Bilkovic et al., 2016b). In Virginia, living shorelines are the preferred shoreline management option for tidal shorelines where appropriate (Code of Virginia §28.2–104.1). The SMM is a tool to help identify shoreline reaches that are appropriate for the preferred management approach of living shorelines. A recommendation to maintain/enhance/create marsh is applied to shorelines with low wind wave energy (low fetch, 0–0.8 km) where marshes can be established or maintained naturally without protection, no physical structures near the shoreline that would prohibit bank grading to achieve proper tidal elevations for marsh plants, and shallow water (no greater than 1 m deep up to 10 m from shore). A stabilization structure fronting the marsh (e.g., rock sill or oyster reef) may be required in shallow water, moderate wind wave energy environments (fetch between 0.8 and 3.2 km) to allow the marsh to become established. Armoring (riprap revetment) is recommended for moderate (fetch between 0.8 and 3.2 km) to high (fetch > 3.2 km) wind wave energy, where the nearshore is deep, and/or the shoreline has permanent physical structures that would prohibit bank grading. For each tidal creek, we documented the occurrence of shorelines that have been armored (bulkhead or riprap revetment) while having a recommended shoreline management approach to maintain/enhance/create marsh that is indicative of a low wind wave energy shoreline. In addition, we extracted information provided by property owners from the Virginia Shoreline Permit Database (1993–2010; CCRM, 2019) on their purpose for applying for a permit to armor their shoreline; listed reasons include erosion control, marina development, commercial construction, water access, yard improvement, aesthetics, and other.

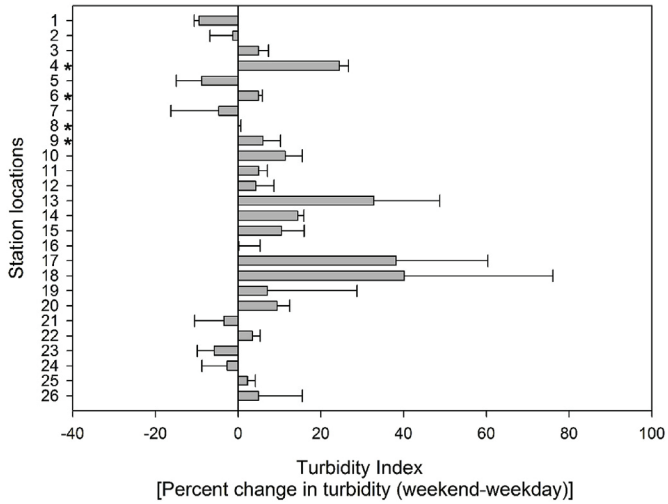

Fig. 3. Comparison of weekend turbidity measures to weekday measures. Positive TI values indicate relatively higher turbidity during the weekend than the week possibly because of increased recreational boating intensity during the weekend. Negative values indicate relatively higher turbidity during the week than weekend. Station location numbers correspond to those on Fig. 1. Stations with * had 2 years of data, all other stations had 3 years of data. Figure modified from Bilkovic et al., (2017).

3. Results

3.1. Elevated turbidity and recreational boating

Elevated turbidity was evident on the weekends in comparison to weekdays for the majority of the stations (n = 19; 73%); however, in many instances, the percent difference was low (< 5% turbidity difference for 35% of stations with elevated weekend turbidity). A negative turbidity index (higher turbidity during the week) occurred for 7 stations, but weekday turbidity at those sites was only slightly (> 10%) higher than the weekend turbidity (Fig. 3). None of the variables examined were significantly associated with the turbidity index (GLM: $X^2 = 3.14$, df = 21, p = 0.53). However, model selection based on AICc indicated marginal support ($\Delta AIC_c = 3.04$) for a best fit model that included boating intensity and armoring (Supporting table 1). This was likely because on unarmored shores, the turbidity index tended to be higher (TI = 10.5% ± 15.1%) in comparison to armored shores (TI = 4.5% ± 11.3) and along unarmored shores, boating intensity appeared to be associated with elevated local turbidity within some waterways.

3.2. Occurrence of high erosion in low energy settings

There are about 26,000 km of tidal shoreline in Chesapeake Bay, but only about a third of that shoreline has erosion data available (Table 2). Of the 8576 km of shoreline for which erosion data are available, 1310 km (15%) are potentially experiencing boat wake-induced erosion. This is likely an underestimate because a large proportion of low energy shorelines, the areas most at risk of experiencing boat wake-induced erosion (i.e., tidal creeks), were lacking erosion rate information (68%), which limited our ability to identify areas experiencing unusually high erosion (Fig. 4).

3.3. Occurrence of shoreline armoring in low energy settings

In all three creeks, armoring is present along approximately a quarter (Sarah Creek 28% (7.1 km), Lynnhaven River 22% (41.1 km), Lafayette River 31% (22.3 km)) of the shorelines where the SMM specifies that only marsh enhancement, maintenance, or creation should be

Table 2
Chesapeake Bay tidal shorelines with available data, approximately 15% (1310 km) are experiencing high erosion (≥0.3 m/yr) in low wind-wave energy settings (fetch < 1000 m), indicating potential boat wakewave induced erosion. Significant erosion data deficiencies exist for high risk areas, so these estimates are likely low.

Location	Total tidal shoreline (km)	Shoreline with erosion and fetch data (km)	Shoreline with erosion and fetch data (%)	Shorelines with low fetch and high erosion (km)	Shorelines with low fetch and high erosion (%)
Maryland	10,945	3302	30	569	17
Virginia	15,776	5274	34	741	14
Total	26,721	8576	32	1310	15

needed to stabilize shorelines (Fig. 5). In fact, on the basis of the physical setting, the vast majority of the shorelines in these low energy creeks could be managed simply by maintaining, enhancing, or creating marshes (Sarah Creek 83% (25.6 km), Lynnhaven River 74% (185.6 km), Lafayette River 78% (70.8 km)). This suggests another source (or perceived source) of shore erosion, possibly boating, has led to the armoring of shorelines (along with the attendant adverse effects of armoring) in low energy areas, where armoring should not be necessary. The vast majority of property owners stated erosion control was the purpose for armoring ((Sarah Creek 98% (62 projects), Lynnhaven River 97% (251 projects), and Lafayette River 92% (135 projects)).

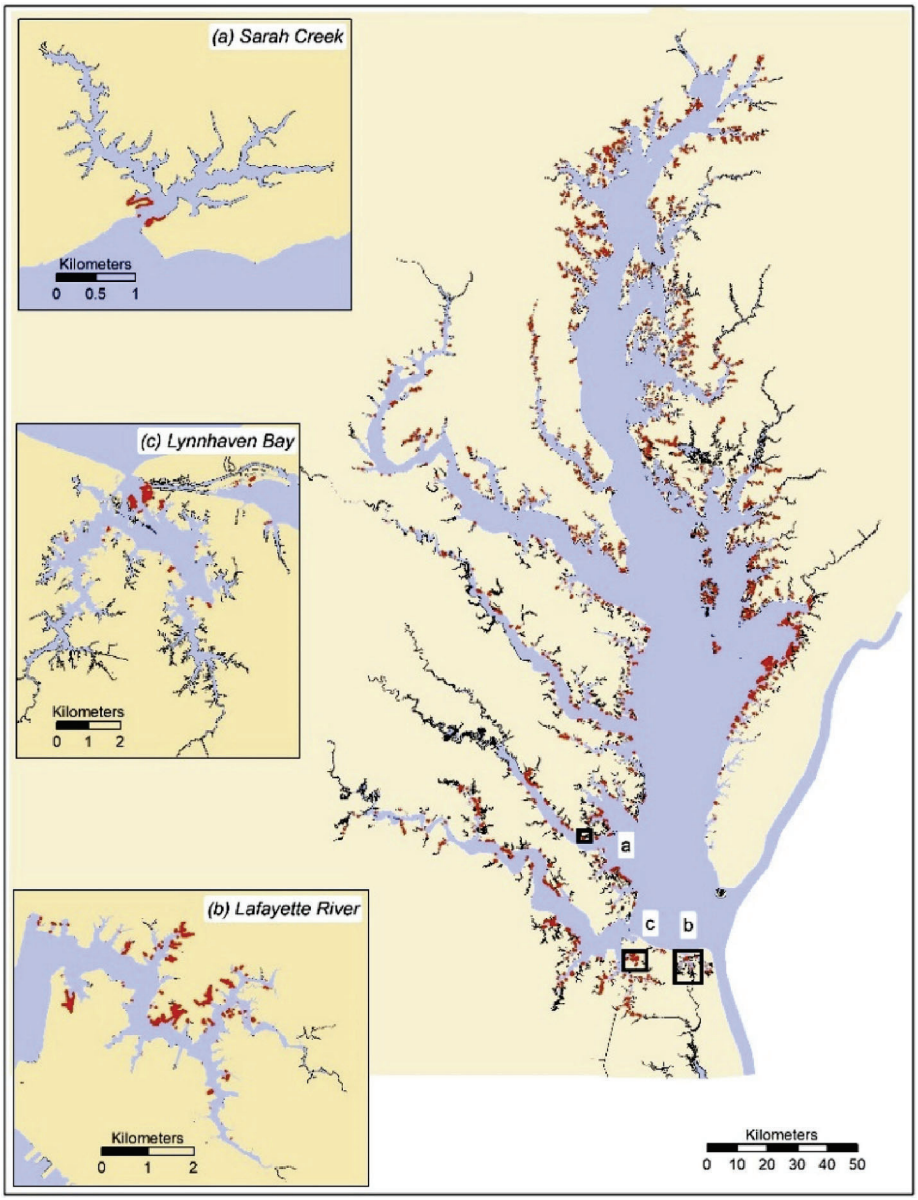

Fig. 4. Distribution of shorelines likely experiencing boat wave-induced erosion in Chesapeake Bay (shown in red); these are shorelines with low fetch (< 1000 m) and high erosion rates (≥0.3 m/yr). The black shorelines are areas lacking erosion data. The insets show example waterways with low wind wave energy where erosion should be low – Sarah Creek (a), Lafayette River (b), and Lynnhaven River (c). (For interpretation of the references to colour in this figure legend, the reader is referred to the Web version of this article.)

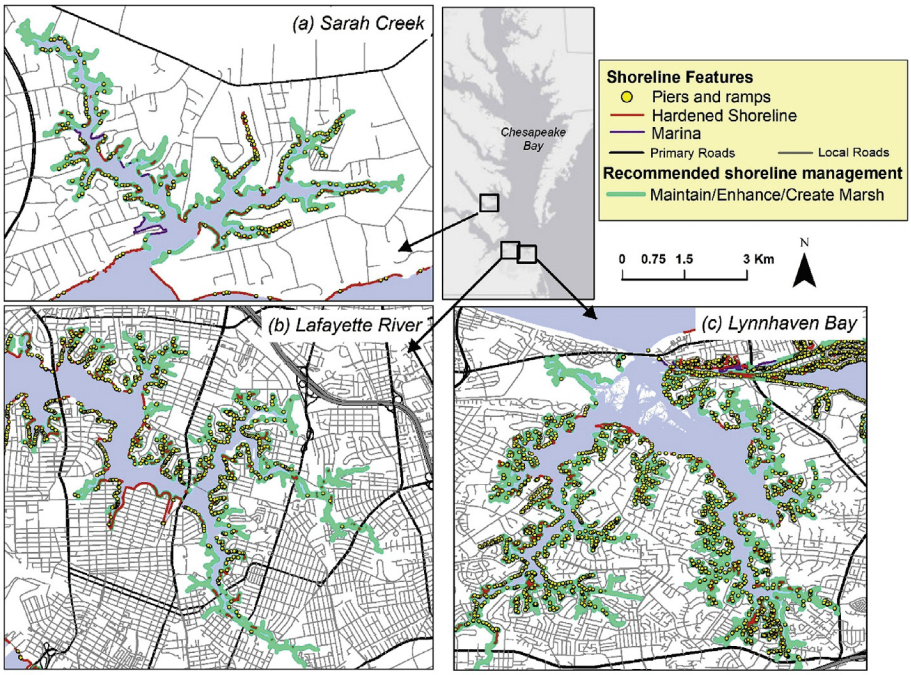

Fig. 5. On the basis of physical conditions, the recommended shoreline management approach is to create a new marsh or to maintain or enhance an existing marsh for the majority of the shoreline – **(a)** Sarah Creek, Virginia (83%), **(b)** Lafayette River, Virginia (78%), and **(c)** Lynnhaven River, Virginia Beach, Virginia (74%). Of those shoreline reaches where marsh is recommended, 28%, 31% and 22%, respectively, have armoring (revetment, bulkhead) currently. Figure modified from Bilkovic et al., (2017).

4. Discussion

There is evidence that links boat wake energy to elevated turbidity and shoreline erosion, particularly in narrow waterways (Ellis et al., 2002; Baldwin, 2008; Houser, 2010; Currin et al., 2017). Our findings suggest that boating may contribute to shoreline erosion and poor water clarity in some Chesapeake Bay creeks and tributaries. Turbidity was elevated in many waterways during periods of expected high boating activity. Armoring was placed along about a quarter of the low energy shorelines of all three examined tidal creeks that are exposed to relatively high boating pressure. Of the nearly 9000 km of shoreline examined throughout the Bay, 15% (1,310 km) are low energy shorelines that are experiencing high erosion ($\geq$0.3 m/yr) that is not likely attributable to wind wave energy. Although our study cannot causally link boat traffic to high erosion along low fetch shorelines, the reaches we identified as potentially being vulnerable to boat traffic impacts are places to target for additional data collection on boating intensity and wave conditions, as well as potential candidate areas for management or policy action to mitigate boat wake impacts. A series of strategically targeted investigations of shorelines of particular concern (ideally shorelines that are experiencing significant erosion and that represent a range of conditions with respect to fetch and boating activity), would be a valuable first step to development of a Bay-wide understanding of the conditions under which boat wakes make a significant contribution to shoreline erosion. This type of data would provide the foundation for sound policy decisions regarding boat wake management strategies in the Chesapeake Bay and elsewhere.

Boat wake policies and the overarching regulatory framework in states with Bay frontage (Virginia, Maryland, and Delaware) vary from state to state. In Virginia, neither state code nor regulations establish wake or speed restrictions for any specific waterway. However, a state agency, the Virginia Department of Game and Inland Fisheries, has express authority to enforce and administer state boating laws (Va. Code Ann. § 29.1–701(A)) and has adopted regulations regarding boat speed near vessels, piers, docks, boathouses, and persons generally (4 Va. Admin. Code § 15-390-80). Additionally, localities have express authority to implement their own boat wake restrictions via a local ordinance (Va. Code Ann. § 29.1–744(D)), and individuals or businesses may apply to their local governing body for the establishment of a no-wake zone via a local ordinance (Va. Code Ann. § 29.1–744(E)). Although Maryland also delegates regulatory authority to a state agency, the Maryland Department of Natural Resources (DNR) (Md. Code Ann., Nat. Res. § 8-8-704(c)), and permits localities to establish local regulations that conform with DNR regulations (Md. Code Ann., Nat. Res. § 8-8-704(f)), Maryland has set forth speed limits for specific waterways within state code (*see,* e.g., Md. Code Ann., Nat. Res. § 8–725.2). Additionally, DNR's regulations define various speed limits (Md. Code Regs. 08.18.01.03) and apply these defined limits to specific designated areas, such as the eastern and western shores of the Chesapeake Bay (Md. Code Regs. 08.18.07.01–02). As with both Virginia and Maryland, Delaware also delegates regulatory authority to a state agency, the Delaware Department of Natural Resources and Environmental Control (DNREC) (Del. Code Ann. tit. 23 § 2114(b)(4)). DNREC regulations define “slow-no-wake” and limit speeds next to swimmers and certain structures (Del. Admin. Code § 3100–2.1 & −6.1.2). Additionally, localities have limited boat speeds near specific structures or on specific waterways (*See* e.g., Smyrna, Delaware Code of Ordinances Sec. 46-58(h)). While regulation of boat wake speed does occur in some manner within each of the three states with Bay frontage, this regulation has not been done comprehensively across the Bay or through coordination between the states.

Other shallow water estuaries have established boat wake policies following differing procedures. Examples include the Narragansett Bay in Rhode Island and the Pamlico Sound in North Carolina. Rhode Island authorizes the Department of Environmental Management (DEM) to “establish maximum speeds for boats in the public harbors in the state of Rhode Island at five (5) miles per hour, no-wake” (46 R.I. Gen. Laws § 22–9(c)). Additionally, ordinances or local laws may be adopted that are identical to the state laws and regulation, and subdivisions of the state may apply to DEM for special rules and regulations regarding vessel operations within the subdivision's territorial limits (46-22 R.I. Gen. Laws §§ 14(a)&(b). This has resulted in many coastal localities adopting wake restrictions (*See* e.g., Bristol, Rhode Island Code of Ordinances Sec. 8-41)). North Carolina utilizes a state agency, the North Carolina Wildlife Resources Commission (NCWRC), to implement boat wake policies in a uniform manner across the state (N.C. Gen. Stat. § 75A-15). NCWRC is authorized to adopt its own rules to prohibit the entry of vessels and establish speed zones in certain areas (N.C. Gen.

Stat. § 75A-15). Additionally, localities may petition NCWRC for wake rules and the Commission is authorized to adopt rules for local areas that are "heavily used for water recreation purposes by persons from other areas of the State and as to which there is not coordinated local interest in regulation" (N.C. Gen. Stat. § 75A-15). Under this management structure, boat wake restrictions have been established for almost all coastal counties through agency regulation. This results in consistent language between regulations and provides easier access to boat wake restriction rules because the information can be found in one place.

Management and policy strategies to address boat wake-induced shoreline erosion that are alternatives to boat speed/wake restrictions include motorboat bans and shoreline armoring. Banning motorized vessels is unlikely to be adopted in any major waterway, especially one whose economy relies heavily on both recreational and commercial boating and/or shipping; however, in smaller waterways this can be a viable option. With respect to armoring of the shoreline, living shorelines are preferred to armoring because these techniques strengthen the endurance of the shoreline and build resilience by using natural vegetation and sediment. By contrast, armoring may result in adverse effects, such as natural habitat degradation and erosion of downdrift shorelines due to deflected wave energy or lack of sediment supplies to maintain the shorelines. Other policy strategies targeting boating behavior that have a higher likelihood of being implemented include limiting the number of passages that a boat makes in a waterway, setting minimum distance of a navigation channel from the shore, and implementing boat size restrictions in small waterways.

Although concerns about the harm that boating activity may pose for shoreline stability, water quality, and ecosystem integrity have been voiced for decades, the development and implementation of management and policy actions to mitigate boat impacts has been hampered by lack of a proven approach for quantifying the role of boat waves in shoreline erosion. While there is currently no one-size-fits-all approach for evaluating boat wake impacts, there have been a few recent attempts to develop overarching strategies. Glamore (2008) developed a Decision Support Tool (DST) aimed at evaluating the relative impact of boat vs. wind waves along a given reach of shoreline. The tool calculates total wind wave energy, total boat wake energy and shoreline erosion potential. User inputs include data on the frequency of boat passage, local wind data, and 22 different shoreline characteristics that are used to determine erosion potential including: shoreline slope, sediment type, channel width and upland land use, among others. Output from the DST includes guidance regarding whether management of boat wakes is necessary based on the relative amount of shoreline wave energy contributed by boats compared to that of wind energy, and the calculated shoreline erosion potential. This tool represents a viable approach to analysis of boat wake impacts and has been successfully employed in the management of lake shorelines and limited river reaches, but the large number of required input variables make its application across a large and diverse system like Chesapeake Bay challenging.

Fonseca and Malhotra (2012) developed a similar approach that involved the use of two GIS-based modeling packages: WEMo (Wave Exposure Model) for quantifying wind-wave energy and its companion product BoMo (Boat wake Model) for quantifying boat wake energy. In their approach, these tools are used in tandem to estimate the relative contribution of boat wake energy along a given shoreline. WEMo (which is freely available, https://coastalscience.noaa.gov/research/coastal-change/wemo/) requires users to input local wind data, a GIS shoreline shapefile, and high quality bathymetry data; BoMo (not yet available) also requires shoreline and bathymetry data and allows a user to select hull type, size and speed. The models then calculate the total amount of wave energy impacting the shoreline from their respective sources. With this approach, both wind and boat wakes can be hindcast or forecast to determine which is the predominant driver of shoreline erosion. Like the DST, this dual model approach is limited by the availability of data. While wind data and shoreline shapefiles are relatively easy to obtain, much of the publicly available bathymetry data is either outdated, or not of sufficient spatial coverage, and data on the number of boat passages along a given shoreline do not exist. As a result, these approaches have not been broadly implemented.

Prior to development of a truly quantitative understanding of boat wake-induced erosion at a systems-level, interim protective measures can be applied on the basis of documented effects of boat wakes in the literature. Wave height- or wave energy-based criteria have been used to establish wake management strategies (Stumbo et al., 1999; Glamore, 2008). Wave decay studies indicate that, in general, even small (< 9 m) power boats traveling within 150 m of the shore are capable of generating wave heights that can cause erosion of vegetated marsh shorelines (Zabawa and Ostrum, 1980; Coops et al., 1996; Coops et al. 1996, 1996; Schafer et al., 2003; Roland and Douglas, 2005). This distance is not without exceptions, for example, boats traveling further offshore can still produce erosive boat wakes, particularly those vessels that are large or moving at high speeds, which increases the wake energy. Still, setbacks can be a relatively easy solution to boat wake-induced shoreline erosion where the setting allows. With additional information on recreational and commercial boating traffic, varying setback distances could be established in vulnerable Bay waterways. A 150 m setback in small, low energy, waterways that have high recreational boating activity could help reduce shoreline erosion, while those waterways used by large commercial vessels may require larger setbacks to lessen the erosive effects of wakes. In restricted waterways where there is no space to move channels away from shore, no-wake zones provide an alternative strategy for managing erosion. A GIS-based investigation of regions where there IS high erosion that is likely caused by boat wakes and there IS NOT room to move navigation channels farther from shore might provide the first cut for sites to investigate for potential implementation of no-wake zones. Another important consideration for the implementation of no-wake zones is that maximum wave height can be produced as a boat transitions in and out of planing mode, often at the start and finish of designated no-wake zones. This should be factored into their placement.

Shoreline wave energy, whether generated by wind or boating activity, is a critical factor to consider in the implementation of shoreline management strategies. The design and use of more natural approaches to shoreline erosion (i.e., living shorelines) is strongly influenced by shoreline wave energy. A quantitative understanding of the relationship between boating activity and shoreline wave energy will help to inform the design of these sites and give property owners and design practitioners a greater level of confidence in their application. In addition, this information could be used when planning and siting Bay restoration activities (e.g., wetland or seagrass restoration) to evaluate the probability of long-term persistence. Conversely, and just as important, this information can help to identify areas where shoreline wave energy is too high to consider the use of "softer" living shoreline management strategies.

While our focus area is Chesapeake Bay, sheltered coasts around the world are struggling with these same issues and as coastal regions continue to become more densely populated, the role of boat wake-induced erosion will be increasingly significant. In general, there is a dearth of data on boating activity and its consequences, particularly that of small, recreational boats. While some of these data gaps can be effectively addressed through citizen science-led efforts (e.g., documenting the frequency of boat passages at a given location), others will require field and modeling studies. All efforts to increase our quantitative understanding of the amount of boat wake energy impacting a given shoreline, and the consequences of this impact, will be vital to the development of effective management strategies for mitigating boat wake-induced shoreline erosion. Such strategies should be implemented with a whole-system perspective, as uniform boat wake policies will likely be most effective for consistent shoreline protection.

Funding

Funding was provided for this research by Chesapeake Bay Program Scientific and Technical Advisory Committee (STAC) and Chesapeake Research Consortium, Edgewater, Maryland.

Acknowledgments

We thank Ken Moore, David Parrish, Bruce Michael, Mark Trice, and Brian Smith for providing Chesapeake Bay continuous water quality monitoring data. Robert Isdell contributed to the GIS analysis on shoreline erosion rates and Marcia Berman, Karinna Nunez and Tamia Rudnicky provided information on the Shoreline Management Model. We thank Christine Tombleson for providing data from the Virginia Shoreline Permit Database. The Virginia Coastal Policy Center wishes to thank W&M Law School students Sarah Edwards, Kristin McCarthy and Emily Messer for their assistance with this paper. This paper is Contribution No.3842 of the Virginia Institute of Marine Science, William & Mary. We thank the Chesapeake Bay Program Scientific and Technical Advisory Committee (STAC), including Lisa Wainger, for convening and supporting this group as we generated a report on this topic that informed this paper (STAC 17–002, https://scholarworks.wm.edu/reports/1271/).

Appendix A. Supplementary data

Supplementary data to this article can be found online at https://doi.org/10.1016/j.ocecoaman.2019.104945.

References

Asplund, T.R., 1996. Impacts of Motorized Watercraft on Water Quality in Wisconsin Lakes. Wis. Dep. Nat. Res. Bur. Research, Madison, WI, pp. 46 PUBL-RS-920-96.

Baldwin, D.S., 2008. Impacts of Recreational Boating on River Bank Stability: Wake Characteristics of Powered Vessels. Report of the Murray Catchment Management Authority. Murray-Darling Freshwater Research Centre, Wodonga, Victoria.

Bauer, B.O., Lorang, M.S., Sherman, D.J., 2002. Estimating boat-wake-induced levee erosion using sediment suspension measurements. J. Waterw. Port, Coast. Ocean Eng. 128, 152–162.

Bilkovic, D.M., 2011. Response of tidal creek fish communities to dredging and coastal development pressures in a shallow-water estuary. Estuar. Coasts 34 (1), 129–147.

Bilkovic, D.M., Mitchell, M., Mason, P., Duhring, K., 2016b. The role of living shorelines as estuarine habitat conservation strategies. Coast. Manag. 44 (3), 161–174.

Bilkovic, D.M., Slacum Jr., H.W., Havens, K.J., Zaveta, D., Jeffrey, C.F.G., Scheld, A.M., Stanhope, D., Angstadt, K., Evans, J.D., 2016a. Ecological and economic effects of derelict fishing gear in the Chesapeake Bay: 2015/2016 final assessment report. Prepared for marine debris Program, office of response and restoration, national oceanic and atmospheric administration. https://marinedebris.noaa.gov/reports/effects-derelict-fishing-gear-chesapeake-bay-assessment-report.

Bilkovic, D., Mitchell, M., Davis, J., Andrews, E., King, A., Mason, P., Herman, J., Tahvildari, N., Davis, J., 2017. Review of Boat Wake Wave Impacts on Shoreline Erosion and Potential Solutions for the Chesapeake Bay. STAC Publication Number 17-002, Edgewater, MD, pp. 68.

Burnham, K.P., Anderson, D.R., 2002. Model Selection and Multimodel Inference: a Practical Information-Theoretic Approach. The University of Chicago Press, New York.

Campbell, D., 2015. Quantifying the Effects of Boat Wakes on Intertidal Oyster Reefs in a Shallow Estuary. Thesis. University of Central Florida.

Castillo, J.M., Luque, C.J., Castellanos, E.M., Figueroa, M.E., 2000. Causes and consequences of salt-marsh erosion in an Atlantic estuary in SW Spain. J. Coast. Conserv. 6, 89–96.

Center for Coastal Resources Management (CCRM), 2019. Shoreline Permit Database. Virginia Institute of Marine Science, William & Mary, Gloucester Point, Virginia.

Center for Coastal Resources Management (CCRM), 2016. Chesapeake Bay Shoreline Inventory Database. Virginia Institute of Marine Science, William & Mary, Gloucester Point, Virginia. http://www.vims.edu/ccrm/research/inventory/index.php.

Center for Coastal Resources Management (CCRM), 2015. Shoreline Management Model, Version 4. Virginia Institute of Marine Science, William & Mary, Gloucester Point, Virginia.

Chesapeake Bay Watershed Agreement, 2014. Chesapeake Bay Program. https://www.chesapeakebay.net/what/what_guides_us/watershed_agreement, Accessed date: 27 November 2018.

Coops, H., Geilen, N., Verheij, H.J., Boeters, R., van der Velde, G., 1996. Interactions between waves, bank erosion and emergent vegetation: an experimental study in a wave tank. Aquat. Bot. 53, 187–198.

Currin, C.A., Davis, J., Malhotra, A., 2017. Response of salt marshes to wave energy provides guidance for successful living shoreline implementation. In: Bilkovic, D.M., Toft, J., Mitchell, M., La Peyre, M. (Eds.), Living Shorelines: the Science and Management of Nature-Based Coastal Protection. CRC Press, Taylor & Francis Group.

DSAS. Digital Shoreline Analysis System. https://woodshole.er.usgs.gov/project-pages/DSAS/.

Ellis, J.T., Sherman, D.J., Bauer, B.O., Hart, J., 2002. Assessing the impact of an organic restoration structure on boat wake energy. J. Coast. Res. 36, 256–265.

Environmental Finance Center, University of Maryland, 2013. Recreational boating and fiscal analysis study. https://efc.umd.edu/assets/boating_analysis_final_report_-_noaa_added.pdf.

Fonseca, M., Malhotra, A., 2012. Boat wakes and their influence on erosion in the Atlantic Intracoastal Waterway, North Carolina. NOAA Tech. Memo. NOS-NGS #143. 24p.

Glamore, 2008. A Decision support tool for assessing the impact of boat wake waves on inland waterways. International Conference on Coastal and Port Engineering in Developing Countries. pp. 20. available. http://pianc.org.

Grizzle, R.E., Adams, J.R., Walters, L.J., 2002. Historical changes in intertidal oyster (*Crassostrea virginica*) reefs in a Florida lagoon potentially related to boating activities. J. Shellfish Res. 21, 749–756.

Hallac, D.E., Sadle, J., Pearlstine, L., Herling, F., Shinde, D., 2012. Boating impacts to seagrass in Florida Bay, Everglades National Park, Florida, USA: links with physical and visitor-use factors and implications for management. Mar. Freshw. Res. 63 (11), 1117–1128.

Hardaway Jr., C.S., Milligan, D.A., Wilcox, C.A., 2017. Shoreline Studies Program shoreline evolution database 1937-2009. Retrieved from. http://www.vims.edu/research/departments/physical/programs/ssp/shoreline_evolution/index.php.

Houser, C., 2010. Relative importance of vessel-generated and wind waves to salt marsh erosion in a restricted fetch environment. J. Coast. Res. 262, 230–240.

Johnson, J.B., Omland, K.S., 2004. Model selection in ecology and evolution. Trends Ecol. Evol. 19 (2), 101–108.

Kildow, J.T., Colgan, C.S., Johnston, P., Scorse, J.D., Farnum, M.G., 2016. State of the US Ocean and Coastal Economies: 2016 Update. National Ocean Economics Program.

Koch, E.W., 2002. Impact of boat-generated waves on a seagrass habitat. J. Coast. Res. 37, 66–74.

Koch, E.W., Sanford, L.P., Chen, S.N., Shafer, D.J., Smith, J.M., 2006. Waves in Seagrass Systems: Review and Technical Recommendations (No. ERDC-TR-06-15). Maryland University Cambridge Center for Environmental Science.

Liddle, M.J., Scorgie, H.R.A., 1980. The effects of recreation on freshwater plants and animals: a review. Biol. Conserv. 17 (3), 183–206.

Maryland Geological Survey (MGS), 2003. Shoreline change map data for tidewater Maryland. http://www.mgs.md.gov/coastal_geology/shoreline%20change.html.

Maynord, S.T., Biedenharn, D.S., Fischenich, C.J., Zufelt, J.E., 2008. Boat-Wave-Induced Bank Erosion on the Kenai River, Alaska. (No. ERDC TR-08-5). U.S. Army Engineering Research and Development Center, Vicksburg, MS.

McGranahan, G., Balk, D., Anderson, B., 2007. The rising tide: assessing the risks of climate change and human settlements in low elevation coastal zones. Environ. Urbanization 19 (1), 17–37.

Parnell, K.E., Kofoed-Hansen, H., 2001. Wakes from large high-speed ferries in confined coastal waters: management approaches with examples from New Zealand and Denmark. J. Coast. Manag. 29, 217–237.

Roland, R.M., Douglas, S.L., 2005. Estimating wave tolerance of *Spartina alterniflora* in coastal Alabama. J. Coast. Res. 21, 453–463.

Schafer, D.J., Roland, R., Douglass, S.L., 2003. Preliminary Evaluation of Critical Wave Energy Thresholds at Natural and Created Coastal Wetlands. WRP Technical Notes Collection ERDC-TN-WRP-HS-CP-2.2. U.S. Army Engineering Research and Development Center, Vicksburg, MS.

Smith, C.S., Gittman, R.K., Neylan, I.P., Scyphers, S.B., Morton, J.P., Fodrie, F.J., Grabowski, J.H., Peterson, C.H., 2017. Hurricane damage along natural and hardened estuarine shorelines: using homeowner experiences to promote nature-based coastal protection. Mar. Policy 81, 350–358.

Sorenson, R.M., 1973. Water waves produced by ships. J. Waterw. Harb. Coast. Eng. Div.: Proc. Am. Soc. Civ. Eng. 99, 245–256.

Stumbo, S., Fox, K., Dvorak, F., Elliot, L., 1999. The prediction, measurement, and analysis of wake wash from marine vessels. Mar. Technol. 36, 248–260.

Thieler, E.R., Himmelstoss, E.A., Zichichi, J.L., Ergul, Ayhan, 2010. Digital Shoreline Analysis System (DSAS) version 4.0—an ArcGIS Extension for Calculating Shoreline Change (ver. 4.2, August 2010). U.S. Geological Survey Open-File Report 2008–1278.

Thieler, E.R., Martin, D., Ergul, A., 2003. The Digital Shoreline Analysis System, Version 2.0: Shoreline Change Measurement Software Extension for ArcView. USGS U.S. Geological Survey Open-File Report 03-076.

U. S. Army Corps of Engineers (USACE), 1994. Cumulative Impacts of Recreational Boating on the Fox River - Chain O' Lakes Area in Lake and McHenry Counties, Illinois: Final Environmental Impact Statement. Environ. And Social Anal. Branch. U.S. Army Corps of Eng., Chicago, IL, pp. 194.

Whitfield, A.K., Becker, A., 2014. Impacts of recreational motorboats on fishes: a review. Mar. Pollut. Bull. 83 (1), 24–31.

Zabawa, C., Ostrom, C., 1980. The Role of Boat Wakes in Shoreline Erosion in Anne Arundel County, Maryland. Final Report to the Coastal Resources Division, Maryland Department of Natural Resources.